

POLITECNICO DI TORINO

Collegio di Ingegneria Meccanica, Aerospaziale, dell'Autoveicolo e della Produzione

Corso di Laurea Magistrale in Automotive Engineering

Tesi di Laurea Magistrale

Behavioral Analysis of Entrapped Condensate in a Vehicle Charge-Air-Cooler



Relatore

Prof. Marco C. Masoero

Candidate

Caleb R. St-Aubin Ouellette

Ottobre 2019

DECLARATION OF ORIGINALITY

I hereby certify that I am the sole author of this thesis and that no part of this thesis has been published or submitted for publication.

I certify that, to the best of my knowledge, my thesis does not infringe upon anyone's copyright nor violate any proprietary rights and that any ideas, techniques, quotations, or any other material from the work of other people included in my thesis, published or otherwise, are fully acknowledged in accordance with the standard referencing practices. Furthermore, to the extent that I have included copyrighted material that surpasses the bounds of fair dealing within the meaning of the Canada Copyright Act, I certify that I have obtained a written permission from the copyright owner(s) to include such material(s) in my thesis and have included copies of such copyright clearances to my appendix.

I declare that this is a true copy of my thesis, including any final revisions, as approved by my thesis committee and the Graduate Studies office, and that this thesis has not been submitted for a higher degree to any other University or Institution.

ABSTRACT

The effect of the Weber number and inclination angle on the fraction carryover of the condensation found in a vehicle charge-air-cooler were experimentally investigated under steady state conditions. The validity of describing the fraction carryover in terms of the Weber number, using the heat exchanger fin spacing as the significant length, was explored. Condensate entrainment testing was performed at multiple heat exchanger face velocities and the fraction of condensate that is blown through with respect to the total amount was recorded for angles ranging between 0 and 50 degrees. A positive agreement between the results obtained and those from literature was found for the use of the Weber number as the governing parameter for heat exchanger condensate entrainment. A predictive equation valid between charge-air-cooler angles of 0 and 40 degrees was obtained to describe the expected entrainment that uses the Weber number, and a critical Weber number as input.

Supplementary testing was also performed to observe the physical effects of a shearing air flow on a liquid bridge suspended between two plates. The observational testing showed that a liquid bridge may react in four different ways to the airflow, depending on the velocity.

ACKNOWLEDGEMENTS

I would like to acknowledge my academic advisor, Dr. Ofelia Jianu. Thank you for all your assistance, motivation and support throughout this project. It is with your knowledge and guidance that it was all able to come together. Your devotion to research and your desire to pass on your knowledge through teaching is truly inspiring. I am proud to be one of your first graduate students and I am sure that the ones to come will be grateful to have your mentorship.

To the remainder of my committee: Dr. Vesselina Roussinova and Dr. Narayan Kar, Dr. Marco Masoero, thank you for your advice and assistance. Your input helped shape the project and I, for that, am truly grateful.

I want to express my tremendous gratitude to Dr. Tim Scott for your counsel, advice, coaching and motivation throughout this project. Your extensive experience as a mentor is very evident. I truly appreciate your efforts to ensure the success of the project.

To the Fiat Chrysler Automobiles team, Dan Hornback, Mauro Casella, Marie Mills, Nicole St. Louis, Nathan Waak, Walter Ferraris for all the support and assistance throughout this project. To the technical team at the Chrysler Technical Center as well, Pat Moore, Mike Lucas, Dave Hoffman, I am grateful for your advice and assistance with the fabrication.

To the program coordinators on the Canadian and Italian sides, Dr. Jennifer Johrendt and Dr. Giovanni Belingardi.

Of course, to my loving girlfriend Caelan, my parents, Roch and Denise and sister, Ani and to my friends for your unconditional love and support. It was with your help that I was able to persevere through the tougher parts of this, both literal and figurative, journey.

Finally, to my friends and travel partners, Alfredo and Kyle. It's been quite the ride getting here! Thank you for making living abroad that much more enjoyable. I wish you both the best of luck with the rest of your careers.

TABLE OF CONTENTS

DECLARATION OF ORIGINALITY	ii
ABSTRACT.....	iii
ACKNOWLEDGEMENTS	iv
LIST OF TABLES.....	xi
LIST OF FIGURES	xii
LIST OF APPENDICES	xv
LIST OF ABBREVIATIONS.....	xvi
Chapter 1 – Introduction	1
1.1 Motivation	1
1.1.1 Condensation on Charge-Air-Cooler (CAC) Fins.....	1
1.1.2 Effect of Condensation in Charge-Air-Coolers.....	2
1.1 Background	3
1.2.1 Charge-Air-Coolers	3
1.2.2 Exhaust Gas Recirculation	4
1.2.3 Moist Air Fundamentals	6
1.3 Project Objectives	9
1.4 Outline of Thesis	11
Chapter 2 - Description of Condensation Phenomena	12
2.1 Widely Spaced Plates.....	12

2.2 Close Spaced Plates	14
2.3 Louvered fins	16
Chapter 3 - Literature review	19
3.1 Lack of Available Research on this Topic	19
3.2 Effect of Condensation on heat and mass transfer	22
3.3 Condensate retention	23
3.4 Condensate Carryover Phenomena	24
3.5 Mechanisms for Droplet Entrainment.....	26
3.5.1 Entrainment from Two Phase Liquid-Gas Flow	26
3.5.2 The Onset of Entrainment (OE).....	27
3.5.3 Droplet Entrainment Inception Velocity	31
3.5.4 Kutateladze Criterion.....	31
3.5.5 Ishii and Grolmes Model	35
3.6 Droplets Subjected to Gravity and Shearing Air Forces	36
3.7 Full or Partial Droplet Entrainment from a Surface.....	38
3.7.1 Liquid Droplet Entrainment from a Vertical Surface	38
3.8 Drag Force on a Droplet Draining Off the Outlet of an Exchanger	39
Chapter 4 – Current Heat Transfer Model	42
4.1 Assumption of an Even Condensation Layer	42
4.2 Formulation of Maximum Water Thickness Equation (CTC Model Approach).....	43

Chapter 5 - Development of a Predictive Equation.....	48
5.1 Dimensionless Groups	48
5.1.2 Identification of the Relevant Parameters.....	49
5.1.3 Buckingham Pi Theorem Method	50
5.1.4 Identification of the Dimensionless Groups	51
5.2 Formulation of Equation	53
Chapter 6 – Test Bench Description and Correlation	58
6.1 Experimental Apparatus and Methodology	58
6.2 Cold Surface Test Bench Components.....	58
6.2.1 Charge-Air-Cooler Specifications	60
6.2.2 Test Section.....	61
6.2.3 Measurements and Sensors	62
6.2.4 Condensate Capturing Method	63
6.3 Spray Bench (Main).....	65
6.3.1 Design and Methodology of Spray Bench	66
6.4 Test Bench Correlation.....	73
6.5 Liquid Bridge Testing.....	75
6.5.1 Supplementary Experimental Setup and Methodology	75
6.5.2 Air Supply	76
6.5.3 Test Section.....	76

6.5.4 Methodology	77
Chapter 7 – Experimental Results and Discussion.....	79
7.1 Initial Sensitivity Testing	79
7.2 Comparison of 0-Degree Results with Reference Data.....	82
7.3 CAC Entrainment Testing	84
7.3.1 Effect of the Weber Number.....	86
7.3.2 Effect of CAC Angle	86
7.4 Curve Fitting	89
7.5 Liquid Bridge Testing Results	96
Chapter 8 – Conclusions and Recommendations	99
8.1 CAC Condensate Entrainment Characteristics	99
8.2 Liquid Bridge Testing Conclusions.....	100
8.3 Recommendations for future Experimental Studies	101
8.3.1 Additional Entrainment Testing	101
8.3.2 Testing at Angles Above 40°	102
8.3.3 CAC Condensate Retention Testing	103
8.3.4 Measurement of Droplet Size Distribution	104
8.3.5 Liquid Bridge Testing	104
REFERENCES	105
APPENDICES.....	112

Appendix A: Uncertainty Analysis	112
A.1 Uncertainty in Measured Parameters.....	112
A.2 Uncertainty in Calculated Parameters.....	113
Appendix B: Isokinetic Sampling	117
VITA AUCTORIS	121

LIST OF TABLES

Table 1: Relevant parameters	50
Table 2: Parameters from [18]	56
Table 3: CAC Specifications	61
Table 4: Liquid bridge air blower specifications	76
Table 5: Sensitivity testing results	80
Table 6: Variance between angles	80
Table 7: Critical Weber number for each measured angle.....	90
Table 8: Optimized equation coefficients and resulting RMSE	91
Table 9: Liquid bridge testing observations	96
Table 10: Uncertainty in measured values	113

LIST OF FIGURES

Figure 1: High pressure EGR (Left) and low pressure EGR (Right) systems [3].....	5
Figure 2: Humidity ratio of saturated air as a function of temperature [1].....	8
Figure 3: Droplet hanging at the end of the CAC fin.....	14
Figure 4: Liquid bridge between two plates [14]	15
Figure 5: Compact louvered fin heat exchanger [9].....	17
Figure 6: Various flow regimes [42].....	27
Figure 7: Droplets entrainment mechanisms in concurrent annular flow (A-D) and counter-current annular flow (E) [14].....	29
Figure 8: Variation of Θ with Bo number for ethylene glycol drops [17]	37
Figure 9: Condensate retention on several exchangers [22]	43
Figure 10: Film thickness for several of the coils.....	45
Figure 11: General nature of model	45
Figure 12: $1/y$ vs $1/x$ for several coils (Data adopted from [22]).....	47
Figure 13: Droplet entrained from liquid film.....	49
Figure 14: Fraction carryover as a function of face velocity based on data From [18] ..	54
Figure 15: Fraction carryover as a function of $We-We_{crit}$ based on data from [18]	57
Figure 16: CSB honeycomb flow straightener	59
Figure 17: CSZ Dimension II model RCHS-808-4-H/WC air supply	59
Figure 18: Cold surface test bench	60
Figure 19: Outlet face of CAC used for testing	61
Figure 20: CAC housing test piece for CSB	62
Figure 21: View of CSB outlet gutter/thermocouple.....	63

Figure 22: Ransco AFM666 air flow cart	66
Figure 23: Pacer model DTA 4000 vane anemometer	67
Figure 24: Metler model PM6100 electronic balance.....	68
Figure 25: Spray bench nozzle configuration [21]	69
Figure 26: Spray bench with HX attached	70
Figure 27: Representation of Condensate with $\theta_{CAC} = 0$	71
Figure 28: Magnetic protractor fitted to spray bench	72
Figure 29: Correlation between results from both test benches.....	74
Figure 30: Liquid bridge viewing test piece	77
Figure 31: Formation of liquid bridge between plates	77
Figure 32: Liquid bridge test piece attached to air blower	78
Figure 33: Result differences in terms of dialed flow rate	80
Figure 34: Result differences in terms of the dry velocity measured.....	81
Figure 35: Result differences in terms of the Weber number.....	81
Figure 36: Comparison of results from 0° testing in terms of face velocity.....	83
Figure 37: Comparison of results from 0° testing in terms of Weber number.....	84
Figure 38: Fraction carryover in terms of face velocity	85
Figure 39: Fraction carryover in terms of Weber number	85
Figure 40: Increase in FC_0 with increasing inclination angle.....	87
Figure 41: Change in trend at 50° CAC Inclination.....	88
Figure 42: Representation of observed condensate at $\theta_{CAC} > 40^\circ$	89
Figure 43: Fraction carryover plotted in terms of the We minus the We_{crit}	90
Figure 44: Predictive curve for 0° fraction carryover.....	92

Figure 45: Predictive curve for 30° fraction carryover	92
Figure 46: Predictive curve for 35° fraction carryover	93
Figure 47: Predictive curve for 40° fraction carryover	93
Figure 48: Predictive curve for 50° fraction carryover	94
Figure 49: Optimized equation to best fit the entire data set.....	95
Figure 50: We_{crit} in terms of the Inclination Angle	96
Figure 51: Liquid bridge stretched just before breakup.....	97
Figure 52: Satellite droplet formed immediately after breakup at 9.30 m/s	98
Figure 53: Bridge is pushed along intact at low velocities	98
Figure 54: Illustration of pressure drop at tube inlet [21].....	117
Figure 55: Particles bypassing tube inlet [21].....	118
Figure 56: Droplets bypassing the towel due to the pressure rise [21]	118
Figure 57: Condensate sampling with isokinetic sampling [21].....	120

LIST OF APPENDICES

Appendix A: Uncertainty Analysis.....	111
Appendix B: Isokinetic Sampling.....	116

LIST OF ABBREVIATIONS

AC	Air Conditioner
ASHRAE	American Society of Heating, Refrigerating and Air-Conditioning Engineers
ASME	American Society of Mechanical Engineers
BSFC	Brake Specific Fuel Consumption
CAC	Charge-Air-Cooler
CSB	Cold Surface Bench
CTC	Chrysler Technical Center
EGR	Exhaust Gas Recirculation
FC	Fraction Carryover
FCA	Fiat Chrysler Automobiles
HX	Heat Exchanger
Re	Reynolds Number
RMSE	Root Mean Squared Error
OE	Onset of Entrainment
SB	Spray Bench
WCAC	Water Cooled Charge-Air-Cooler
We	Weber Number

Chapter 1 – Introduction

1.1 Motivation

Due to increasingly stringent emissions regulations, automotive manufacturers have the increasingly difficult task to lower their vehicle emissions. Therefore, they seek innovative ways to design engines capable of reaching higher fuel efficiencies without sacrificing performance. One of the key systems employed in many vehicles today to achieve better fuel mileage without sacrificing power is a turbocharger system which usually includes charge-air-cooler.

1.1.1 Condensation on Charge-Air-Cooler (CAC) Fins

Condensation will start to form if the temperature of moist air is dropped below its dew point. This can occur if the moist air meets a surface that is at a temperature equal to or below the air's dew point. Since charge air entering the CAC is hot (roughly 200 °C), it has a relatively high saturation point and can hold a larger amount of moisture than the ambient air before compression. The air then passes through the CAC fins, which are cooled to around 45 °C by the flowing coolant. This drastically reduces the charge air's temperature and ability to hold water vapor.

During regular operating conditions, if no additional water is added to the system, the charge air will never have a higher moisture content than it did when it was at ambient temperatures. Therefore, the humidity ratio of regular ambient air is not going to be high enough to cause any significant condensation. However, one of the main products of combustion is water vapor. Therefore, the exhaust gas that is produced after combustion

is highly saturated. When a technology known as exhaust gas recirculation (EGR), which is further explained in section 1.2.2, is utilized, up to 20% of the vehicles exhaust gas is recirculated and mixed with the ambient air before entering the compressor. This introduces new water to the system; hence the heated charge air will contain higher amounts of water vapor than the original ambient air did. With the charge air at this higher relative humidity, the risk of producing high amounts of condensation on the CAC fins becomes present, as they can easily be below the charge air's dew point. The amount of condensate produced is therefore proportional to the level of EGR employed. Currently, the maximum EGR is limited by factors, such as condensation, which is the focus of this thesis project.

1.1.2 Effect of Condensation in Charge-Air-Coolers

In a condition where excess condensation is generated in the CAC, there is a risk that the accumulated condensate could be entrained into the combustion chamber during high engine loads and intake air flow is high. This ingestion of a critical mass of water could lead to misfires in the combustion chamber or lead to other adverse effects which could send the vehicle into limp mode or damage the engine. This was an issue that the Ford Motor Company has recently had to address [1]. Recently, the deliberate, controlled, injection of water into the combustion chamber has become a topic of interest as there is potential to increase the efficiency and lower emissions [2]. However, this is an entirely separate scenario as the entrained water formed through condensation would likely be ingested in a large uncontrolled mass leading to undesirable effects.

1.1 Background

1.2.1 Charge-Air-Coolers

The turbocharger and the use of “engine downsizing” has become an increasingly popular strategy since the 1980s. There exist several types of turbocharger systems, but in all cases, they employ at least one compressor that is driven by the vehicles exhaust gas. This compressor serves to compress the intake air of the vehicle before it enters the combustion chamber. Compressed air has a much higher density of oxygen than ambient air hence, when this compressed intake air (i.e. charge air) enters the combustion chamber, a larger amount of fuel can be injected while maintaining a stoichiometric ratio, which produces more power during each stroke. This higher power-per-cycle means that smaller displacement engines are now capable of producing equal, or in some cases, higher amounts of power than other naturally aspirated, larger displacement engines.

In a turbocharger system, when the intake air is compressed, this also dramatically increases its temperature. In the past, air was not compressed to the levels that we see today, therefore there was not much concern that arose from injecting the unconditioned charge air directly into the combustion chamber. However, in modern systems charge air is usually passed through a CAC before it enters the combustion chamber. Without this step, the hot air could cause an undesired pre-ignition of the air-fuel mixture in the cylinders, also known as engine knock, which has very detrimental and damaging effects on engine life and condition.

CACs, known more colloquially as intercoolers, are highly effective heat exchangers capable of reducing charge air temperatures to operating temperatures in a very short amount of time before it enters the combustion chamber. CACs can either be

air-cooled or water-cooled (WCAC) and can either be placed inside or outside of the intake manifold. In the case of WCACs, coolant runs through the tubes and heat from the passing charge air is exchanged to the coolant. The effectiveness of WCACs is governed by the coolant flow rate and its temperature. Under investigation in this thesis, is a water-cooled, louvered fin heat exchanger but it will simply be referred to as a CAC.

1.2.2 Exhaust Gas Recirculation

During the power stroke of an internal combustion engine, a mixture of ambient air and fuel is combusted through an oxidation process of the fuel. The gases that are formed as a byproduct of this process are referred to as exhaust gases. It was mentioned above that it is the flow of this exhaust gas that spins the turbine that drives the turbo compressor. After this step most of the gas passes through and is treated by exhaust aftertreatment systems such as a 3-way catalytic converter. It is then ejected from the vehicle to the atmosphere.

As described in chapter 1.1, in a process known as exhaust gas recirculation (EGR), up to 20% of the exhaust gas can be purposely recirculated and mixed with the intake air before it is compressed. There exist two different types of EGR systems: high pressure and low pressure. In high pressure EGR, the exhaust gas is taken immediately from the exhaust manifold and reintroduced directly into the intake manifold, after the CAC. In the case of low pressure EGR, a portion of the exhaust gas that has passed through the compressor and the catalyst is reintroduced into the system before the compressor (see Figure 1). Therefore, the mixed gas goes through the same process of compression and cooling that regular intake air does before it enters the combustion chamber.

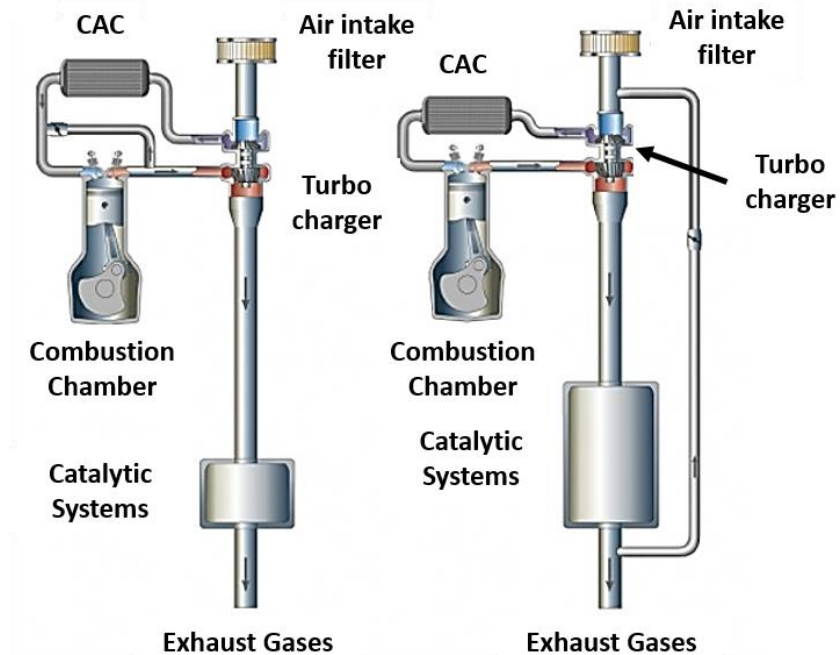


Figure 1: High pressure EGR (Left) and low pressure EGR (Right) systems [3]

The main reason EGR systems are used is because of exhaust gas' inert properties since all the combustible materials have already been used. Therefore, the exhaust gas acts to reduce the peak in-cylinder temperature during combustion by diluting the air and absorbing a portion of the heat produced. Lowering combustion temperatures leads to a lower amount of NO_x formed, an undesirable combustion emission. Lowering the peak temperatures also assists with the prevention of engine knock. When EGR is activated, the throttle valve that controls airflow to the cylinders must be opened further in order to achieve the same power as when EGR is not activated.

The brake specific fuel consumption of an engine (BSFC) refers to the amount of fuel used by an engine per unit of power produced. There exists a relationship between the BSFC of an engine and the EGR percentage. There is a critical point at which increasing EGR also dramatically increases the required fuel to produce the necessary

power. This point will vary depending on the engine, but it exists for all engines, nevertheless. Due to the degrading quality of the intake air as EGR is increased, there is a limit to the amount of exhaust gas that can be mixed with intake air, since enough oxygen must still be present to ensure proper combustion. There exists a trade-off between the BSFC of an engine and the amount of EGR employed. However, the maximum amount that could theoretically be used is still higher than the maximum that is currently used in industry.

1.2.3 Moist Air Fundamentals

Since this thesis deals with the formation of condensation through the cooling of charge-air, some of the fundamentals of moist air are presented in this section.

Moisture is always present in atmospheric air in the form of water vapor. The amount of water vapor on a per-mass basis (i.e. kg_{water}/kg_{dry_air}) is known as the humidity ratio (ω).

$$\omega = \frac{m_{water\ vapor}}{m_{air}} \quad (1)$$

Another way to specify the amount of water vapor in a mixture is by using the partial pressure of the vapor (P_v). The partial vapor pressure is, conceptually, the contribution of the water vapor to the total pressure. Humidity ratio and vapor partial pressure are related by equation 2:

$$\omega = \frac{0.622P_v}{P - P_v} \quad (2)$$

Or, rearranged:

$$P_v = \omega P 0.622 + \omega \quad (3)$$

Where, P is the total pressure and 0.622 is the ratio of the molecular mass of water and of air.

The ratio of the amount of water vapor that air contains to the maximum amount that it could theoretically hold for a given temperature and pressure is known as the relative humidity (φ) and is expressed as a percentage. When the relative humidity is at 100%, the air is considered fully saturated. Using the vapor partial pressure, it can be expressed as:

$$\varphi = 100 \frac{P_v}{P_{v.sat.}} \quad (4)$$

Therefore, it is necessary to determine the partial pressure of the water vapor, as well as the partial pressure of the water vapor in a condition where the mixture is fully saturated. Because the partial pressure of the water vapor when the mixture is saturated equals the saturation pressure of water at the mixture temperature, equation 4 can be rewritten as:

$$\varphi = 100 \frac{P_v}{P_{sat \text{ at } T}} \quad (5)$$

To determine the saturation pressure of water, one can use steam tables. Otherwise, it can also be calculated using the Antoine equation [4] to fit the saturation pressure data over a typical range, as in equation 6.

$$P_{sat}(bar) = \begin{cases} \exp\left(17.0034 - \frac{5950.3}{T + 269.21}\right), & -40 < T < 0^\circ\text{C} \\ \exp\left(12.07 - \frac{4044.0}{T + 235.56}\right), & 0 < T < 50^\circ\text{C} \end{cases} \quad (6)$$

The amount of water vapor that can be held in air depends on the air's temperature and pressure. As temperature increases or as pressure decreases, the saturation point of air increases. Although the saturation point of air is a function of both, the temperature has the largest effect on the saturation point, as seen in Figure 2.

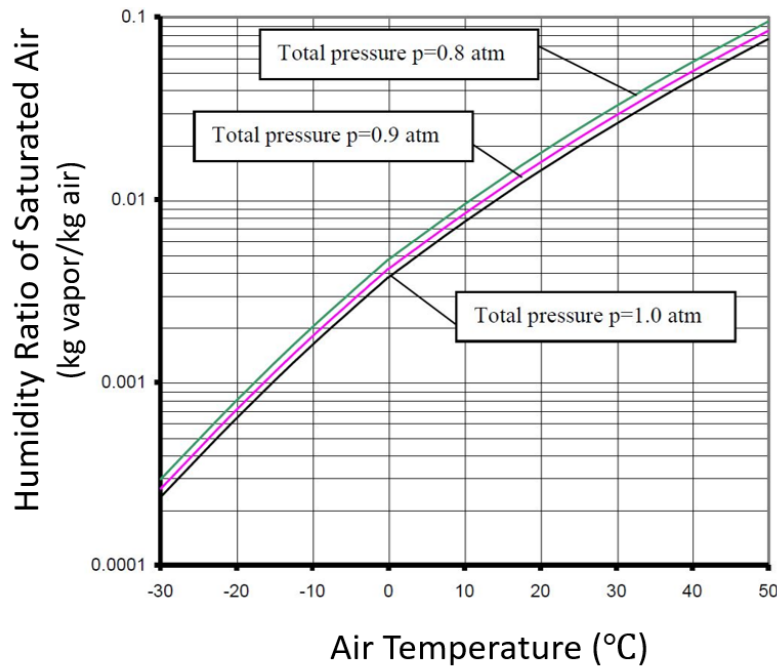


Figure 2: Humidity ratio of saturated air as a function of temperature [1]

1.2.3.A The Dew Point

The amount of water vapor that air can hold drops as the temperature of the air is dropped. Therefore, if air having a relative humidity of 50% is cooled to a certain point,

without changing the amount of water vapor present, the new relative humidity of the air might be 80%. The critical temperature where the air reaches a relative humidity of >100% is known as the dew point. Clearly, air cannot have a relative humidity of over 100%, so at this point, some of the water vapor will start to drop out of the air in the form of condensation. The dew point temperature (T_{dp}) of air depends on its humidity.

When the partial pressure of the vapor in a moist air mixture is known, the temperature at which water will start to leave the mixture and form condensation can be calculated. By solving equation 6 for the temperature, we obtain the dew point temperature, T_{dp} .

$$T_{dp}(\text{°C}) = \begin{cases} \frac{5950.3}{17.0034 - \ln(P_v)} - 269.21, & 0.0001 < P_v < 0.0061 \text{ bar} \\ \frac{4044.0}{12.07 - \ln(P_v)} - 396.15, & 0.0061 < P_v < 0.125 \text{ bar} \end{cases} \quad (7)$$

1.3 Project Objectives

The objectives of this study were to develop a correlation using dimensionless parameters to describe the drainage and entrainment of condensate within an automotive charge-air-cooler under condensing conditions at steady state. The effects of the charge-air flow face velocity (V_{face}) and angle of inclination (θ_{CAC}) of the heat exchanger were considered. Few studies have been conducted regarding condensation retention and entrainment in CACs and it appears that there exists no information on the effect that the HX inclination angle has on the amount of condensate that is entrained by the air flow, known as fraction carryover (FC). As noted later in the literature review, there exist a few models available in literature that pertain to this phenomenon. ElSherbini and Jacobi's model [5], is the most relevant as it predicts the retention of condensate on plain-fin heat

exchangers however, it is limited to cases with plain fins and assumes that there are no liquid bridges present. A few other models have also been developed such as Wang *et al.*'s model [6] to describe the entrainment of droplets in churn flow. Although the flow within a CAC is not a churn flow, the findings of this model demonstrate that the Weber (We) number is the appropriate dimensionless parameter to describe the entrainment of droplets by the airflow. This is further supported by other analyses such as the one by Kim and Peterson [7].

A model able to predict the thermodynamic effects of the retained condensate on the air-side heat exchanger performance was previously developed by Fiat Chrysler Automobiles (FCA) and is currently being used as a predictive tool. This model uses the ambient conditions to predict the total amount of condensation that should theoretically be formed and its effect on the thermodynamic performance of the heat exchanger. However, it does not predict the formed condensate's motion and destination after it drops out of the air stream. To date, FCA has not invested much time/resources to research this topic. However, due to some growing internal concerns it has become a topic of interest. Working in conjunction with FCA's Advanced Powertrain department, this project aims to develop a preliminary framework for predicting the amount of condensation that will be entrained by the air passing through the CAC based on the We number and θ_{CAC} . This preliminary work focuses on a single charge-air-cooler model which is currently fitted on several FCA vehicles; therefore, the results are specific to its fin geometry. The work allows for expansion such that it can be applied to a wide variety of charge-air-coolers so that it may be used in conjunction with the thermodynamic model to enhance its predictive capabilities.

1.4 Outline of Thesis

The contents of this thesis are organized into 8 chapters that are laid out in the following order. Chapter 2 provides a description of the various ways condensation can behave under the influence of gravitational and drag forces on increasingly complex surfaces. Chapter 3 serves as an in-depth review of literature pertaining to this subject, as well as other related subjects that may be used to better understand condensation entrainment within a CAC. Chapter 4 discusses the current heat transfer model used by FCA and the way that it expresses the amount of condensate found within a CAC. Chapter 5 presents the method used to fit a predictive equation to the fraction carryover data. Chapter 6 provides a description of the test benches and methodologies used to perform the fraction carryover and liquid bridge testing. Chapter 7 analyzes and discusses the results obtained through the experimental testing. Finally, chapter 8 serves as a conclusion and provides recommendations for future work that should be performed on this subject.

Chapter 2 - Description of Condensation Phenomena

Prior to the formal review of literature pertaining to entrainment, the following chapter discusses the fundamental modes in which condensation droplets can accumulate and disperse on simple surfaces. The factors that make the analysis of finned surfaces complex in heat exchangers, such as those found in CACs, are examined.

2.1 Widely Spaced Plates

First, the simple case of water condensing on a single isolated flat plate is considered. The first condensate will appear in the form of multiple small droplets. Here, their shape and size will depend on the contact angle along the drop perimeter on the interface between the droplet and the plate. The contact angle is governed by a complex function of surface texture, condition, material, and coatings [8]. The contact angle is the parameter that determines the magnitude of the surface tension forces binding the droplets to the plate [9]. In this relatively simple scenario, the droplet profile can be calculated using a closed form solution of the Young-Laplace equation as developed by Ku *et al.* [10].

Droplets that form near one-another are subjected to an attractive force and may combine to form larger droplets [11]. As more droplets form, there is more opportunity for them to combine. If the plate is inclined at a certain angle, the droplets, which were originally being held in place on the plate due to the surface tension force, can reach a critical mass in which the gravitational force will exceed the surface tension force causing them to start sliding down the plate [12].

If there is a flow of gas passing over the surface, the droplets will also experience a drag force that is proportional to their face area. In a CAC, the three main forces that act on a water droplet are the surface tension forces, the gravitational forces and the drag forces induced by the passing charge-air flow.

If either the gravitational or the drag force is higher than surface tension force, the droplet will begin to slide down the plate in the direction of the resulting net force. As it slides, it can collide and combine with other droplets in its path. In a CAC, droplets will slide until they reach the end of the fin and eventually fall off. Smaller droplets might be immediately entrained by the passing airflow and blow through the CAC with the air. Other, larger droplets might be too heavy to get entrained and might simply drop and land on another fin or the bottom of the CAC. It is also possible for droplets to stay attached to the end surface of the fins due to the surface tension force, which is seen in Figure 3.

For larger droplets, the drag force can overcome the surface tension force that keeps the droplet together. In this scenario, the droplet can reach a critical condition where some of the water can get stripped from the droplet. This separated water can then either be entrained by the air flow or can deposit as another droplet [13]. Therefore, even in this very simple case, there is already a high amount of variability and uncertainty regarding exact droplet behavior within the CAC.

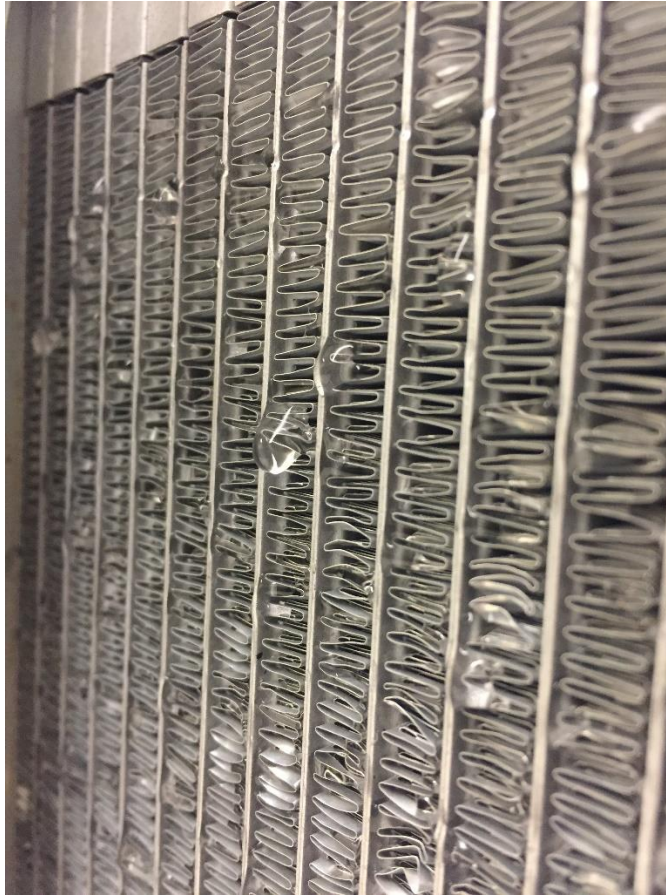


Figure 3: Droplet hanging at the end of the CAC fin

2.2 Close Spaced Plates

The analysis becomes more complex when considering multiple plates that are spaced closely to one-another. Once again, condensate droplets will begin to form on the plate surfaces. However, in this case, droplets will form on both the top and bottom surfaces of the plates. Again, these droplets will continue to grow, either by coalescing with other droplets in proximity or by sliding along the surface and combining with other droplets in its path. When a droplet reaches a critical size, there is a possibility that it will combine with another larger droplet on the bottom surface of an adjacent plate. This is what is referred to as a “liquid bridge” as seen in Figure 4. Elsherbini and Jacobi

developed a model capable of predicting the condensate retention for plain fin heat exchangers, however, the model is limited to heat exchangers with fin spacing that is wide enough so that liquid bridges will not be present [5]. The CAC under investigation uses louvered fins instead of plain fins. Moreover, due to the small fin spacing, the formation of liquid bridges is inevitable, therefore, such model cannot be used.

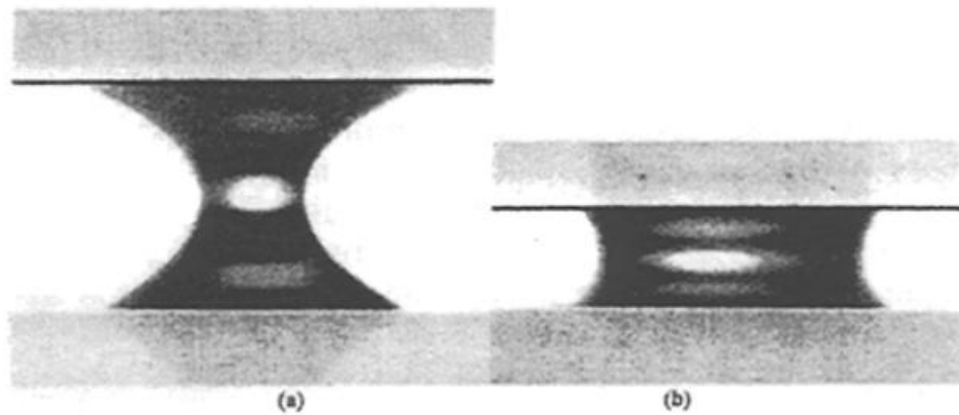


Figure 4: Liquid bridge between two plates [14]

Liquid bridges can take on a variety of shapes and because bridges are attached at both ends to the plates, they can act as a blockage for the air flowing through and increase the pressure drop between the inlet and the outlet of the passage. Like in the case of regular drops, liquid bridges will continue to grow by coalescing with other bridges or with other droplets. If the plates are on an incline, they will begin to slide down and accumulate the droplets in their path when they reach a critical mass. Once the bridge reaches the end of the plate it will drop off, in which case a portion of the bridge might drop to the bottom, remain attached to the edge of the plate or a satellite drop might be entrained by the passing airstream end exit.

When there is an airflow passing through the plates, as a liquid bridge grows and its face area increases, the drag force also increases, which can lead to multiple scenarios. One possibility exists where the drag force can overwhelm the surface tension force holding the bridge to the surfaces, causing it to slide along the channel. Again, the bridge will gather droplets in its path towards the end of the channel and may now act in any of the ways described above with the movement due to gravity. Another scenario is when the shear force overwhelms the interfacial force holding the bridge together. In such case the liquid bridge can be torn apart forming multiple smaller droplets that can either be entrained by the flow [15] or retained and left to continue interacting with other droplets. Observational testing of liquid bridges was performed, and the results are described in Chapter 8 of this thesis.

2.3 Louvered fins

As mentioned previously, most automotive charge-air-coolers, including the one used in this study, are “louvered fin” heat exchangers. These are special types of fins that include small cutouts raised at a specific angle as seen in Figure 5. Louvered fins are used in compact heat exchangers to increase heat transfer by interrupting thermal boundary layer growth, which increases the convective heat transfer coefficients and reduces the air side resistance [16]. However, these louvers can also drastically complicate the way that condensate droplets form and interact with each other and other surfaces.

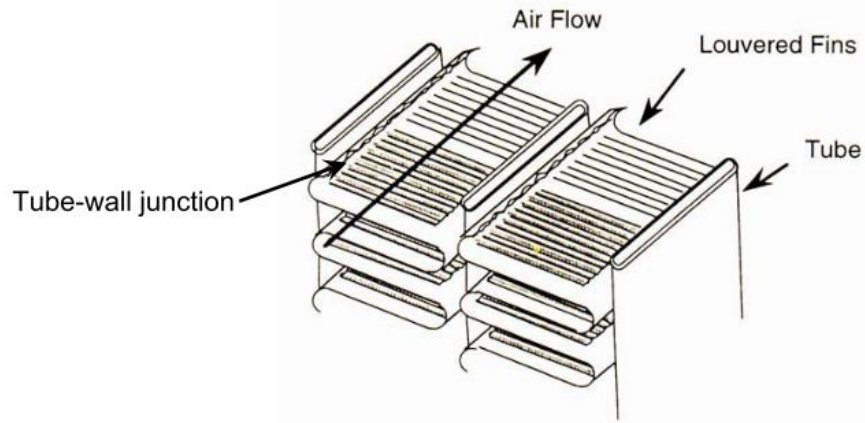


Figure 5: Compact louvered fin heat exchanger [9]

Condensate droplets can form on the fin surfaces as well as on the louver surfaces and edges. The droplets can grow and create liquid bridges that will fill the louver gaps. The shape and size of these bridges will depend on the louver pitch. Since the shape and volume of a liquid bridge depends on the spacing between surfaces [14], a smaller louver pitch can create a bridge that is more convex in shape while larger louver pitches can produce more conventionally shaped, concave bridges. Once these bridges are formed, they can start to move in multiple ways depending on the surface inclination angle and air stream velocity. Some may slide down the louver and interact with the droplets in the channel below, others may slide up the louver to interact with the droplets in the channel above or they may be pushed into the next louver opening. Of course, these droplets could also split and do all three of the actions mentioned above or any combination of them. The droplets could also be fully or partially entrained by the air stream.

The entrainment of condensation in a CAC is therefore very complex and involves several parameters that are usually unknown. Because the surface tension force depends

so heavily on the contact angle, factors such as the age and the amount of usage of the unit could have drastic effects on the reliability of any model developed to predict the entrainment of condensation. Moreover, it is nearly impossible to predict how a droplet will behave once it is formed in a CAC since there are so many pathways for droplet movement to consider. Recently, even the validity of the models developed to predict the rate of entrainment in more simple 2-phase annular pipe flow, one of the most comparable flow patterns to what occurs within a CAC, have been questioned due to the empirical correction methods used to reduce the over-predictions [17]. Therefore, any attempt to form a theoretical mathematical model capable of predicting the entrainment of condensate for a CAC will likely prove to be inaccurate.

Chapter 3 - Literature review

3.1 Lack of Available Research on this Topic

Only one technical paper was found in literature where the fraction of condensate blow off from a heat exchanger was explicitly measured [18]. At first, it may appear strange that this topic has not been studied more in depth, especially considering that air conditioning technologies have been around since the 1900s. The following section will provide an explanation for the apparent lack of research performed on the topic of condensate carryover from a heat exchanger.

Before the 1920s, sulfur dioxide or ammonia, which are harmful to the environment and humans, were used as the working fluids in refrigeration systems [19]. Therefore, ammonia systems were used solely for large commercial food freezing and other similar industrial applications where long-term human exposure was not very common [19]. This was important because if a leak was detected in the system, the entire building would need to be evacuated. If the system was used to cool spaces frequently occupied by humans, the ammonia was instead used to chill water which was then used as the working fluid in air cooling heat exchangers. This practice is still applied today [20] for large buildings. Sulphur dioxide systems were instead used in old home refrigerators. If these systems were to leak, there was a high potential for anyone exposed to get sick [20]. However, there were no air conditioning, air cooled evaporators used in conditions where the air would blow directly over humans. In the 1920s, William Carrier invented exchangers that used freon refrigerants as the working fluid, a fluid that is not lethal if

inhaled [21]. The research that then followed focused on the analysis of wet surface heat transfer and its enrichment of the heat transfer coefficient.

Later, engineers determined that above certain air velocities, the condensation formed during an evaporator's operation got entrained into the air stream. They also noticed that if the airflow was suddenly increased, the retained water would blow off in the form of large globs [21]. To fix this problem, the evaporator in most applications could simply be tilted a few degrees, the airflow could be kept below a certain critical entrainment value and the tubes were oriented so that the condensate drained most easily [22], hence solving the entrainment issue.

Since this solution has worked for most industries requiring heat exchangers, little has been invested in the research of condensate blow-off or on the development and correlation of predictive mathematical models since the early 2000s. Since then, some research has been conducted and models have been created [5], [9], [23]–[27] to describe the retention of water droplets on surface and heat exchangers. However, to produce results, exchanger geometries that include only one significant length, meaning basic plate fin exchangers that do not include louvers, with tubes recessed inside the fins have always been the focus of studies. This renders the air outlet configuration a simple row of vertical plates and the plate spacing becomes the controlling dimension. In this scenario, simple models to predict a droplet surface tension force on a plate, such as the *Two-Circle Method* [5], can be used.

In most technical papers, it appears that researchers are more concerned with the condensate retention problem than the blow-off problem. This is likely because the blow off problem is not one that is present in real evaporator installations, since they use design

guidelines that ensure there is no, or relatively little, blow off. In addition, prior to the 1970s, evaporators were mostly round tubes equipped with flat plates. Complicated designs including louvers, like those found in automotive air conditioners (AC) and CACs did not become standard until after the 1990s. Many window AC units and central air conditioning systems still utilize the flat plate on round tube design. This gives a reason as to why such little information is available about the condensate blow-off phenomena in open technical literature. Therefore, the work presented in this thesis is among the initial work on the topic of the quantification of condensate entrainment from a heat-exchanger. In addition, the heat exchanger under examination is an automotive CAC that is equipped with louvered fins on flat tubes, where there is no single known dimension that can be used to correlate the results to dimensionless groups, further complicating the phenomenon, as explained in Chapter 2.

It should be noted that increased research concerning this topic will be beneficial for all processes where condensate in a system can affect the quality of the end-product and where the intake air cannot be highly regulated (i.e. dried compressed air). It remains mostly applicable to situations where condensate blow-off can be significant and inevitable and where we are concerned with the amount of water exiting the HX with the airstream. One specific example of this case is in internal combustion engine CACs.

Recently, the Ford Motor Company has shown a large interest in the research and development on the topic of engine HX condensation. In 2012 a patent was filed (granted in 2014) for a model capable of predicting the condensation in their EGR coolers [28]. In addition, they funded a Ph.D. project that was completed in 2015, which focused on the quantitative investigation of condensation within the tubes of a CAC [1]. This is the

first study to explicitly deal with this topic. This sudden interest in this issue is likely related to the recent problems that the company has experienced relating to engine misfires that was sending some of their vehicle into limp mode in specific driving conditions. The cause of this issue was attributed to the intake of a critical mass of water of water formed by condensation in the CAC [1]. The project resulted a tool capable of predicting the rate and quantity of condensate formed in the CAC, which engineers at the Ford Motor Company can use to virtually analyze and validate different CAC designs. However, it did not study the direct relation between the dimensionless groups considering the variable parameters (i.e. the air stream face velocity) and the fraction of entrained condensate.

3.2 Effect of Condensation on heat and mass transfer

The subject of how condensation formed on a heat exchanger affects its performance regarding heat transfer is a well understood subject in which many conclusions have been drawn. In 1970, Bettanini [29] conducted several studies relating to the heat and mass transfer for vertical plates. He reported that there is an enhancement in sensible heat exchanger performance under dehumidifying conditions. He attributed this enhancement to the increase in surface roughness due to the condensation on the surface. In 1978, McQuiston determined that the enhancement in performance for plain finned-tubes was strongly dependent on the fin spacing [30], [31]. For circular-finned tubes, it was determined by Jacobi and Goldshmidt [22] that this enhancement was also dependent on the Reynolds number of the passing flow. At lower Reynold's numbers, a degradation in heat exchanger performance was observed, while with high Reynolds numbers an enhancement was present. Jacobi and Schmidt attributed their, and McQuiston's observations to condensation retention. They concluded that when the

Reynolds number is low, retained condensate would occupy heat exchanger face area, leading to a deterioration in effectiveness, while with a high Reynolds number retained condensate would be removed by the vapor shear. These findings were later supported by Uv and Sonju [32].

3.3 Condensate retention

Korte and Jacobi experimentally investigated the effects of condensation on the air-side performance of plate-fin-tube heat exchangers [33]. During these experiments real-time and steady state measurements of the condensate retention were reported for the several exchangers tested with varying fin spacing. They developed an initial model to predict the quantity of condensate retained as a function of the HX geometry, advancing/receding contact angles and air-side Reynolds number. However, it is only valid for plate-fin-tube heat exchangers with wide fin-spacings. Later, Kaiser and Jacobi [22] studied the effects of condensate accumulation and shedding on the air-side thermal performance of automotive evaporator coils. Experiments were conducted under both wet and dry conditions. They studied the condensate load up on the coils by collecting quantitative retention data both in real-time and at steady state. They determined that the greater the water mass-flux, the shorter the time required to reach steady state. Their experiments showed that the frontal velocity of the airflow had a large influence on the quantity of retained condensate at steady state.

Zhong *et al.* developed a method to characterize the water drainage from heat exchanger surfaces which they named the *dynamic dip test* [34]. The results obtained from this new test method were verified by comparing them against wind-tunnel testing. Later, Joardar *et al.* used this method to test over 30 automotive-style heat exchangers

with varying fin spacing and geometry [35]. They determined that in general, introducing an inclination to the exchanger reduces steady state retention by roughly 20%. They believe that the surface tension effects play a dominant role in water retention for high fin density coils. They also noted that the fin shape has a large effect on the retention effects. Rectangular fins tend to have over 50% lower retention compared to the same coils with triangular or straight edge louver fins. Finally, they note that the louver geometry can also play an important role in the condensate retention but that due to the absence of relevant data on this type of exchanger, no firm conclusions could be drawn. Therefore, it is expected that an automotive CAC will have a higher tendency to retain condensate and that its angle of inclination will influence the amount that is retained.

3.4 Condensate Carryover Phenomena

For the reasons mentioned previously, the understanding of condensate carryover phenomena is important not only in the automotive industry, but in many industries that employ dehumidifying heat exchangers. The ASHRAE Handbook does not provide a discussion of the mechanism of condensate carryover or the operating parameters affecting it. Rather, it provides only guidelines on how to avoid entrainment [20]. Reviewing past literature reveals very few references associated with the condensate carryover issue, and none have been found pertaining specifically to the case of an automotive CAC. The following section discusses the literature that may have some relevance in understanding which parameters and dimensionless groups dictate the process of droplet entrainment and retention within a CAC. However, it should be noted that none of the literature has explicitly explored this subject.

Mandrusiak and Carey [36] performed an analytical and experimental study of liquid shedding from the downstream edge of an offset fin matrix that did not include tubes. They introduced two Weber number parameters, which they used to characterize the presence or absence of significant liquid shedding in the matrix. However, the Weber numbers were obtained through the correlation of the geometry specific test and so are not expected to be applicable to louvered fin heat exchangers like that found in a CAC.

Brown et al. [37] performed experiments to develop an analytical model capable of predicting the trajectory of a spherical droplet placed in a uniform fluid stream. Because the model was written in general terms, it expressed the horizontal carryover distance as a function of free stream fluid velocity, gravitational acceleration, fluid density, coefficient of drag, vertical travel distance, droplet radius and density. Limitations of this model are that it requires the knowledge of the droplet release elevation and the droplet diameter.

Hong [38] developed a model to predict carryover for which he assumed that the droplets were being entrained from a liquid film that covered the film surface. The Brown et al. model was included to predict the droplet trajectory. However, no experiments were performed to validate this model.

Min and Webb [18] investigated the condensate carryover phenomena in dehumidifying heat exchangers. This is the only available literature that directly pertains to the measurement of entrained condensate. During their experiments they used two separate wavy finned-tube coils with the fin surfaces treated in such a way that one would provide a low and the other a high receding surface contact angle for the water droplets (10° and 70° respectively). The objective was to determine the effect of the contact angle on the retention and carryover of the condensate formed in a heat exchanger. They

observed that as the frontal velocity increases, the quantity of condensate carryover increases and that it is blown further away from the coil. They noted that the receding contact angle on the fin surface is a key factor for controlling the condensate carryover characteristics. The coil with the lower receding contact angle showed significantly less carryover than the one with the higher contact angle, meaning that the fraction of retained condensate is higher with lower contact angles. In addition, they observed that numerous liquid bridges were formed in the coil with the higher receding contact angle while few were seen for the lower receding contact angle coil. They concluded that the dominant carryover results from droplets formed from bridged condensate. In other words, high entrainment should be expected in heat exchangers that promote the formation of liquid bridges.

3.5 Mechanisms for Droplet Entrainment

3.5.1 Entrainment from Two Phase Liquid-Gas Flow

Although literature pertaining directly to CACs is limited, it is possible to draw similarities between droplet entrainment within a CAC and a more common phenomenon such as two-phase gas-liquid flow within a pipe. This is a vastly studied subject since it is commonly encountered in many industrial applications such as the petroleum, civil and nuclear sectors. This sort of comparison is especially applicable since it is assumed that the water found in a fully saturated CAC forms as an even layer of a certain thickness along the heat exchanger fin as data in multiple studies [5], [8], [15], [22], [24], [26], [39]–[41] is presented in terms of water mass per unit area.

Various types of two-phase flows within a pipe can exist, known as flow regimes or patterns, illustrated in Figure 6. At low air flow velocities, the closest flow regime that approximates the water film in a CAC is a stratified smooth regime. However, as the difference in velocity between the liquid film and the flowing gas is increased, the regime will shift from stratified smooth to stratified wavy. Once the difference in velocity reaches a critical point, droplet entrainment from the water film to the gas stream will begin to occur shifting it to a sort of annular flow pattern. This point at which entrainment begins is referred to as the onset of entrainment [42].

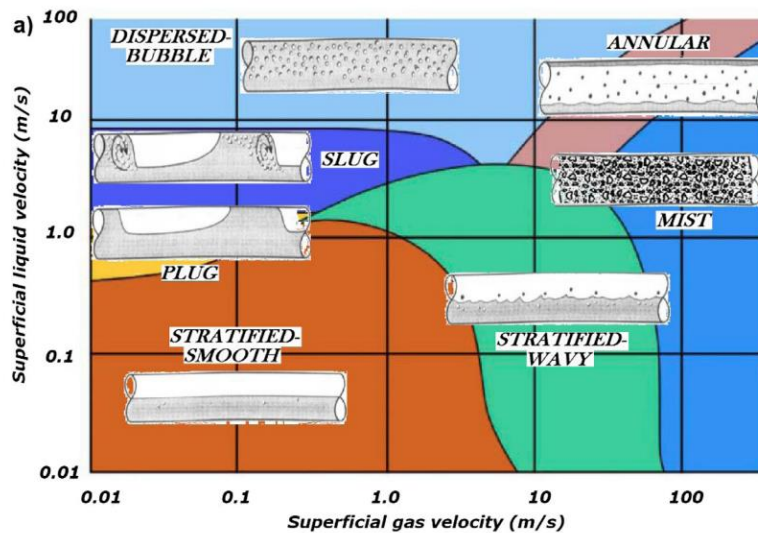


Figure 6: Various flow regimes [42]

3.5.2 The Onset of Entrainment (OE)

As the difference in velocities between the passing air flow and liquid film increases, waves will start to form on the interface. From these waves, droplets are sheared and entrained by the stream. Critical gas and liquid velocities govern the condition at the OE. Once entrainment begins, there is a continuous exchange of mass, momentum and energy between the water and the air, meaning that not only will droplet

entrainment occur, but a phenomenon known as droplet deposition, in which droplets are deposited on the film occurs simultaneously [42]. The flow is considered a fully annular flow once the mass flow rate of entrained droplets is equal to the mass flow rate of deposited droplets.

It is a force balance that governs the deformation mechanisms in the gas-liquid interface. The hydrodynamic and surface tension forces govern the motion and deformation of the disturbance waves. Under certain conditions, the force balance will cause an extreme deformation of the interface on the waves found on the liquid film and causes a portion of the wave to breakup into several liquid droplets. These droplets then get entrained by the passing airflow. There exist five different mechanisms in which droplets can be entrained by the gas: roll wave, wave undercut, bubble bursting, liquid impingement and liquid bulge disintegration, and they can be seen in Figure 7 [15]. Since this investigation is pertaining to the entrainment from a film of water on the fins inside a CAC, the fluid in question has a low viscosity. Therefore, the dominant entrainment mechanism is the roll wave, but in some cases the wave undercut mechanism can also be observed for low liquid Reynolds numbers [42].

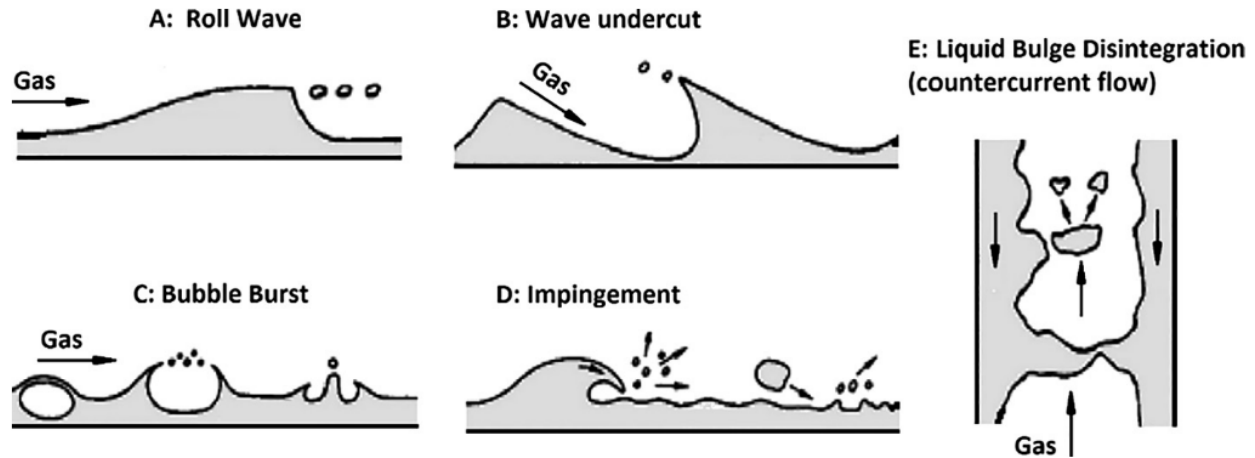


Figure 7: Droplets entrainment mechanisms in concurrent annular flow (A-D) and counter-current annular flow (E) [14]

As the gas velocity increases, the interface will grow increasingly unstable and interfacial waves will appear as a result of the Kelvin-Helmholtz instability [42]. Once the gas flow reaches a high enough velocity, the interfacial waves will begin to transform into larger amplitude roll waves. Beyond this point, the interfacial shear force created by the passing air flow will dominate over the surface tension force keeping the wave together and entrainment will occur.

According to Berna et. al, one of the factors dictating the critical condition for entrainment to take place is the liquid film Reynold number [42]. Due to varied findings in the literature, the onset of entrainment Reynolds number, Re_{lfoe} , does not have a firmly established value. However, the results of investigations performed by several authors has established that for horizontal flows, it lies somewhere between 100 and 400, and for vertical downward flows it is around 2, depending on the author [42]. Some of the first authors to study the Re_{lfoe} were Ishii and Grolmes [15]. They proposed that the critical

liquid velocity corresponds to a liquid film Reynolds number of 160. They also proposed that for conditions where the liquid Reynolds number is below 160, no entrainment takes place due to the suppression of disturbance waves on the film. One of the most recent expressions to calculate the critical Reynolds number for the onset of entrainment was proposed by Owen [43] and it is as follows:

$$Re_{lfoE} = \exp \left(5.8405 + 0.4249 \frac{\mu_g}{\mu_l} \left(\frac{\rho_l}{\rho_g} \right)^{0.5} \right) \quad (8)$$

Where, μ_g and μ_l are the viscosity of the gas and liquid respectively and ρ_g and ρ_l are the densities of the gas and liquid respectively.

However, the experiments performed to determine this expression were all carried out at near atmospheric pressure.

Later, Sawant et al. [27] performed tests at higher pressure conditions such as 1.2, 4.0 and 6.0 bar, with pipe diameters ranging from 0.94 to 12.5 cm and liquid viscosities ranging from 1 to 24 x 10⁻³ Pa-s. They concluded that the previous non-dimensional numbers did not appropriately predict the pressure effects and density ratio changes in their data. They used the viscosity number, N_μ , a dimensionless number comparing the viscous force induced by the internal flow to the surface tension force of the liquid and performed tests and proposed a new correlation for the Re_{lfoE} ,

$$Re_{lfoE} = 13N_\mu^{-0.5} \quad (9)$$

Where the viscosity number is determined as follows,

$$N_\mu = \frac{\mu_l}{\left(\rho_l \sigma \sqrt{\frac{\sigma}{g \Delta \rho}} \right)^{\frac{1}{2}}} \quad (10)$$

Where, μ_l , ρ_l and σ are the liquid viscosity and density and surface tension respectively, and $\Delta\rho$ is the pressure difference within the pipe.

The droplet entrainment process will only begin to occur under high gas velocity in the critical condition such that the Re number of the liquid film is greater than the onset of entrainment Re number (i. e. $Re_{lf} > Re_{ffOE}$). In addition, they determined that there is also a critical gas velocity below which no entrainment is possible for any liquid flow rate [15]. In other words, even if the Re number is high enough for disturbance waves to be present, there also exists a critical gas velocity ($U_{g,min}$) above zero at which no entrainment will occur.

3.5.3 Droplet Entrainment Inception Velocity

The onset of entrainment Reynolds number that was discussed in the previous section, is the parameter indicating the limiting value for whether entrainment can occur in terms of the liquid film. However, this value is independent of the gas flow conditions and does not indicate the critical gas velocity at which entrainment will begin to take place if the Re_{lfOE} is above the critical value. This critical flowing gas velocity is what is known as the entrainment inception velocity [42]. The critical inception velocity is the critical gas velocity above which entrainment from the liquid film can take place. The most widely used method for predicting the entrainment inception velocity is the Kutateladze criterion and the Ishii and Grolmes model [15].

3.5.4 Kutateladze Criterion

Although there is a high amount of work that has been performed on the inception velocity for two-phase flow, in most cases, the work dealing with gas flowing over a pool

or liquid film is theoretical. Epstein [42] evaluated the critical inception velocity from the Kutateladze number criterion. The Kutateladze criterion provides a constant velocity value above which entrainment will take place. It states that entrainment will occur if the Kutateladze number (Ku) is equal to or greater than 3.1 and is written in the form of:

$$Ku^2 = \frac{\rho_g u_g^2}{\sqrt{\sigma g \rho_l}} \geq 9.61 \quad (11)$$

Where, u_g is the gas velocity required to meet the Kutateladze criterion.

If equation 11 is rearranged, the critical air flow velocity for entrainment can be expressed as,

$$u_g \geq \sqrt{\frac{9.61 \sqrt{\sigma g \rho_l}}{\rho_g}} \quad (12)$$

It is also important to note that the Kutateladze number can also be written as a Weber number.

$$Ku^2 = \frac{\rho_g u_g^2}{\sigma} \sqrt{\frac{\sigma}{g \rho_l}} = \frac{\rho_g u_g^2}{\sigma} l_{interf} = We_{interf} \quad (13)$$

Where, $l_{interf} = \sqrt{\sigma/g\rho_l}$ is a characteristic length. The We number will be used later in this thesis to formulate the correlation between the droplet fraction carryover and the air flow speed in the CAC.

The above criterion gives a constant entrainment inception velocity that depends only on the gas and liquid properties. Crowe proposed an improvement on this model in which the following three regions are considered [42].

1. *No entrainment zone.* Where the film Reynolds number is below the Re_{lfOE} , therefore no entrainment is possible.
2. *Rough Turbulent zone.* Where the liquid film Reynolds number (Re_{lf}) is greater than 1500-1750, the liquid film becomes completely rough-turbulent and the entrainment inception has a constant value, as per the model above.
3. *Transition zone.* Where the Reynolds number lies between these two values. Here the entrainment inception velocity does not have a constant value.

In case 1, where $Re < Re_{lfOE}$, the critical Kutateladze number (i.e. inception velocity) is high, therefore liquid entrainment is rare or non-existent.

The second region is characterized by a rough turbulent flow regime where the typical liquid film Reynolds number proposed is 1635. According to Crowe [44], liquid entrainment is expected to occur in this region for Kutateladze numbers greater than 3.2. Note that this is a slightly larger Ku number than the one proposed by Epstein. In this case, the equation is written as:

$$Ku^2 = \frac{\rho_g u_g^2}{\sqrt{\sigma g \rho_l}} \geq 10.24 \quad (14)$$

Which can be rearranged in the same manner as with the Epstein manner to obtain the entrainment inception velocity:

$$u_g \geq \sqrt{\frac{10.24\sqrt{\sigma g \rho_l}}{\rho_g}} \quad (15)$$

The third region, as the name implies, is a transitional region in which the Kutateladze number is sensitive to the Re number. As the Re number increases, the Ku and therefore the inception velocity decreases. Berna et al [42] used the proposed value of 160 by Ishii and Grolmes [15] for the Re_{lfoE} number. By using 160 as a first approximation to estimate the range of the transitional zone to $160 < Re_{lf} < 1635$. In other words, a Re number of 160 corresponds to the condition where waves will start to form and entrainment becomes possible, while the film can be considered fully turbulent at a value equal to or greater than 1635. At the lower end of the range, the critical Ku number is roughly equal to $Ku \approx 7.5$. If the variation in the transitional region is considered linear:

$$Ku^2 = \frac{\rho_g u_g^2}{\sqrt{\sigma g \rho_l}} \geq 61.241 - 0.0312 Re_{lf} \quad (16)$$

Rearranging, the entrainment inception velocity for the transitional region is obtained:

$$u_g \geq \sqrt{\frac{61.241 - 0.0312 Re_{lf} \sqrt{\sigma g \rho_l}}{\rho_g}} \quad (17)$$

3.5.5 Ishii and Grolmes Model

When a flow is annular, there are waves present on the interface between the liquid film and the passing air flow. The difference in velocities between the two mediums dictates the shape of these waves. Ishii and Grolmes [15] concluded that there exists a lower limit for Re_{lf} under which no roll-wave entrainment can occur, known as the onset of entrainment Reynolds number (Re_{lfoE}).

When roll-waves are present on the liquid film, the flowing gas exerts a drag force, F_D , on the wave crest. Ishii and Grolmes [15] assumed that when the drag force overwhelms the retaining surface tension force, F_σ , the wave is broken and entrainment occurs. They used this force balance to derive a criterion for the onset of roll-wave entrainment. They then developed an entrainment inception velocity criterion which depends on the viscosity number and the liquid film Re number [42].

Cherdantsev [17] performed an analysis of all previously developed physically-based models developed to predict the entrainment rate in annular gas-liquid flow by comparing the model assumptions to the experimental observations. It was determined that in nearly all cases, the assumptions are not confirmed and that the results are in strong qualitative and quantitative disagreement with the experimental results. He attributes this to an incorrect hypothesis on the entrainment mechanism used and the prediction of the disturbance wave shapes not matching the experimental data. Because of this, the models yield a large over-prediction of the experimentally obtained entrainment rate by several orders of magnitude. He notes that reasonable agreement with experimental results is achieved with the use of additional empirical correction but in

doing so, the model's validity becomes questionable since any model could be made to fit the data using this method.

3.6 Droplets Subjected to Gravity and Shearing Air Forces

Liquid drops attached to vertical or inclined surfaces will adhere to the surface by means of a retentive force known as surface tension. Drops that are on the verge of sliding on inclined surfaces are referred to as critical drops. The surface tension force (F_s), which holds a critical drop can be related to the contact angle between the drop and the surface by:

$$\frac{F_s}{\sigma R} = k \cos \theta_R - \cos \theta_A \quad (18)$$

Where, k is a constant that depends on the geometry of the drop, σ is the liquid-vapor surface tension, R is a length scale representing the size of the drop contour and θ_R and θ_A are the advancing and receding contact angles, respectively [45]. There is disagreement in the literature regarding the contact angle distribution for drops and for the shapes of their contours. Because of this, the prediction of the value of k has differed by over 300%. [25].

EISherbini and Jacobi studied the parameters of critical-size drops resting on vertical and inclined surfaces [25]. Their measurements indicated that the minimum contact angle of a drop that is on the verge of motion is the characteristic receding angle of the liquid-surface combination.

They noted that at the point of incipient motion on an inclined surface, the maximum contact angle is approximately equal to the advancing contact angle of that

surface and that it is independent from the drop size or the surface inclination angle. To find the minimum contact angles at critical condition, they proposed a dimensionless parameter θ obtained as follows,

$$\theta = \frac{\theta_{min} - \theta_R}{\theta_A - \theta_R} \quad (19)$$

Where, θ_A and θ_R are the advancing and receding contact angles of the surface respectively. Figure 8 shows the variation of θ with respect to the Bond number for ethylene glycol drops of various sizes on a surface at different inclination angles.

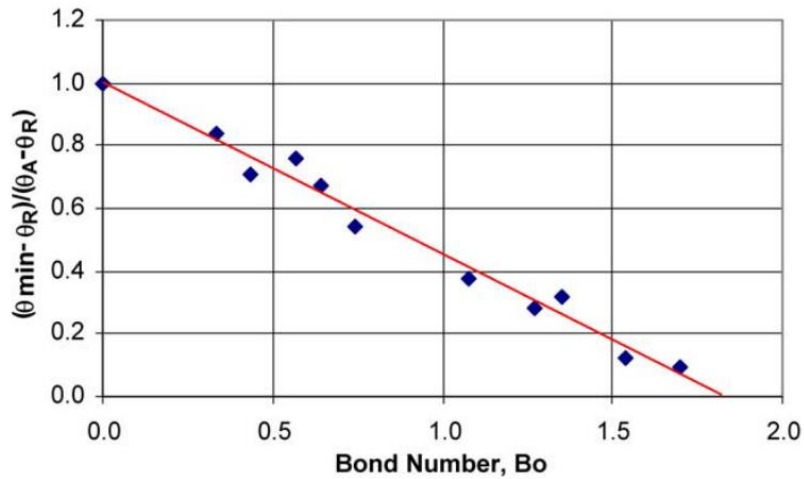


Figure 8: Variation of Θ with Bo number for ethylene glycol drops [17]

Briscoe and Galvin investigated the critical condition for the sliding of sessile and pendent droplets down a solid hydrophobic substrate [46]. They determined that for sessile droplets $\sin\alpha_c$ scaled with $V^{-2/3}$ and that for pendent droplets $\sin\alpha_c$ scaled with V^{-1} where α_c is the critical substrate angle and V is the droplet volume. They found a good agreement between experimental and theoretical values (obtained using the

Dussan equation [47]) for sessile droplets but in the case of pendent droplets, the agreement was only possible by assuming a droplet width independent of its volume.

Fan *et al.* studied the initiation of droplet motion on surfaces through a shearing mechanism generated by a controlled air flow [48]. A model was developed balancing the surface tension forces at the contact line and the drag force due to the air. It was determined that the critical velocity where motion is initiated depends on the contact angle and the droplet size. Three modes of motion were identified: 1. the droplet retains a similar footprint to the initiation of motion; 2. a tail exists at the rear of the droplet; 3. a trail remains at the back of the droplet leaving behind smaller droplets. Their model more accurately predicts motion of the first type.

3.7 Full or Partial Droplet Entrainment from a Surface

3.7.1 Liquid Droplet Entrainment from a Vertical Surface

Sommers *et al.* [11] studied the phenomena of entrainment for droplets attached to a vertical surface under the effect of a cross shear air flow force and the effect of micro channels on the retention of droplets. During their experiments, the objective was to develop a method for predicting the critical air velocity required to induce droplet departure from a vertical surface that uses only a few, easily measurable, simple parameters. These parameters included the advancing and receding contact angles, the droplet volume and the width and depth of the micro-channels, should they be present. The model they developed considers the combined effect of the gravitational, surface tension, and air flow forces on a droplet.

They proposed that in an ideal case, the calculation of the critical air flow force required for the entrainment of a droplet on a vertical surface is obtained using a three-component force balance on the droplet:

$$F_{g,x} + F_{s,x} + F_{d,x} = 0 \quad (20)$$

Which is the sum of the gravitational force, the surface tension force and the air flow force in the x-direction, respectively.

Although this model proved reasonably accurate (15.2% for 89% of droplets) for predicting the critical air velocity required for water droplet departure from a vertical fin, it only applies to droplets ranging from 1-25 μL in volume. Because the model uses only one advancing and receding contact angle, it assumes that the droplet is not a liquid bridge. Therefore, it cannot be used in conditions where liquid bridges are present, such as in a CAC.

3.8 Drag Force on a Droplet Draining Off the Outlet of an Exchanger

Lexmond and Van der Geld [49] performed experiments to identify the effect of the plate thickness on the detachment and breakup process of a droplet hanging at the end. Plates of varying thicknesses were oriented vertically with a droplet attached to the bottom as gas flowed down symmetrically downward on both sides. They concluded that the time required for breakup increases significantly as the gas flow velocity is increased. Detachment of ethanol in quiescent gas took roughly 30 ms while detachment in gas flowing at 1.1 m/s took around 200 ms. Although this might be counter-intuitive, they attribute this increased time to an increasing complexity of the break-up process. They also noted that with increasing gas velocity, more and larger satellites are formed, often

with a size more than half of that of the main drop. This results in a smaller main detached drop and contributes to the increased total break-up time.

It was also observed that if the velocity was kept constant, measurements exhibited the same trends with increasing pressure as with increasing gas velocity at constant pressure. In other words, both an increase in system pressure and air velocity resulted in a slower break-up time. This occurs because with increasing system pressure, the mass density of the gas increases, resulting in similar effects on the droplet to an increase in flow speed. They note that detachment occurs (no gas velocity) when no shape can be found that satisfies the Young-Laplace equation everywhere.

They developed a procedure to predict the main detachment diameter. First, the droplet detachment diameter at zero gas velocity ($d_{v=0}$) must be estimated using equation 21:

$$d_{v=0} = 2 \sqrt[3]{\frac{\sigma D}{4g\Delta\rho}} \quad (21)$$

Where, D is a critical length, such as the width of the channel from which the droplet is hanging.

Next, the We number must be computed based on the air flow velocity (v) using equation 22:

$$We_0 = \frac{\rho_v v^2 d_{v=0}}{\sigma} \quad (22)$$

According to their findings, if the $We > 5$, the detachment diameter will depend on the Re , while if $We < 5$, it depends on the We .

$$d/d_{v=0} = \begin{cases} 1 - CWe_0, & We_0 < 5 \\ 1 - CRe_{pl}, & We_0 \geq 5 \end{cases} \quad (23)$$

Where, $C = 0.11 \pm 0.01$ for water and the Reynolds number is determined using equation 24.

$$Re = \frac{0.003\bar{u}_g}{\nu} \quad (24)$$

Where, ν is the kinematic viscosity of the gas in m^2/s and \bar{u}_g is the mean gas velocity in m/s .

It is important to note that the models described in this chapter are discussed because they all pertain to similar phenomena to the problem at hand. If a numerical model is to be developed to describe the forces acting on the condensation formed within a CAC, it must incorporate many of the potential forces and parameters summarized in this section. Therefore, this chapter serves as a guideline for the correlation development. However, the discussed models are not explicitly used in the development of this correlation since they all pertain to their own problem and have bounds that limit their application to this investigation. Rather, the review of literature served to guide the decisions on which dimensionless groups best applied to the problem being investigated and how they could be used to correlate the CAC inclination angle and the face velocity with the fraction of condensate that is carried over.

Chapter 4 – Current Heat Transfer Model

A model to predict the effect of condensation formed in a CAC on the heat transfer effectiveness has already been developed by FCA. However, due to the complex nature of the condensate retention discussed in Chapter 2, the mathematical modeling of all condensate droplets within a CAC is not feasible. Therefore, the model treats the water found in the CAC as an equivalent liquid along the heat exchanger fins of thickness “ δ_w ”, which is the total liquid volume divided by the total surface area of the heat exchanger. The following section will describe the process used to approximate the water retained in the heat exchanger in terms of a liquid film.

4.1 Assumption of an Even Condensation Layer

In order to simplify the phenomenon, the amount of condensate present in the CAC is expressed in terms of the thickness of an even layer on the air side of the exchanger. Therefore, for a condensate of thickness δ_w covering the air side surface whose area is A_a , the mass of the condensate in the exchanger $m_{retained}$ can be obtained using:

$$m_{retained} = \rho_w A_a \delta_w. \quad (25)$$

As mentioned previously, several authors who have studied condensate retention within a heat exchanger, have presented their data in terms of a mass of water retained per unit surface area of the heat exchanger ([5], [8], [15], [22], [24], [26], [33], [34], [39]–[41]).

4.2 Formulation of Maximum Water Thickness Equation (CTC Model Approach)

In [22], Kaiser and Jacobi plotted the mass of water retained per unit air side area vs. the air face velocity for several different heat exchangers. In their experiments, the heat exchangers were mounted with the tubes running vertically. In this configuration, the fins are horizontal, meaning that the water retention will be at a maximum when there is no air velocity. The results shown in Figure 9 demonstrate an equivalent film thickness which drops off with the inverse of the air velocity.

If a water density of 1000 g/cm^3 is assumed, the thickness of the water layer in mm would be the value found on the Y-axis divided by 1000.

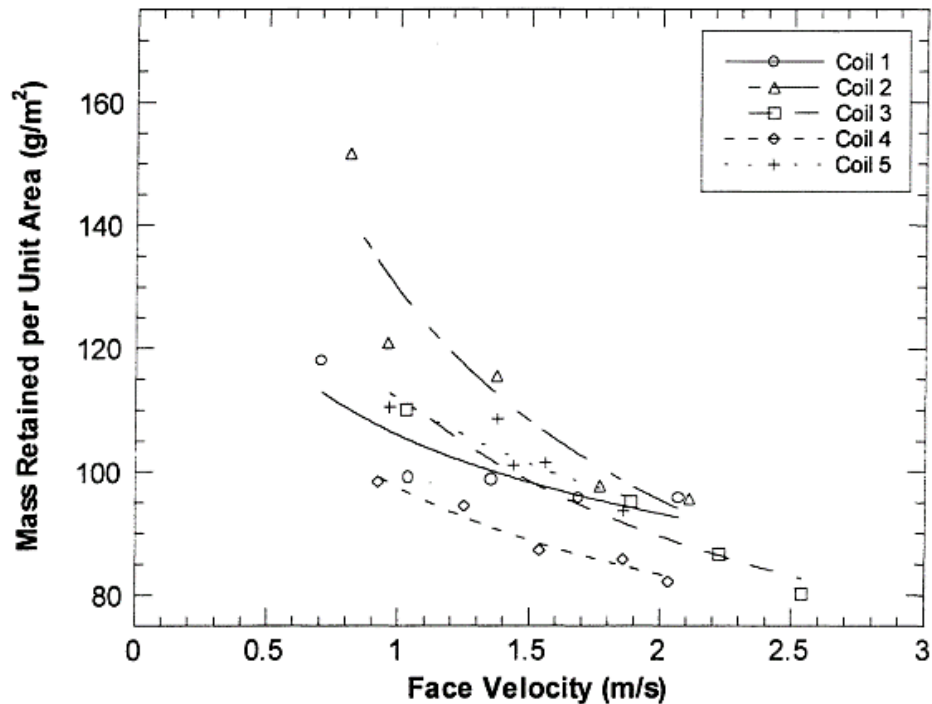


Figure 9: Condensate retention on several exchangers [22]

To formulate the equation, the asymptotic solutions to the general problem were observed. It was determined that for no air velocity, the thickness of the film is proportional to the square root of the surface tension of water times its density and for very large air velocity, the thickness should be proportional to the inverse of air density times the velocity squared [50]:

$$\delta_w = C_1 \left[\frac{\sigma}{\rho_w} \right]^{\frac{1}{2}} \quad \text{for } V = 0 \quad (26)$$

$$\delta_w = C_2 \frac{\sigma}{\left[\frac{\rho_a V^2}{2} \right]} \quad \text{for } V = \text{large} \quad (27)$$

Where, C_1 and C_2 are functions of the specific geometry of the heat exchanger, such as the fin spacing.

This can also be determined by scaling, letting “ L ” represent a significant dimension of the water retained on the heat exchanger fin [21]:

$$F_g \propto gL^3 \rho_w \quad (28)$$

$$F_\sigma \propto \sigma L \quad (29)$$

$$F_D \propto \rho_a L^2 V^2 \quad (30)$$

If the drag is over a liquid film (i.e. surface drag), then the drag force is proportional to the air momentum instead of the kinetic energy. This is equal to the mass flow rate times the velocity, which results in the same relation.

A plot of a part of the data from [22] is shown below. A blending of functions (26) and (27) is illustrated beside it.

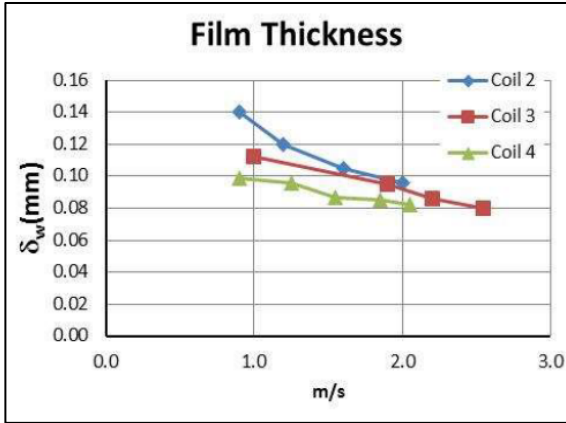


Figure 10: Film thickness for several of the coils

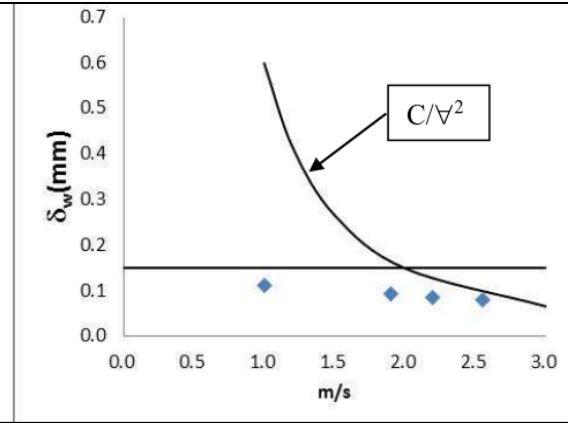


Figure 11: General nature of model

Upon initial inspection of

Figure 10, it is not immediately obvious that the film thickness approaches $\frac{1}{V^2}$ as the velocity tends to infinity. However, balancing the surface tension force against the kinetic energy demonstrates that this is in fact the correct relation. Therefore, a blended relation of the two limiting cases shown in

Figure 11 is necessary. To fit the blended function, the inverse is used.

We first set y equal to equation 26 as a function of equation 27.

$$y = \delta_w \sqrt{\frac{g\rho_w}{\sigma}} \text{ as a function of: } x = \frac{\sigma}{\rho_a V^2/2}$$

It is expected that y equals a constant when the velocity is zero and that y is directly proportional to x as the velocity approaches infinity.

To determine the functional blending of the two extremes, the inverse was plotted.

Therefore, $\frac{1}{y}$ vs. $\frac{1}{x}$ results in equation 31 as a function of equation 32:

$$\frac{1}{\delta_w \sqrt{\frac{\sigma}{\rho_w g}}} \quad (31)$$

$$\frac{\rho_a V^2}{2\sigma} \quad (32)$$

The most general blended function using the method outlined by Churchill and Usagi [51] will have the form:

$$\left[\frac{1}{\delta_w \sqrt{\frac{\sigma}{\rho_w g}}} \right]^n = C_1^n + \left[C_2 \frac{\rho_a V^2}{2\sigma} \right]^n \quad (33)$$

Where, “ C_1 ” is the intercept and “ n ” is an adjustable variable used to make the equation best fit the data. Figure 12 shows a plot of $1/y$ vs $1/x$. From this plot, it appears that setting $n=1$ gives an acceptable fit to the curve for coil 3 of the data from [22]. Using the equation for coil 3, equation 34 is obtained:

$$\frac{1}{\delta_w \sqrt{\frac{\sigma}{\rho_w g}}} = 22.061 + 0.2065 \frac{\rho_a V^2}{2\sigma} \quad (34)$$

Although they have different intercepts, the lines for the other coils appear to follow the same general form.

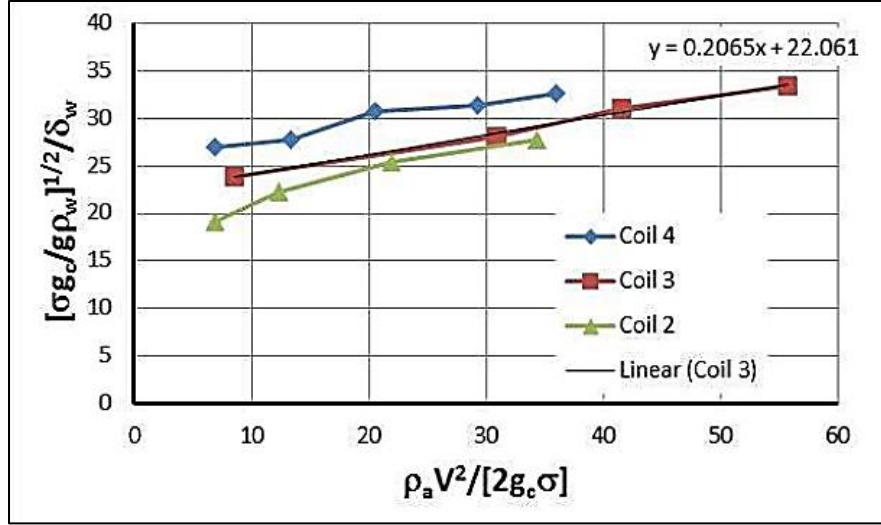


Figure 12: $1/y$ vs $1/x$ for several coils (Data adopted from [22])

Solving equation 34 for the water thickness, the following equation is obtained:

$$\delta_w = \frac{\sqrt{\frac{\sigma}{\rho_w g}}}{22.061 + 0.2065 \frac{\rho_a V^2}{2\sigma}} \quad (35)$$

Therefore, the general model for the maximum allowable condensate layer thickness becomes:

$$\delta_w = \frac{\sqrt{\frac{\sigma}{\rho_w g}}}{C_1 + C_2 0.2065 \frac{\rho_a V^2}{2\sigma}} \quad (36)$$

Chapter 5 - Development of a Predictive Equation

As discussed, the process of condensation entrainment in a louvered fin heat exchanger is quite complex. Due to the complications mentioned earlier, one would conclude that predicting the forces on the water in a CAC tube to determine whether it will drain or blow off the surface using a mathematical model will not yield very useful or consistent results. There are simply too many uncertainties relating to the forces acting on each individual droplet due to the surface tension forces depending so highly on the contact angles. For this reason, this project focuses on the development of a predictive equation to determine the fraction carryover of the formed condensate using an experimental approach.

5.1 Dimensionless Groups

In order to generate a predictive equation, it is important to first develop an understanding of the parameters that are governing the process. Based on the literature, it is well established that the appropriate dimensionless groups used to describe condensate entrainment are the Weber and Bond numbers. In the following section, the Buckingham Pie theory is used to examine the case of a droplet being entrained from a layer of water by air flow passing over it to analytically explain why the use of these parameters is sensible. The steps and methods for obtaining the dimensionless groups are described in the following section.

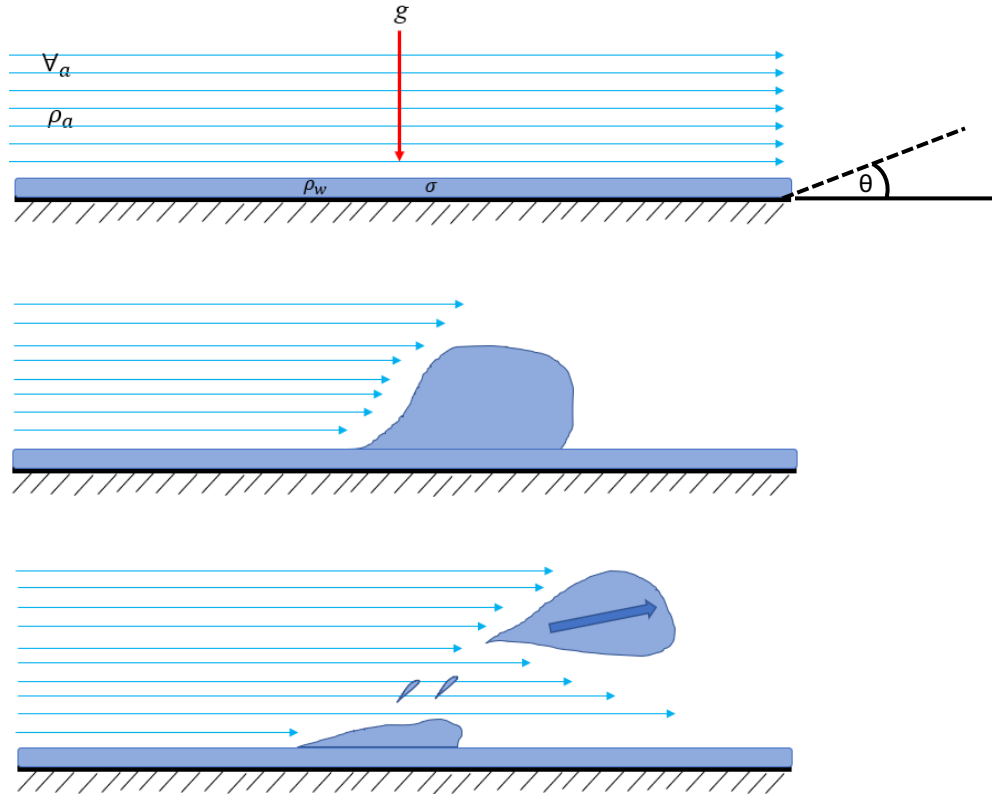


Figure 13: Droplet entrained from liquid film

5.1.2 Identification of the Relevant Parameters

The first step in determining the dimensionless groups governing the phenomena of interest is to identify all the relevant parameters involved. In the case of a droplet getting entrained from a liquid film on an inclined surface exposed to a shearing air flow, the relevant parameters and their basic dimensions are tabulated in Table 1.

Table 1: Relevant parameters

Parameter	Symbol	Base Dimensions
Velocity of the flowing air	\forall_a	Lt^{-1}
Density of the flowing air	ρ_a	ML^{-3}
Density of the droplet	ρ_w	ML^{-3}
Characteristic length of droplet	D	L
Surface tension of droplet	σ	Mt^{-2}
Gravity	g	Lt^{-2}

After identifying the parameters, droplet critical entrainment velocity (\forall) can be written as a function of the other parameters:

$$\forall_a = (\rho_a, \rho_w, D, \sigma, g) \quad (37)$$

However, to perform a Buckingham Pi analysis, the function should be rewritten in the following form,

$$f(\forall_a, \rho_a, \rho_w, D, \sigma, g) = 0 \quad (38)$$

5.1.3 Buckingham Pi Theorem Method

After identifying the relevant parameters, the theorem can be applied. The parameters are arranged in equation form and assigned an exponent to be determined as presented in equation 39.

$$a_1[\forall_a]^{b_1}[\rho_a]^{b_2}[\rho_w]^{b_3}[D]^{b_4}[\sigma]^{b_5}[g]^{b_6} = 0 \quad (39)$$

Next, they parameters are replaced with their base dimensions as shown in equation 40:

$$a_1[Lt^{-1}]^{b_1}[ML^{-3}]^{b_2}[ML^{-3}]^{b_3}[L]^{b_4}[Mt^{-2}]^{b_5}[Lt^{-2}]^{b_6} = 0 \quad (40)$$

The theorem tells us that the number of dimensionless groups that we should expect is given by the number of parameters minus the amount of unique base dimensions. Therefore, in this case, since we have 6 parameters and 3 unique base dimensions, 3 dimensionless groups are expected. In the next step, 3 equations are formed by grouping the common base dimensions:

$$M: b_2 + b_3 + b_5 = 0 \quad (41)$$

$$L: b_1 - 3b_2 - 3b_3 + b_4 + b_6 = 0 \quad (42)$$

$$t: -b_1 - 2b_5 - 2b_6 = 0 \quad (43)$$

From equations 41, 42 and 43 it can be determined that:

$$b_1 = -2b_5 - 2b_6 \quad (44)$$

$$b_2 = -b_3 - b_5 \quad (45)$$

$$b_4 = -b_5 + b_6 \quad (46)$$

Substituting these values into equation 39 yields,

$$a_1 [\nabla_a]^{-2b_5-2b_6} [\rho_a]^{-b_3-b_5} [\rho_w]^{b_3} [D]^{-b_5+b_6} [\sigma]^{b_5} [g]^{b_6} = 0 \quad (47)$$

5.1.4 Identification of the Dimensionless Groups

The dimensionless groups (π_n) are obtained by grouping the parameters with common exponents from equation 47, which yields the following:

$$\pi_1 = [\rho_a^{-1} \rho_w]^{b_3} ; \pi_2 = [\nabla_a^{-2} \rho_a^{-1} D^{-1} \sigma]^{b_5} ; \pi_3 = [\nabla_a^{-2} D g]^{b_6}$$

Therefore, the dimensionless groups obtained are:

$$\pi_1 = \left[\frac{\rho_w}{\rho_a} \right]^A \quad (48)$$

$$\pi_2 = \left[\frac{\forall_a^2 \rho_a D}{\sigma} \right]^B = We \quad (49)$$

$$\pi_3 = \left[\frac{\forall_a}{\sqrt{Dg}} \right]^C = Fr \quad (50)$$

Upon inspection of the resulting groups, one will notice that π_2 and π_3 yield the Weber number and Froude number respectively, both common dimensionless groups used in fluid analyses. The Froude number is defined as the ratio of a fluid's flow inertia to external fields, such as gravity. The Weber number is a ratio of a fluid's inertial force compared to its surface tension force. The Weber number is especially useful when analyzing droplet entrainment since a point of incipient entrainment where the drag force starts to overwhelm the surface tension force can be determined experimentally. This point is known as the critical Weber number. π_1 , which considers the ratio of the densities between the flowing air and the droplet in question, is constant.

Elsherbini and Jacobi [5] developed a model to predict the retention of droplets on an inclined plane under gravitational forces. In this model, they use the Bond number to represent the ratio of the gravitational force to the surface tension forces. It is in this dimensionless parameter that the inclination angle is considered, and it is expressed as:

$$Bo = \frac{\rho_w g D^2 \sin\theta}{\sigma_w} \quad (51)$$

Where ρ_w and σ_w are the density and surface tension of the water respectively, D is a significant length parameter and θ is the angle of inclination.

By dividing equation 49 by equation 50 or in other words, the We number by the Fr number, we obtain a dimensionless group similar to the Bo number.

The obtention of these dimensionless groups through this analysis therefore further reinforces the fact that the fraction carryover might sensibly be expressed in terms of the Weber number.

5.2 Formulation of Equation

If the condensate layer becomes greater than that of the critical thickness (refer to Chapter 4), the excess must be shed. This can either occur through draining from the CAC or by being blown through by the air flow. The amount that is blown through is known as the fraction carryover. As mentioned previously, there is very little information that can be found in the open literature pertaining to the entrainment of condensate within a heat exchanger. However, there is some information from one reference that can be used as a starting point. Min and Webb [18] performed experiments to investigate the condensate carryover phenomena in dehumidifying heat exchangers. They used two separate wavy finned-tube coils with a different surface wettability to observe the effects of the droplet contact angle as well as air face velocity on the fraction carryover and distance of entrainment. They concluded that the surface wettability, and therefore the contact angle of the droplets is the key factor controlling the carryover characteristics, but also that as

the face velocity is increased, so is the fraction carryover. The fraction carryover results for the different face velocities can be seen in Figure 14.

Although the type of heat exchanger that was used during their experiments is not the same type as the CAC, it is expected that a similar trend will be followed. Therefore, it is possible to make a preliminary estimate of what form the data collected during the experiments will take based on the data collected in [18]. Figure 14 shows a plot of the fraction carryover results compared to the face velocity of the passing air flow taken from one of the heat exchangers. Their experiments showed that increasing the air velocity does increase the fraction carryover, however the increase was not linear.

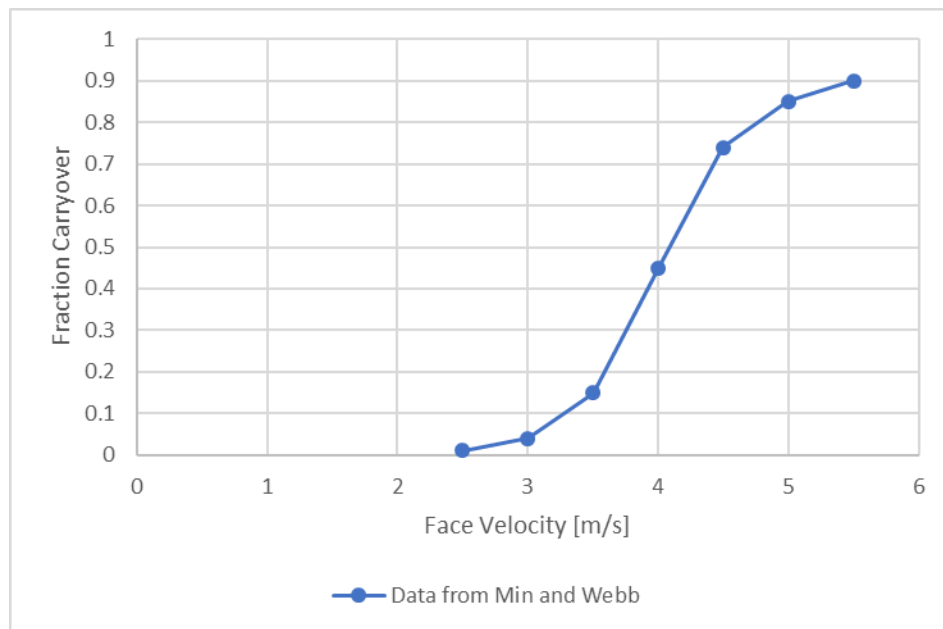


Figure 14: Fraction carryover as a function of face velocity based on data From [18]

Rather than fit a polynomial curve to this data, analyzing the asymptotes and using Churchill's blending method [51], an equation that is not bound to this data range can be

formulated. The percent fraction carryover must go to 1.0 as the air velocity goes to infinity and the function at low velocity has the form:

$$FC = aV_{face}^b \quad (52)$$

The blended function that fits will have the form:

$$\frac{1}{FC^n} = \frac{1}{[aV_{face}^b]^n} + 1 \quad (53)$$

Where “ n ” is an adjustable parameter to be determined based on the specific data set.

However, as reported in [7], [15] and [52], we should expect that no entrainment will occur until a certain critical air velocity greater than zero is reached. In other words, the fraction carryover would go to zero at a certain air velocity larger than zero. In literature, this critical velocity is usually formulated in terms of a dimensionless parameter such as the Kutateladze number (Ku), as seen in [42]:

$$Ku = \frac{\rho_a V^2}{\sqrt{\sigma \rho_w g}} \quad (54)$$

Or by a critical Weber number:

$$We_{crit} = \frac{\rho_a V_{face,crit}^2 \lambda_c}{\sigma} \quad (55)$$

Where, if a liquid film is considered, λ_c is the wavelength of the disturbances that cause waves whose peaks are picked up and made into droplets by the passing air. Since this wavelength has not been investigated for the case of heat exchangers, a characteristic length will be used instead. The HX fin spacing, or the pitch, Δ_f , will be used as this characteristic length. In that case, the Weber number is written as:

$$We = \frac{\rho_a V^2 \Delta_f}{\sigma} \quad (56)$$

Because the critical inception velocity is expressed in terms of the We [42], it stands to reason that the fraction carryover should also be expressed in terms of the We and not simply the velocity. This also ensures that the equation considers all the governing parameters such as the air density, the fin spacing, the water surface tension and the face velocity. Using the values tabulated in Table 2 , equation 57 is obtained:

$$We = \frac{\rho_a V^2 \Delta_f}{\sigma} = 0.0171V^2 \quad (57)$$

Table 2: Parameters from [18]

Parameter	Value	Unit
Air Density	1.2	[kg/m ³]
Fin Spacing	2.0	[mm]
Surface Tension	7.49 X 10 ⁻²	[N/m]

In Min and Webb's testing, the OE was found when a face velocity of roughly 2.4 m/s was reached. Therefore, the We_{cr} can be calculated using equation 55. The proper view of this is to plot the fraction carryover vs. Weber number minus the critical Weber number, which in this case is roughly 0.13.

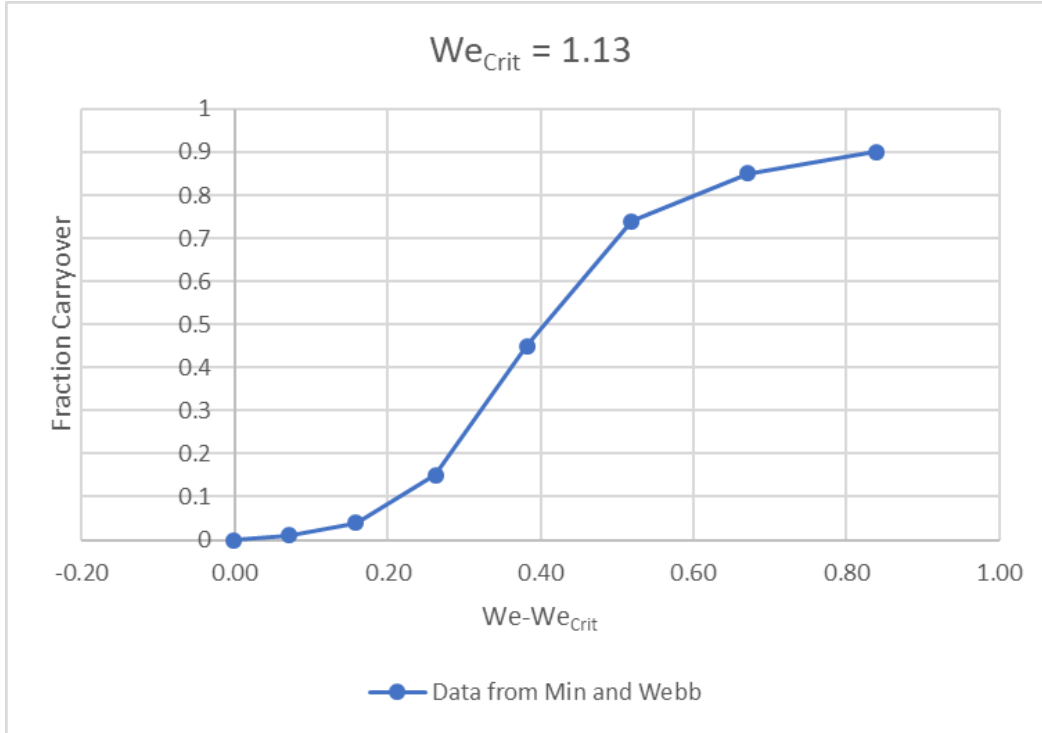


Figure 15: Fraction carryover as a function of $We - We_{crit}$ based on data from [18]

The We_{crit} imposes a second asymptote in the equation. Now the function must go to zero at We_{crit} and go to 1.0 as it tends to infinity. The blended function fitting these criteria has the form presented in equation 58:

$$\frac{1}{FC^n} = 1 + \frac{1}{[a(We - We_{crit})^b]^n} \quad (58)$$

Solving for the fraction carryover yields:

$$FC = \frac{a[We - We_{crit}]^b}{\{1 + [a(We - We_{crit})^b]^n\}^{1/n}} \quad (59)$$

Where a is a constant depending on the HX, b determines the general form of the curve (order) and n is an adjustment constant used to best fit the data.

Chapter 6 – Test Bench Description and Correlation

6.1 Experimental Apparatus and Methodology

To perform the condensate fraction carryover testing, two separate test benches were designed at the Chrysler Technical Center (CTC). Bench 1 more closely approximates the way that condensate forms within the CAC during real world operations and is therefore referred to as the *cold surface bench* (CSB). Bench 2, known as the *spray bench* (SB) was designed to facilitate testing and ensure more repeatable results. The results obtained using bench 1 were used to calibrate bench 2 and ensure that the results obtained are comparable, despite the less realistic method used to generate the condensate. After this validation, the spray bench was used to obtain most of the experimental data.

6.2 Cold Surface Test Bench Components

The CSB, seen in Figure 18, was designed to replicate the way that condensate realistically forms in a CAC during normal vehicle operations. It consists of what is essentially an open loop wind tunnel that uses an air blower and air conditioner capable of heating and humidifying the air to a requested temperature and humidity. The preconditioned air is supplied by a CSZ Dimension II model RCHS-808-4-H/WC (Figure 17), capable of supplying up to 300 CFM of air with a temperature range of 40-90 °F with a relative humidity of up to 90%. The air passes through a custom-made honeycomb flow straightener (Figure 16) before it is ducted to the CAC. It then passes through the fins of the CAC heat exchanger while cold water is run through its tubes resulting in the natural

formation of condensation on the cold CAC fins. The air then exits the CAC through the outlet face.

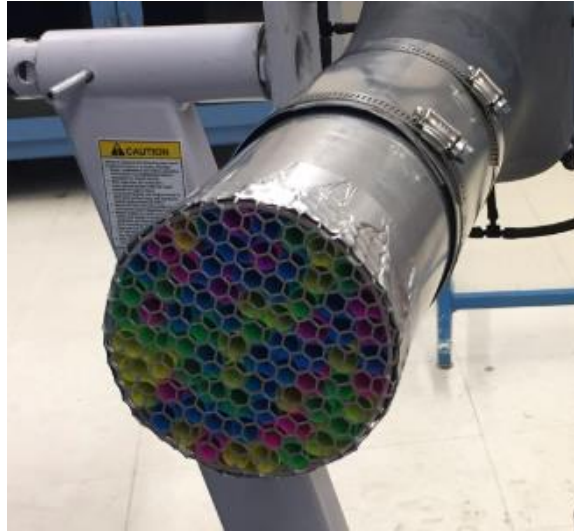


Figure 16: CSB honeycomb flow straightener



Figure 17: CSZ Dimension II model RCHS-808-4-H/WC air supply

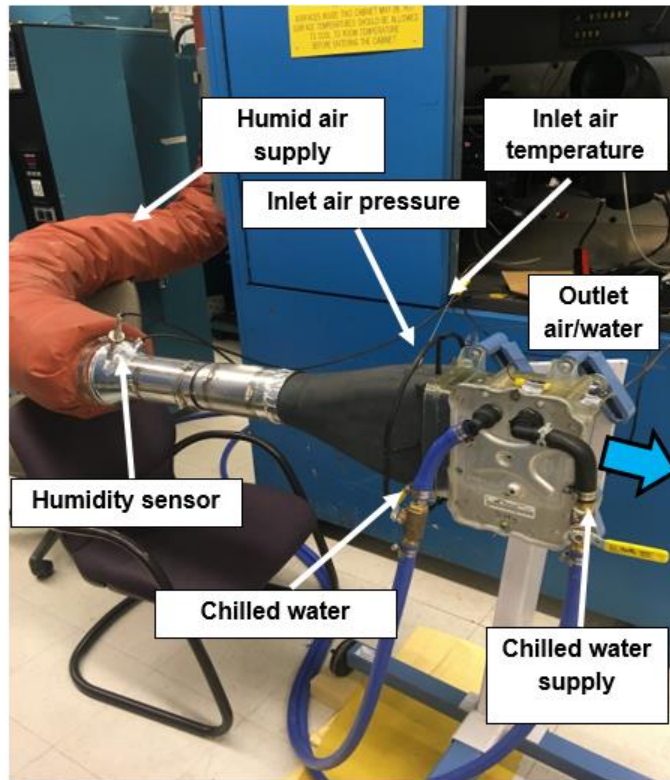


Figure 18: Cold surface test bench

6.2.1 Charge-Air-Cooler Specifications

The same charge air cooler was used for every test for both benches. It is a wavy, louvered-fin heat exchanger it is illustrated in Figure 19 and its specific parameters can be found in Table 3.

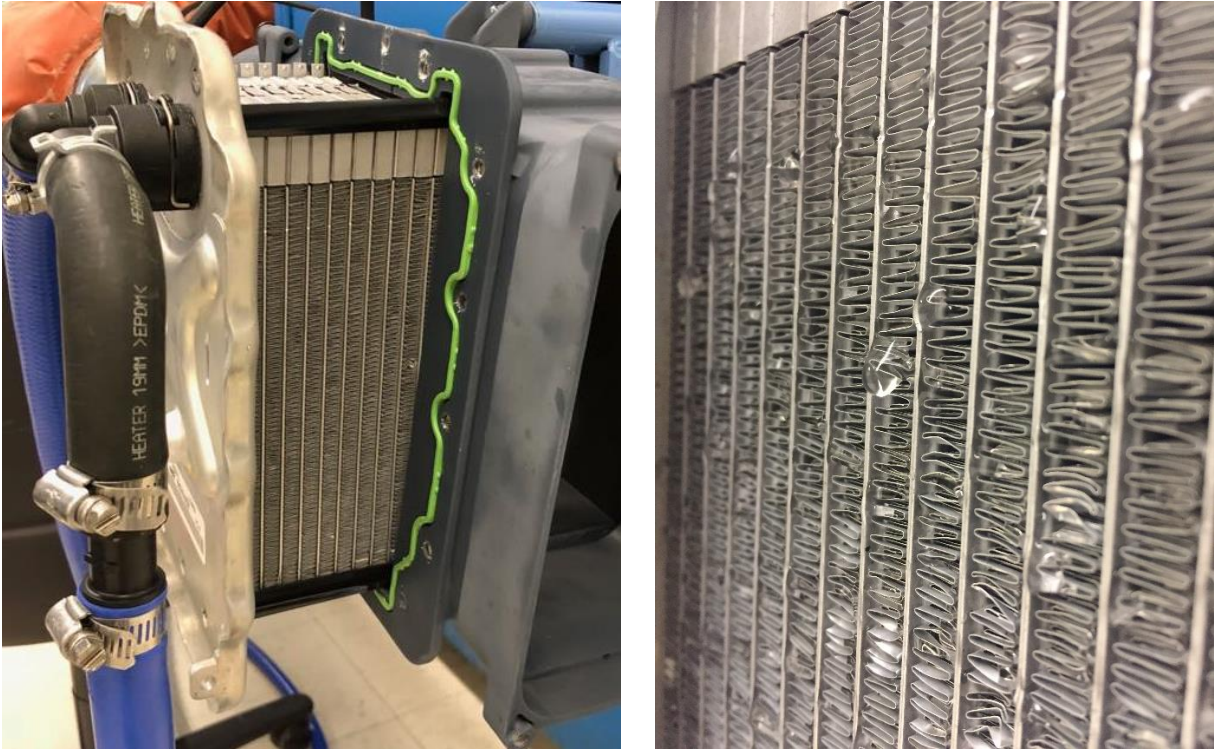


Figure 19: Outlet face of CAC used for testing

Table 3: CAC Specifications

Material	Aluminum	-
Type	Water to Air	-
Fin Pitch Δ_f	1.05	[mm]
Plate Pitch	8.2	[mm]
Plate Length	192.5	[mm]
Thickness	110	[mm]
Usage Status	New	-

6.2.2 Test Section

The test section, seen in Figure 20, was 3D printed and specially designed to mount the specific CAC used for testing. The test section is mounted to an engine stand that allows it to be set and maintained at an angle of up to $\pm 90^\circ$. The test piece is also

capable of mounting with flow meters, thermocouples and humidity sensors at its inlet and outlet.

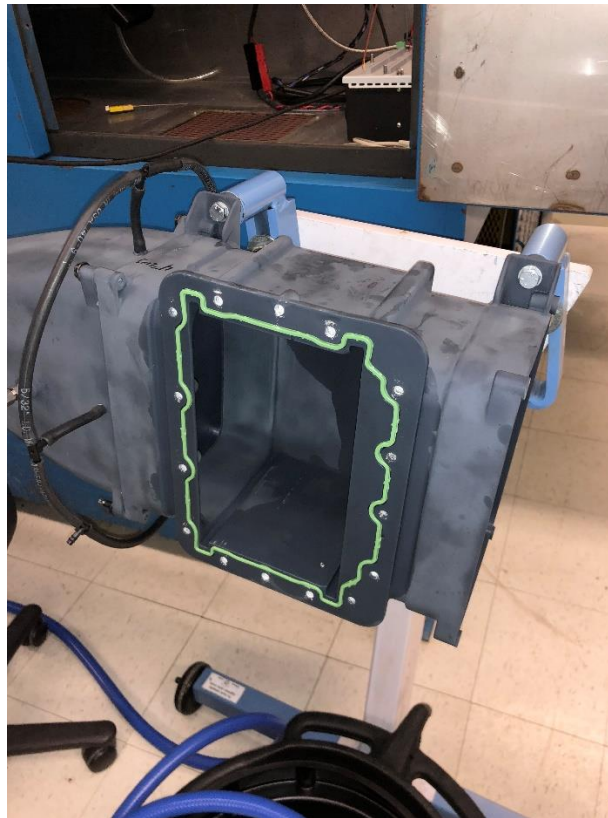


Figure 20: CAC housing test piece for CSB

6.2.3 Measurements and Sensors

To calculate the fraction carryover of the condensate, the total amount of water formed in the system for the given test period must be known. Therefore, the test section inlet and outlet are fitted with type-K thermocouples with an accuracy of $\pm 1^\circ\text{C}$, and a Vaisala model HMT338 humidity sensor with a resolution of 1% for relative humidity up to 95%. With these values, the total moisture content of the air entering and leaving the CAC can be calculated using the equations 6, 4 and 2 from Chapter 1.1.3. The difference in the two values is the amount of water that has dropped out of the air in the form of

condensation. Since the fraction carryover is directly related to the airflow speed, it is important to have an accurate measure of the air velocity. Therefore, the test section outlet is fitted with a Pacer model DTA 4000 vane anemometer with a resolution of 0.01 m/s. The flow velocity was also used in conjunction with the CAC face area to determine the mass flow rate of the air.

6.2.4 Condensate Capturing Method

The test section outlet for this bench incorporates a “gutter” to capture the condensate that drains off and the outlet face of the CAC, which is seen in Figure 21. The CAC is weighed before and after the testing to determine the amount of water that is retained within the fins. However, since the CAC is allowed to become fully saturated before the testing time starts, this value remains relatively constant for each test.



Figure 21: View of CSB outlet gutter/thermocouple

The method to determine the fraction carryover at a specific test point goes as follows.

1. The desired face velocity, humidity and temperature are set on the air supply by using the measured values from the sensor. Note that it is difficult to set the parameters to an exact value, however it is not critical that the exact desired parameters be met since it is the trend in the *FC* that is of interest. It is therefore only important that a range of face velocities be collected.
2. The system is allowed to reach steady operating conditions before starting the data collection (i.e. the air velocity, humidity and temperature fluctuations are minimized). This also allows the CAC to fully saturate so that the retained condensate holds a steady value. Note that with this bench, the stabilization time could take up to 30 minutes.
3. Once the system reaches steady operating conditions, an absorbent microfiber cloth is weighed just prior to collecting any condensate and recorded as the “dry weight”. The cloth is then held below the gutter spout for a known time (usually 20 seconds). The wet cloth is immediately weighed, and this value is known as the “wet weight”. The mass flow rate of drained condensate is then calculated using equation 60.

$$\dot{m}_{cond,drained} = \frac{m_{dr,dry} - m_{dr,wet}}{t_{collected}} \quad (60)$$

Where, m_{dr} refers to the mass of the drained condensate.

4. Step 3 is repeated, this time holding the cloth roughly 2 inches away from the outlet of the CAC to capture the condensate that is blown through with the air. The mass flow rate of entrained condensate is found using equation 60.

5. The fraction carryover can then be calculated using equation 61:

$$FC = \frac{\dot{m}_{cond,entrained}}{\dot{m}_{condensed} + \dot{m}_{cond,drained}} \quad (61)$$

Since the CAC is allowed to reach steady state, it is assumed that the retained condensate does not change through the testing for each test point. Therefore, the retained condensate is not considered.

6.3 Spray Bench (Main)

Using the cold surface bench proved to be difficult and very time-consuming as the time required for the system to stabilize was often very high. Therefore, bench 2, known as the *spray bench* was designed in a way that allowed for more efficient testing.

With the SB, the condensation is not formed within the CAC, but rather, water droplets are introduced into the upstream air using a nozzle. These droplets then enter the CAC with the air, eventually saturating the CAC in the same way that natural condensation would have. Zhong *et al.* [34] developed a method for testing the retention of condensation through the use of the dynamic dip test. They determined that whether a heat exchanger becomes saturated through the effect of natural condensation or by being saturated by submerging it in water, the retention effects and results are similar. Therefore, if properly implemented, the nozzle bench should provide results similar enough to those obtained using the CSB, especially when dealing with a fully saturated heat exchanger.

6.3.1 Design and Methodology of Spray Bench

The main components of the SB are: an air blower; a 4-inch diameter, 14 inches long plexiglass tube; and a spray nozzle. The air flow is generated by a Ransco AFM666 Air Flow Cart (Figure 22) and a commercially made test item from 1997. It uses ASME nozzles to measure the flow rate generated with a mixed flow blower and is equipped with an on-board data processing and display system. However, the HX face velocity is used for the analysis and it is directly measured using a Pacer model DTA 4000 vane anemometer (Figure 23) with a resolution of 0.01 m/s. Moving the anemometer over the face of the heat exchanger and sampling the air flow indicates an uncertainty in the air velocity of 0.1 m/s.

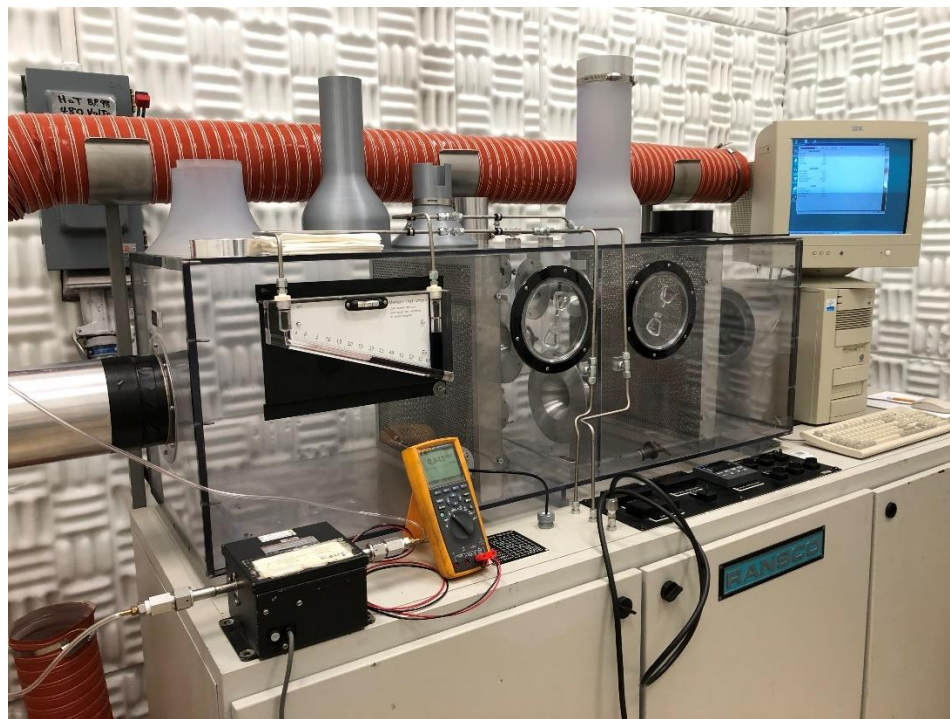


Figure 22: Ransco AFM666 air flow cart



Figure 23: Pacer model DTA 4000 vane anemometer

Similarly to the methodology outlined with the CSB, the water that drains or blows off is collected using either a microfiber absorbent cloth (for larger water flow rates, such as the water in the inlet stream and the drained water) or a lighter absorbing cloth (for the fraction that is blown off). The mass of water collected over time is determined using the same Metler model PM6100 electronic balance used with the CSB (Figure 24) with a resolution of 0.01 g. This unit was recently calibrated, so the precision uncertainty of the instrument is estimated to be ± 0.02 g.



Figure 24: Metler model PM6100 electronic balance

Several sample tests were conducted in which the collecting towels were allowed to sit in air for up to 10 seconds after collecting the water before being weighed. This was performed to determine how much of the collected water evaporates in the time elapsed between when the absorbing paper is removed from the air stream and when it is placed onto the scale. The evaporation loss consistently showed that less than 0.03 g were lost during this time. Combining this bias uncertainty with that of the scale yields a total uncertainty of ± 0.04 g for the difference in mass between the wet and dry towel, which is the water mass collected. Based on these findings, it was determined that the timing of the water collection (i.e. how long the towel is held in the air/water stream) has an

uncertainty of ± 0.1 seconds, due to the time required to get the complete towel in and out of the stream.

The spray bench configuration can be seen in

Figure 25 and Figure 26. Initially, a space was left between the plexiglass tube outlet and the CAC is so that different CACs with varying parameters could be tested with ease in the future since no proprietary test piece had to be built to mount it. However, in order to achieve the higher air velocities, it was necessary to bring the ducting right to the inlet face of the CAC, which yielded more consistent results.

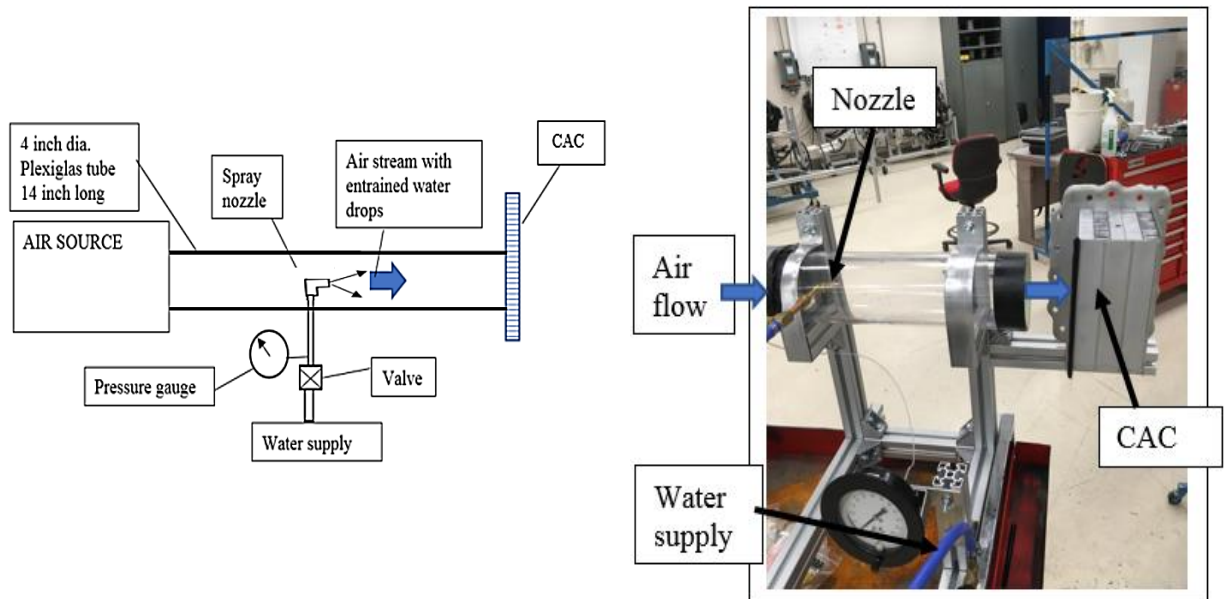


Figure 25: Spray bench nozzle configuration [21]

To properly simulate the condensation formation in the SB, it was necessary to determine the optimal configuration to get the spray from the nozzle to mix properly with the air stream to provide a reasonable, uniform deposition of water on the inlet side of the heat exchanger. Several nozzle types, positions and configurations (i.e. direction of spray) were tested before selecting the configuration seen in Figure 25.



Figure 26: Spray bench with HX attached

There is an angled metal plate installed at the outlet of the CAC with small gap left between it and the face. Any condensate that runs down the face of the CAC and falls through the gap is considered drained condensate. Condensate that is pushed by the airflow and that falls onto the plate is considered blown through. Smaller droplets that are entrained by the airflow and are blown further than the plate, are also considered blown through. This is visualized in Figure 27.

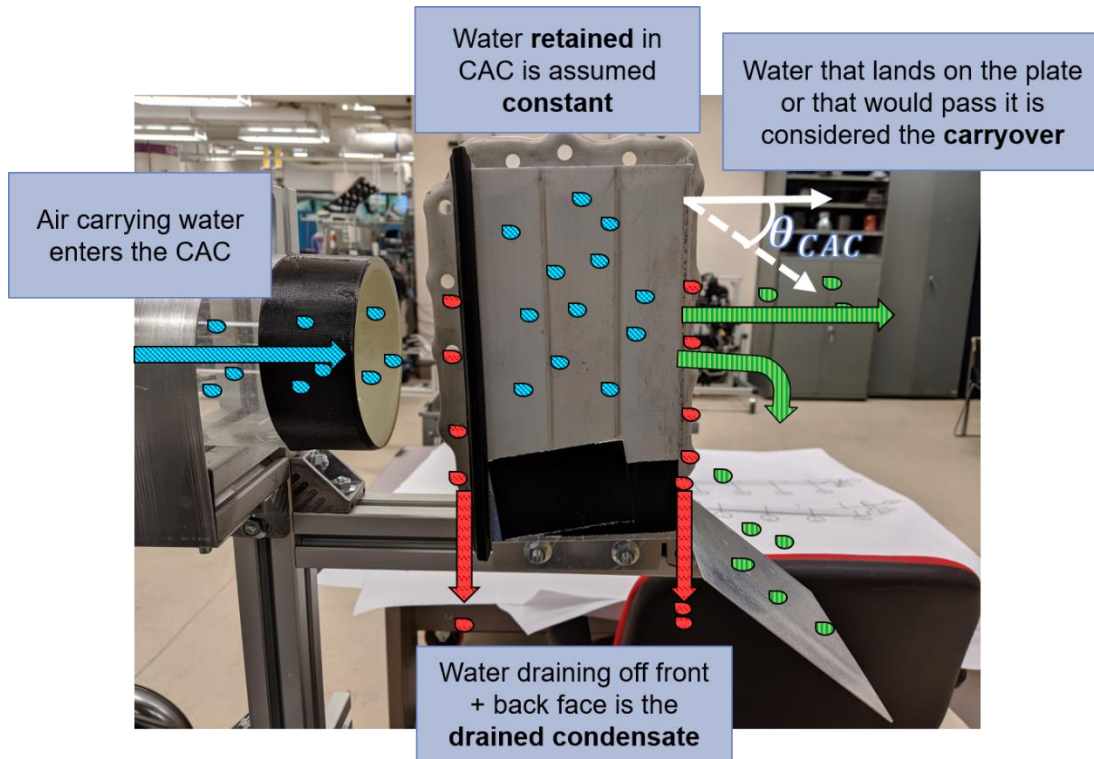


Figure 27: Representation of condensate at $\theta_{CAC} = 0$

To monitor the temperature of the air/water exiting the CAC, the same type-K thermocouple from the CSB was installed on the CAC outlet. This temperature is required to calculate the We since it affects the surface tension and air density. To set and monitor the angle of inclination of the SB, a magnetic protractor was fitted to the frame. This analog protractor divided in increments of 1° , giving it an associated uncertainty of $\pm 0.5^\circ$. The desired angle was set by tilting the entire spray bench and using foam blocks to support it. This is illustrated in Figure 28.



Figure 28: Magnetic protractor fitted to spray bench

The method to determine the fraction carryover at a specific test point for the SB goes as follows:

1. The desired air flow rate is set on the Ransco air supply.
2. With the water supply turned off, the air velocity exiting the CAC is measured and recorded using the anemometer.
3. The water supply is turned on and the system is allowed to run for around 5 minutes to properly saturate the CAC.
4. Once the system stabilizes, an absorbent microfiber cloth is weighed just prior to collecting any condensate and recorded as the “dry weight”. The towel is then held below the angled plate at the outlet shown in Figure 26 for a known time (usually 20 seconds). The wet cloth is immediately weighed, and this value is known as the “wet weight”. This amount is known as the drained condensate. The mass flow rate of drained condensate is then calculated using equation 60.

5. Step 4 is repeated, this time holding a cloth at the end of the angled plate. The amount collected is considered part of the entrained condensate. This rate is calculated using equation 62.

$$\dot{m}_{bt,1} = \frac{m_{bt,1,wet} - m_{bt,1,dry}}{t_{collection}} \quad (62)$$

Where m_{bt} refers to the mass of the blown-through (i.e. entrained) condensate.

6. Step 4 is once again repeated, this time holding a lighter absorbent cloth roughly 4 inches away from the outlet of the CAC to capture the condensate that is blown through with the air that would not land on the angled plate, these are usually very small droplets. The mass flow rate of entrained condensate is found using equation 63:

$$\dot{m}_{bt,2} = \frac{m_{bt,2,wet} - m_{bt,2,dry}}{t_{collection}} \quad (63)$$

7. The fraction carryover can then be calculated using equation 64:

$$FC = \frac{\dot{m}_{bt,1} + \dot{m}_{bt,2}}{\dot{m}_{bt,1} + \dot{m}_{bt,2} + \dot{m}_{dr}} \quad (64)$$

Again, the CAC is allowed to reach steady state and it is assumed that the retained condensate does not change through the testing for each test point. Therefore, the retained condensate is not considered.

6.4 Test Bench Correlation

The first step in verifying that the SB would provide results comparable to the cold surface bench was to ensure that the condensate behavior on the CAC is the same for both benches. On the CSB, the air flow is very uniform over the face of the CAC and the inlet ducting is sealed around the face of the heat exchanger. However, on the SB, the

air flow does not cover the entire face of the exchanger, but rather a roughly circular region of 4-5 inches in diameter. Since the purpose of these tests is to determine the ratio of condensate that is blown through compared to the total amount, this is acceptable since the region only needs to be large enough so that it contains an adequate number of fins.

Tests were run on both benches at the same velocities and ambient conditions to compare the results. In both cases, the benches had a 0° angle of inclination. The results are plotted in terms of the Weber number in Figure 29.

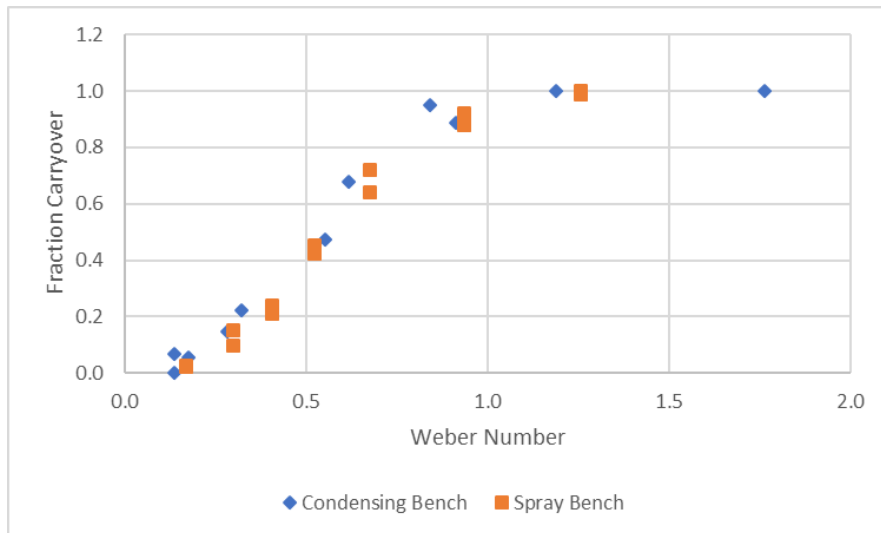


Figure 29: Correlation between results from both test benches

The tests showed a strong correlation in the results obtained by the two benches with a negligible difference.

6.5 Liquid Bridge Testing

When condensation is formed in a heat exchanger with thinly spaced fins, such as a CAC, large amounts of liquid bridges are expected to form. These bridges are then exposed to the airflow of the intake air passing through the cooler. Some aspects of liquid bridges have been studied fairly extensively, such as the surface tension forces acting on a bridge formed between two simple plates [14] or the breakage of liquid bridges through the effect of stretching the plates [53]. However, there is limited literature available pertaining to the effects of a shearing air flow on a liquid bridge suspended between two plates. If a robust numerical model is ever to be developed to accurately predict the fraction carryover from a HX in future works, it is crucial that an understanding is developed of exactly which mechanisms are forming the entrained condensate. It is assumed that a large portion of the carryover may come from the deformation of liquid bridges.

A better understanding of how liquid bridges react to a sudden airflow is beneficial to the overall understanding of the movement of condensation in a CAC. Therefore, a simple supplementary test rig was designed at the FCA facilities in Turin, Italy for the purpose of performing observational testing on liquid bridges.

6.5.1 Supplementary Experimental Setup and Methodology

A separate air flow test bench was designed and constructed for studying the motion and breakup of a liquid bridge exposed to shearing air flow. This test bench included an air blower and a plexiglass test section.

The experimental apparatus consisted of an open-loop air supply and a fabricated test section to form and examine the liquid bridge. Other equipment included a diaphragm to measure the airflow speed, a camera to capture the results and a syringe to inject a controlled amount of water in the test section.

6.5.2 Air Supply

The simple air flow test bench used for this study was over 20 years old and the make/model was not available. However, its specifications are tabulated in Table 4. Axial airflow was provided with this unit and the flow rate was controlled using a potentiometer that was correlated with a 20 mm diameter orifice plate. Flow straighteners were installed in the contraction at the blower outlet.

Table 4: Liquid bridge air blower specifications

Parameter	Range	Unit	Associated Uncertainty
Air flow	0-580	SCFM	1% on reading
Pressure difference	0-800	Pa	0.1% on reading

6.5.3 Test Section

The test section, seen in Figure 30, was designed such that it would provide easy viewing and video recording of the liquid bridge during testing. Two flat, rectangular plexiglass pieces 100 mm wide, 150 mm long and 6 mm thick were machined. Holes were drilled in each of the four corners and on one of the pieces, the holes were threaded. Fasteners were then used to attach them together. The 4 mm spacing between the pieces was controlled using metal spacers. The sides were sealed using clear tape, which could also be used to modify the inlet size of the test piece.

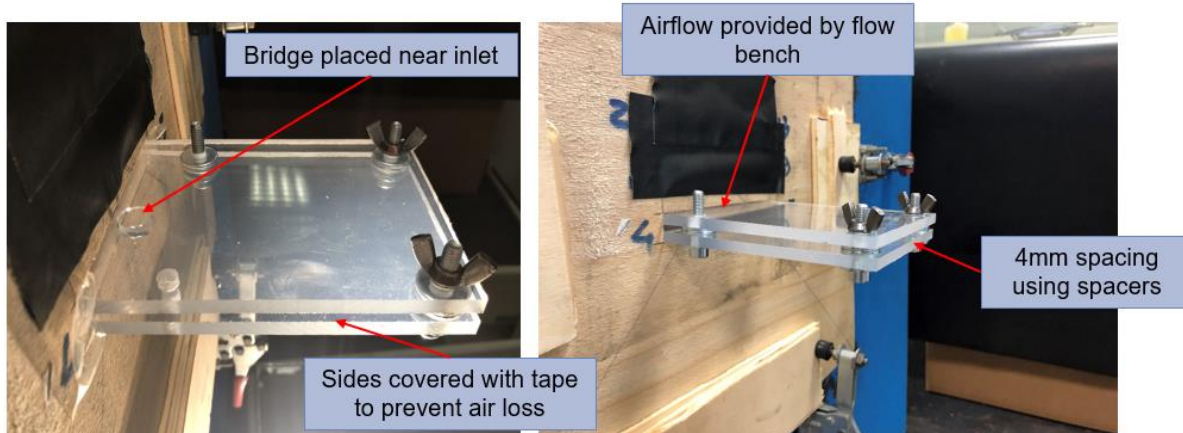


Figure 30: Liquid bridge viewing test piece

6.5.4 Methodology

To prepare the liquid bridge, a 600 μ l droplet of distilled water was placed roughly 1-2 cm away from the inlet on the lower plexiglass piece. Then the top piece was placed above. If the water did not automatically form a bridge with the top piece, the bridge was forced to form by applying a small pressure directly above the droplet on the top piece.

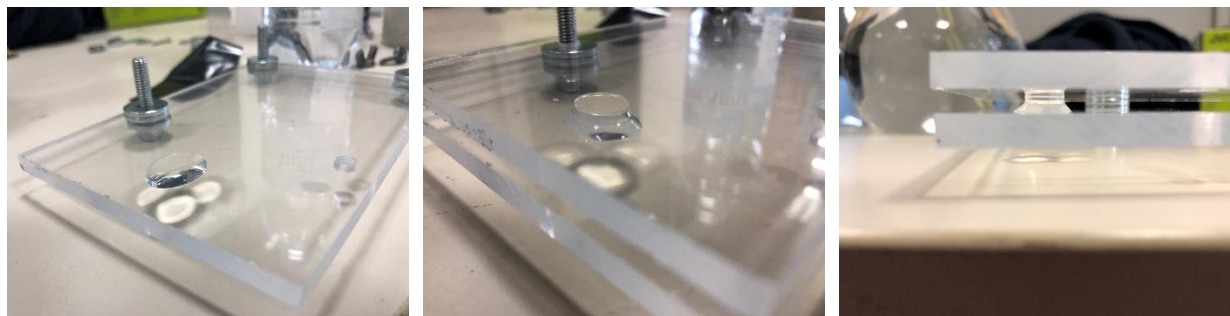


Figure 31: Formation of liquid bridge between plates

Before attaching the test piece, the blower was turned on and set to the desired air velocity and then shut off. Then, the test section was carefully placed in the custom outlet piece of the air blower, as seen in Figure 32.

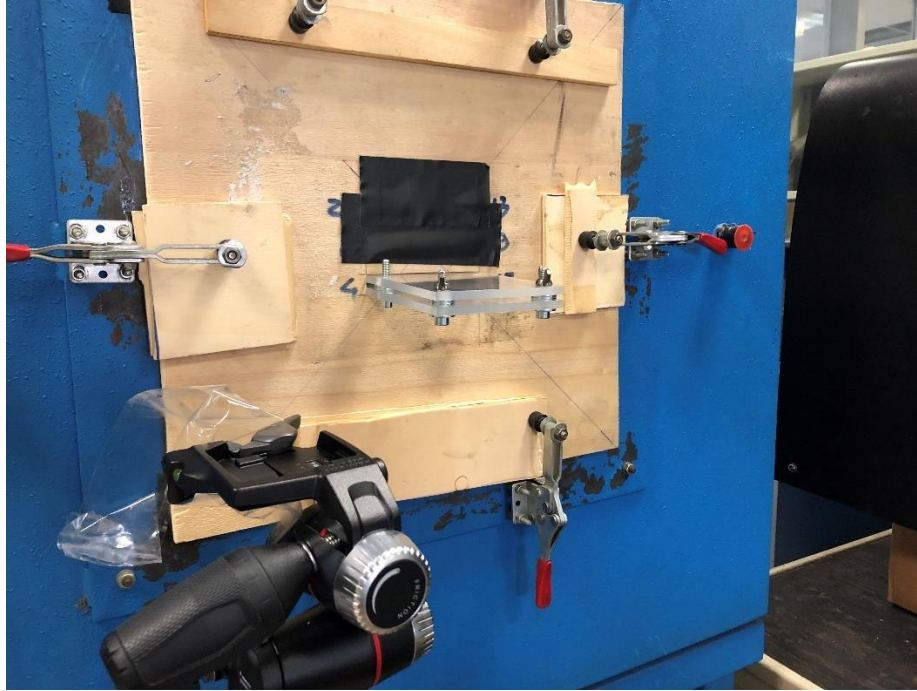


Figure 32: Liquid bridge test piece attached to air blower

Once the test piece was installed with the liquid bridge sitting properly, the camera was prepared. The camera that was used was capable of recording at 240 fps with a resolution of 1080P. This allows for limited slow-motion capabilities, but it is not adequate for very detailed slow-motion footage. This limitation was one of the reasons why a more complex test piece that simulated louvers was not used. It would have been too difficult to observe what was happening and to draw any meaningful conclusions.

Finally, the air blower was turned on and is allowed to run for roughly 5 seconds to capture exactly how the liquid bridge reacts.

Chapter 7 – Experimental Results and Discussion

After ensuring the SB produced similar results to the CSB it was decided that this bench would be used exclusively for the main portion of the entrainment testing.

7.1 Initial Sensitivity Testing

Before the systematic testing of multiple flow rates/inclination angles following the methodology described in Chapter 6 could begin, it was necessary to determine how sensitive the results are to slight, undesired variations in the inclination angle. In other words, how crucial the precision of the inclination angle is and if being off the desired angle by \pm a few degrees has a measurable impact on the results.

The FC was measured for five air flow rates with the CAC angled first at 1° then the same air flow rates were run with the angle set to 3° . The results and differences are seen in Table 5 and Table 6, respectively. Figure 33 illustrates the difference in the resulting FC depending on θ_{CAC} . Plotting them in terms of the dialed flow rate aligns them perfectly, allowing us to see the difference in terms of the same input. However, the actual velocity measured varied slightly between the tests and this is represented in Figure 34. Finally, because We is a function of the measured face velocity, it also shows the same slight variations between the 1° and 3° test points, as seen in Figure 35. These variations in velocity are quite small and so this still serves as an adequate comparison of the results.

Table 5: Sensitivity testing results

θ_{CAC} [Degrees]	Percent Dialed [%]	Airflow Dialed [SCFM]	Measured Velocity [m/s]	Weber Number	Fraction Carryover
1	53.8	300	2.06	0.07273	0.00224
	62.9	350	2.52	0.10884	0.00934
	72.1	400	3.02	0.15632	0.12407
	81.7	450	3.5	0.20996	0.20499
	91.1	500	4.05	0.28113	0.50852
3	54.1	300	2.15	0.07923	0.00238
	63.4	350	2.6	0.11586	0.00323
	72.6	400	3.12	0.16684	0.02355
	82.1	450	3.55	0.21600	0.26793
	91.6	500	3.98	0.27150	0.57799

Table 6: Variance between angles

	1°	3°	Δ
Fraction Carryover	0.00	0.00	0.00
	0.01	0.00	-0.01
	0.15	0.18	0.03
	0.24	0.30	0.06
	0.55	0.59	0.04

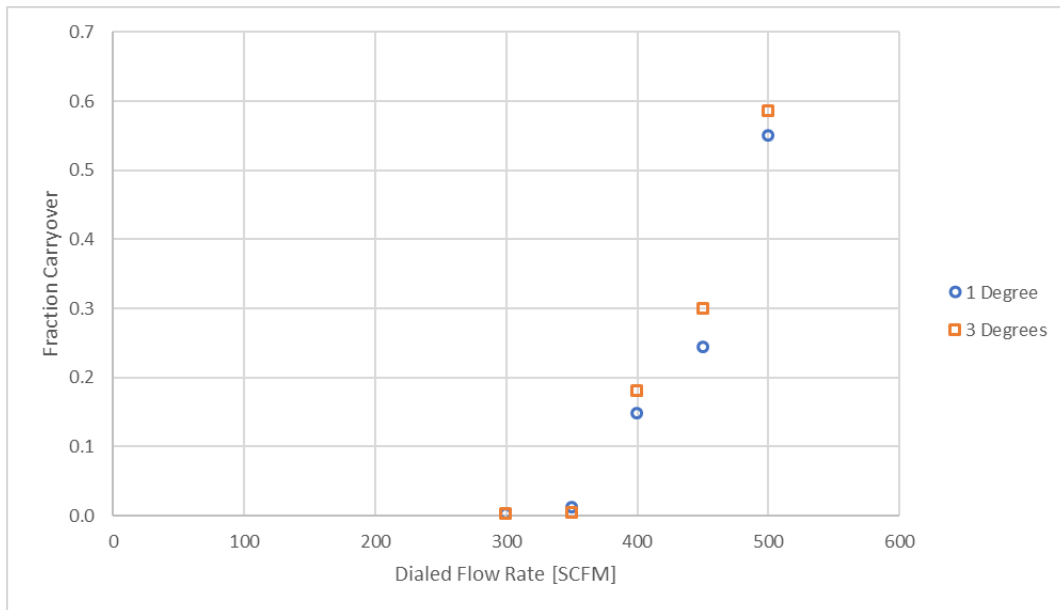


Figure 33: Result differences in terms of dialed flow rate

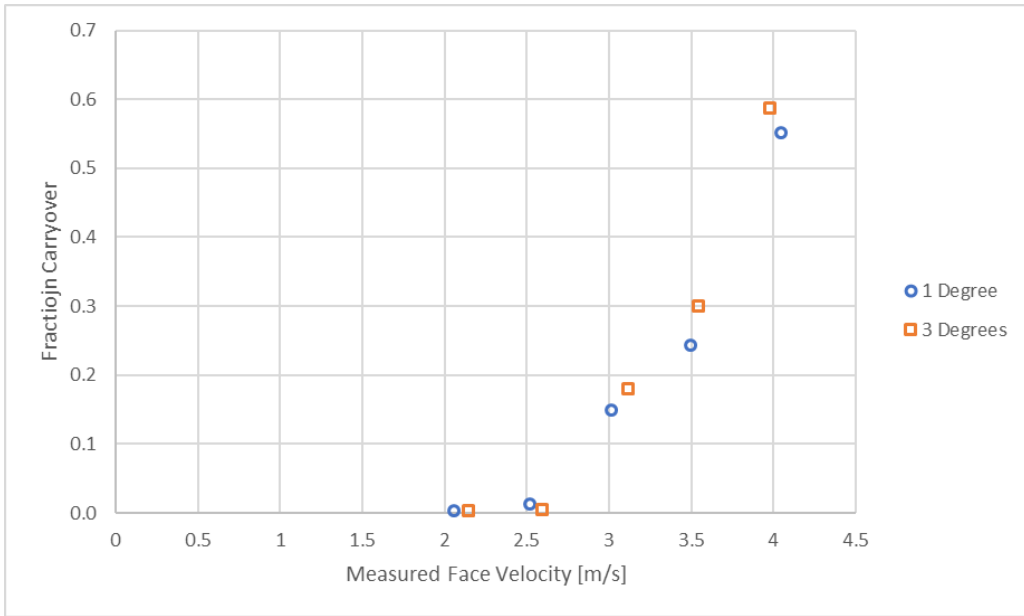


Figure 34: Result differences in terms of the dry velocity measured

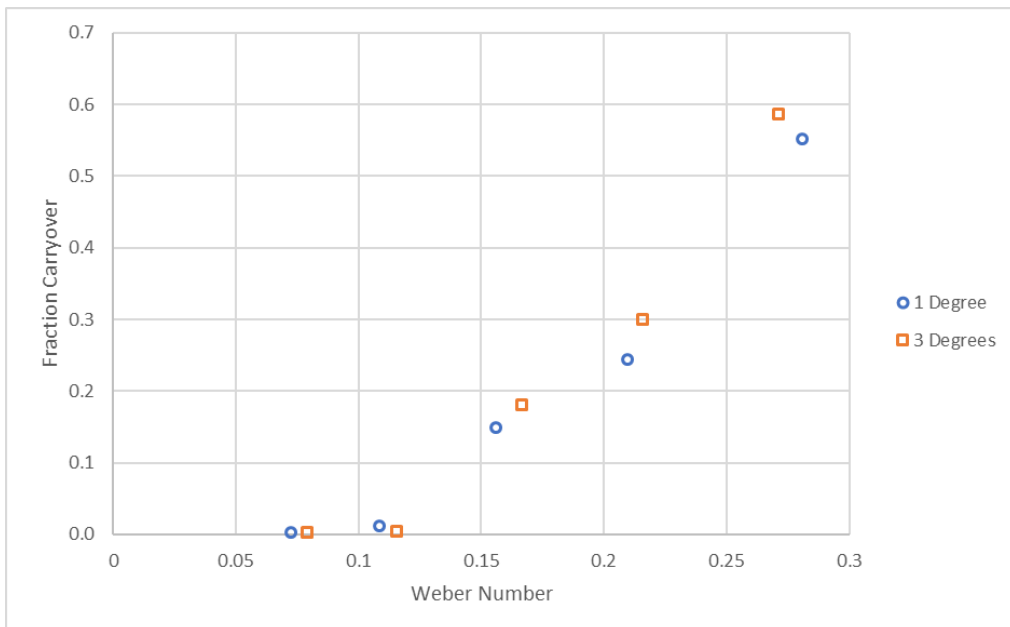


Figure 35: Result differences in terms of the Weber number

The results show that generally there is a slight difference shown between the two test angles. There is an increase in the FC as θ_{CAC} is increased, which is expected. However, the differences when comparing the 1° to 3° inclination results are relatively small. Since the uncertainty of the inclination angle is $\pm 0.5^\circ$, there should be no measurable impact on the results stemming from this uncertainty.

7.2 Comparison of 0-Degree Results with Reference Data

The entrainment testing performed by Min and Webb [18] is the only comparable reference data for this project and it was performed with the heat exchanger set with no angle of inclination. Therefore, the initial set of testing that was performed for this project was with the CAC set at an angle of 0°. Meaning that the tubes were parallel with the floor, while the inlet/outlet faces are perpendicular to it. This way, the results could be compared to the reference data to determine if they follow the same trend. The results for the 0° testing and the data taken from the reference are plotted in Figure 36.

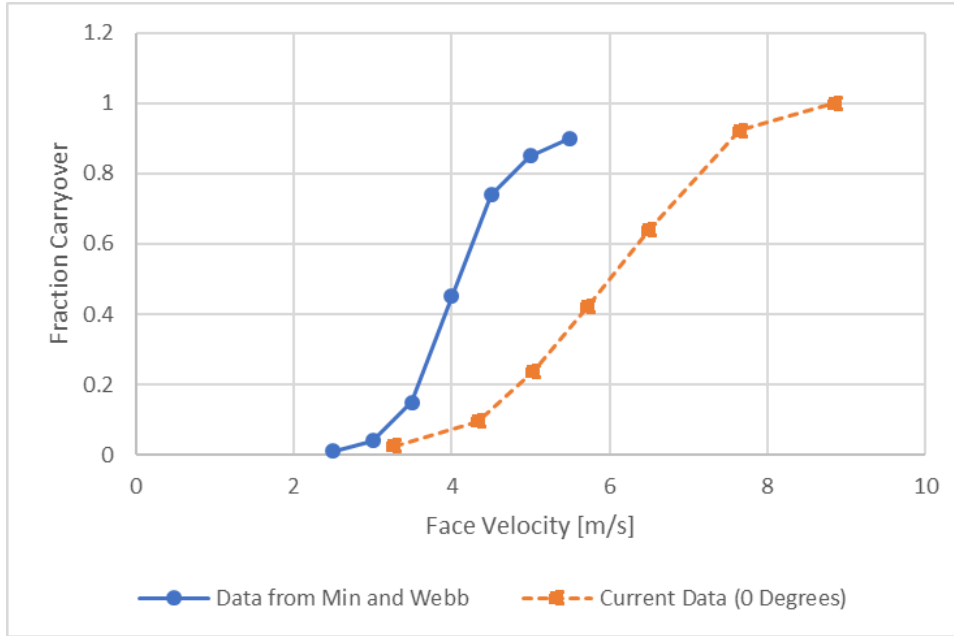


Figure 36: Comparison of results from 0° testing in terms of face velocity

It is interesting to note that the fraction carryover results obtained do follow a similar trend to the results obtained by Min and Webb [18] when plotted in terms of the HX face velocity. However, the curves that they form are not identical. This is expected since several parameters were not the same during the two experiments, such as the type of heat exchanger, the fin spacing/geometry and air/water parameters. To account for this, in Figure 37 both data sets were expressed in terms of the Weber number. In doing so, the curves become much more similar in shape and magnitude despite the differences present during the individual experiments. This is significant, as it implies that using the Weber number and the fin spacing as the significant length is an adequate way of expressing the fraction carryover of a heat exchanger as it normalizes the data by including the relevant governing parameters. This implies that it might be applicable for entrainment testing on any HX.

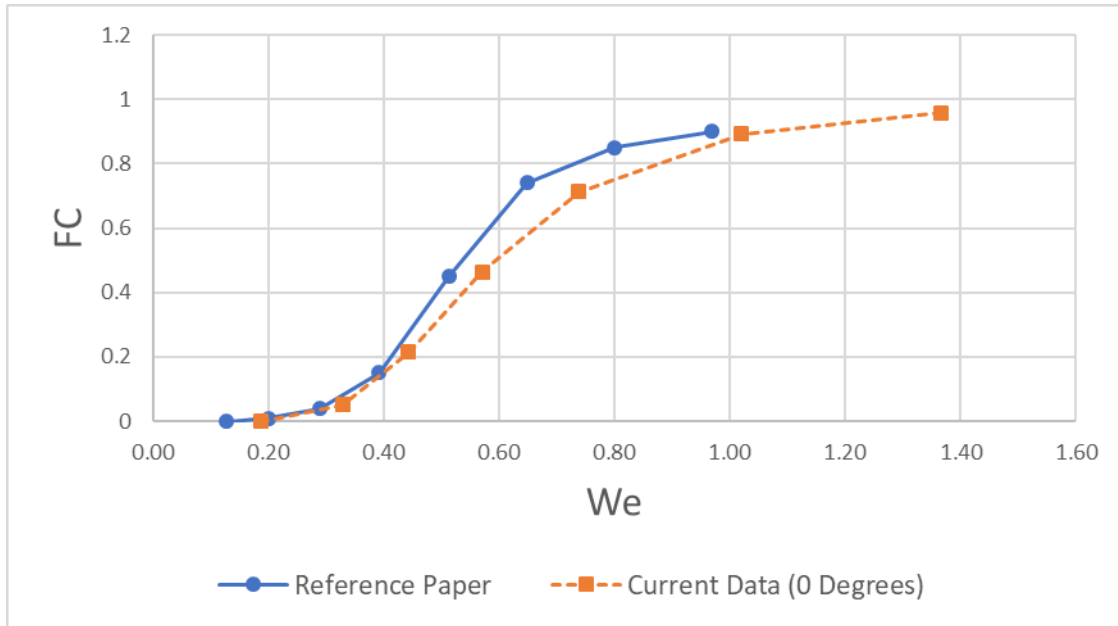


Figure 37: Comparison of results from 0° testing in terms of Weber number

7.3 CAC Entrainment Testing

The following results were gathered using the spray stand. Air mixed with water from the nozzle was passed through the CAC until it was saturated to simulate steady state condensation. *FC* was recorded for the same face velocities at multiple angles. The results are shown for each angle in terms of V_{face} in Figure 38 and in terms of *We* in Figure 39.

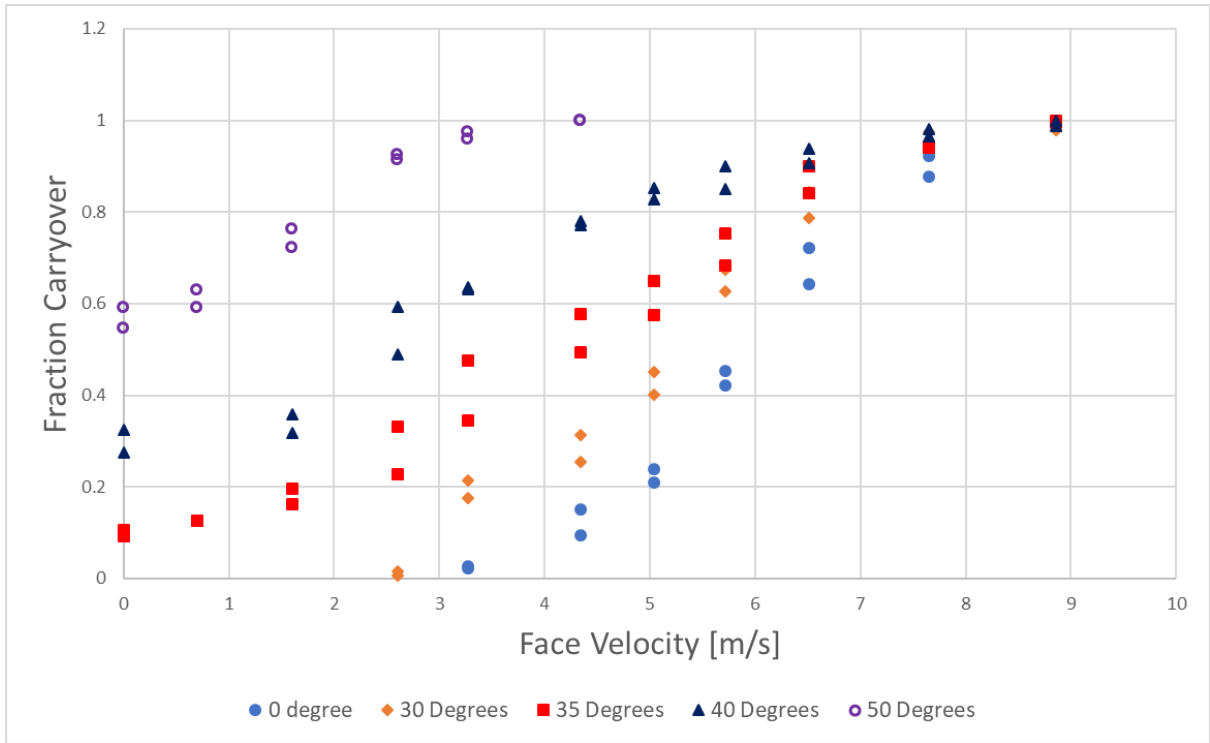


Figure 38: Fraction carryover in terms of face velocity

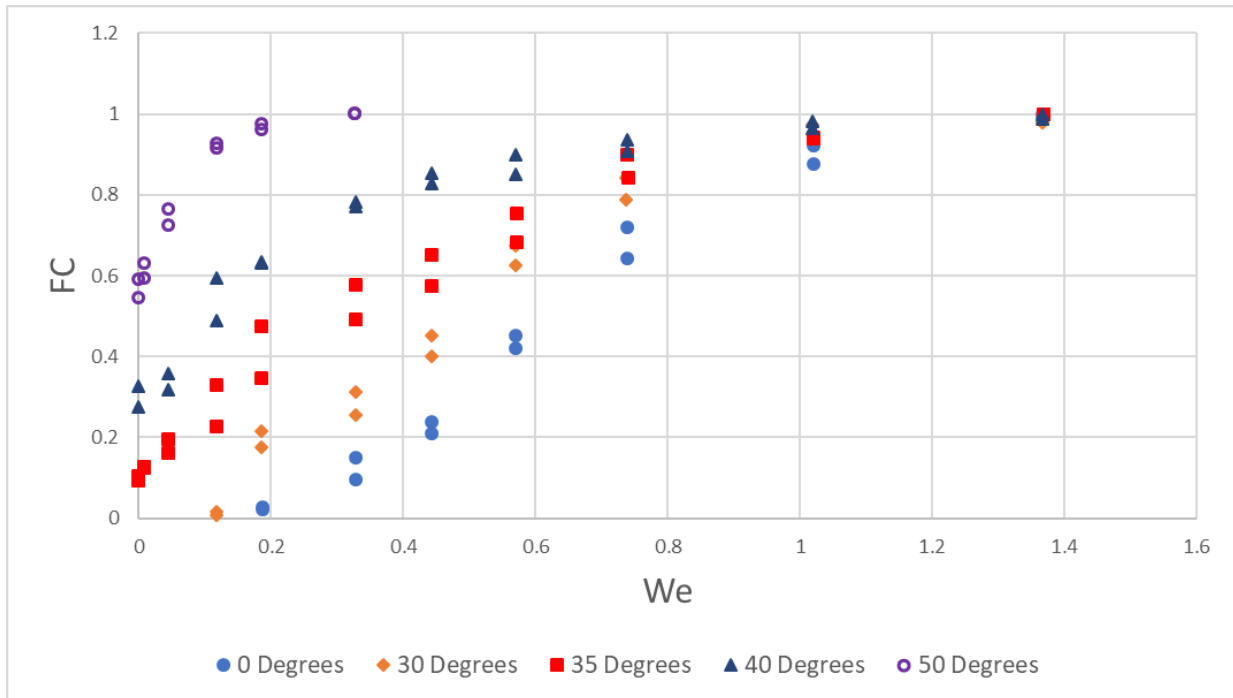


Figure 39: Fraction carryover in terms of Weber number

7.3.1 Effect of the Weber Number

Recall that the fraction carryover is the ratio of the condensate that exits the CAC in the form of entrained (blown through) condensate compared to the total amount of condensate leaving the CAC. Observing the data for each angle individually, it is evident that increasing We , which is predominantly dominated by the V_{face} , increases FC , meaning that a higher ratio of condensate is entrained. The increase in carryover appears to follow a third order distribution, increasing sharply once entrainment starts and then tends to 1 at higher velocities meaning that all the condensate that leaves the CAC is entrained while none of it drains off the faces.

7.3.2 Effect of CAC Angle

It is very interesting to note that for the angles tested, the FC follows a similar third order trend. It appears that increasing θ_{CAC} simply shifts the data set towards the left. This holds true up to an angle of roughly 40° . This means that increasing θ_{CAC} decreases the We_{crit} . It also reduces the V_{face} required for FC to equal 1.

7.3.2.A Critical Angles

The data demonstrates two critical angles where significant changes occur in the data. The first is at roughly 35° , where after this point, $FC > 0$ at $V_{face} = 0$, meaning that there is always some amount of condensate, FC_0 , that is entrained regardless of the value of V_{face} . The value of FC_0 increases almost linearly as the angle is increased after 35° , as seen in Figure 40. This occurs because the gravitational force acting on some of the droplets hanging at the end of the channels at these higher angles is large enough to cause the droplets to drop off the face without clinging to the face of the CAC and draining

to the bottom of the face. The gravitational force gets larger as θ_{CAC} is increased meaning that eventually even droplets with a smaller mass will drop without draining down the face. At $\theta_{CAC} > 35^\circ$, there is no longer a We_{crit} where entrainment begins. Rather, We_{crit} takes on a negative value. This is obviously not physically possible, but it serves to make the entire data set comparable for the sake of analysis.

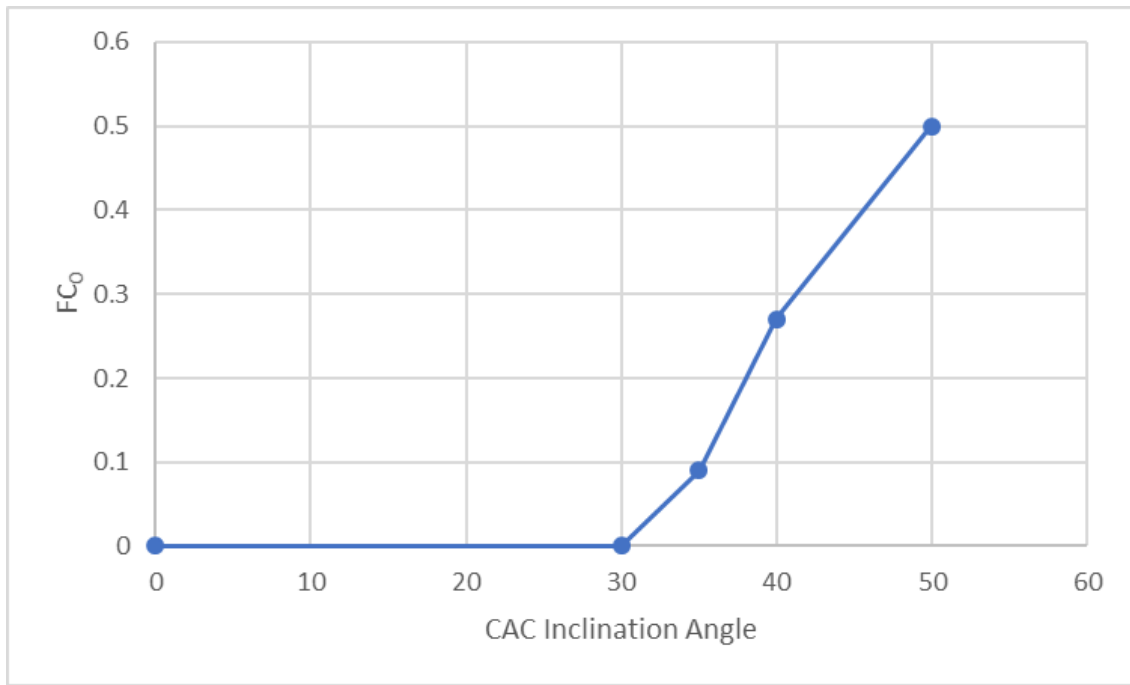


Figure 40: Increase in FC_0 with increasing inclination angle

The second critical angle lies somewhere between 40° and 50° . Here, the FC no longer follows the same trend as with the smaller angles, this is more clearly illustrated in Figure 41. At this point, the amount of condensate that is carried over may be dominated by other parameters, such as gravity, and the correlation of the FC using the We is no longer valid. Therefore, it could not be described using the same equation. This is likely due to this angle being very close to a critical point where there would be no “drained”

condensate even when $V_{face} = 0$ ($FC_0 = 1$). This is because the condensate that “drains” is now considered carried over since it drains above the angled plate. This is illustrated in Figure 42. At 50° there is still a minimal amount of condensate that runs along the HX face and drains through the gap in the inclined plate when $V_{face} = 0$ but it rapidly disappears once the air velocity is increased. No tests above 50° were performed. Therefore, it is not certain at exactly what angle there is no condensate that is considered drained when there is no air flow but it is likely not much higher than 50° .

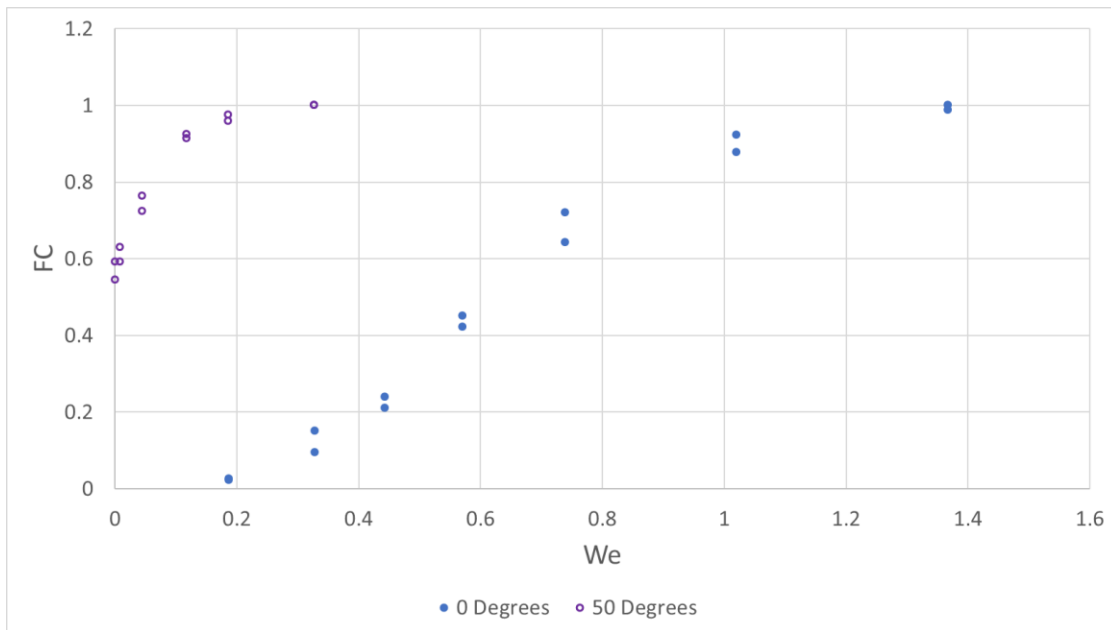


Figure 41: Change in trend at 50° CAC Inclination

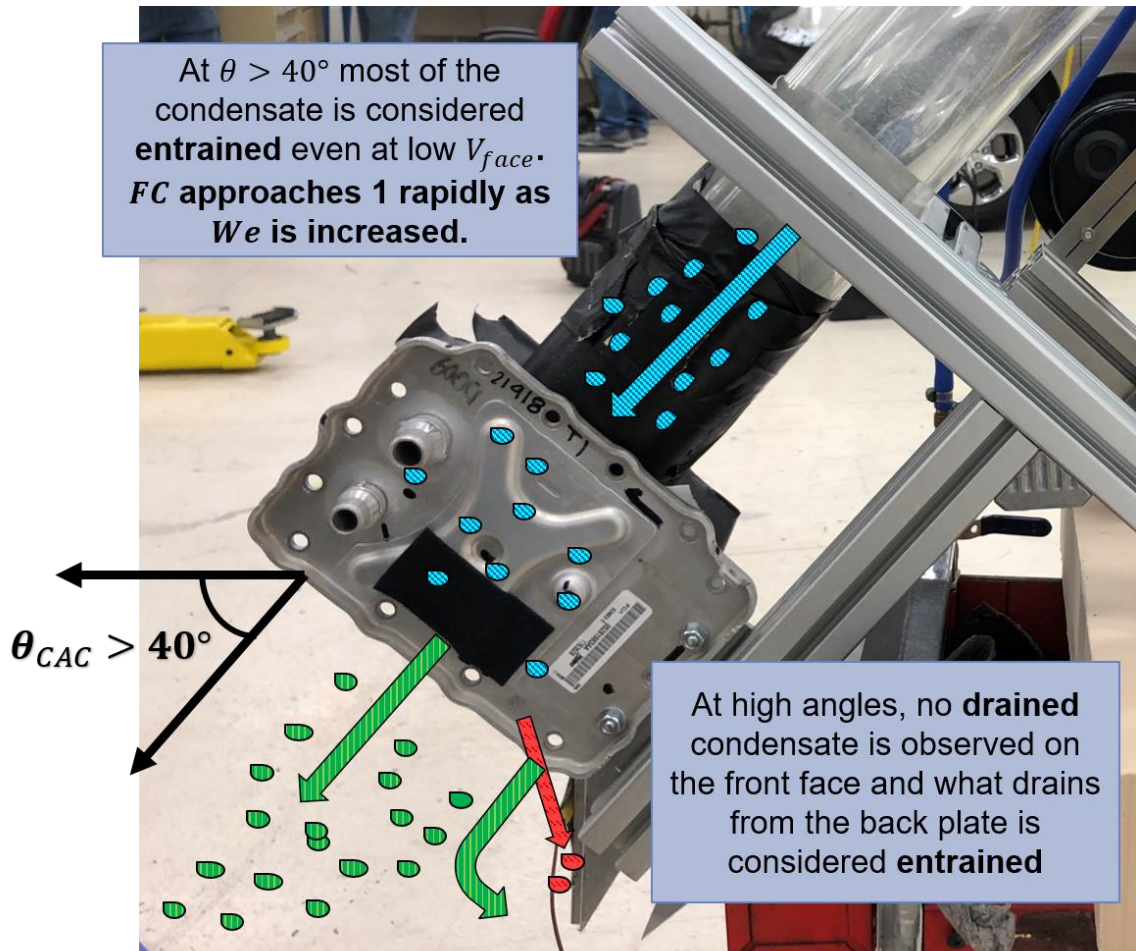


Figure 42: Representation of observed condensate at $\theta_{CAC} > 40^\circ$

7.4 Curve Fitting

The next step is to fit a predictive equation that can describe the FC . The goal is to create a predictive equation that uses only We and the θ_{CAC} as inputs. This way, the user could theoretically predict the amount of expected condensate for a range of θ_{CAC} under varying engine loads within some degree of certainty. To accomplish this, the method described in Chapter 5 is employed.

By plotting the data illustrated in Figure 39 in terms of the $We - We_{crit}$ for each respective angle, the data can be shifted so that it all starts from the origin. In the case of

$\theta_{CAC} > 35^\circ$, where there is always some form of *FC*, the $We_{crit} = 0$. To compensate for this, it is assumed that the curve continues to follow the same third order trend below zero and so a negative We_{crit} is used. The We_{crit} that was determined for each CAC angle tested is tabulated in Table 7.

Table 7: Critical Weber number for each measured angle

HX Angle [Degrees]	We_{crit}
0	0.17
30	0.1
35	-0.1
40	-0.2
50	-0.6

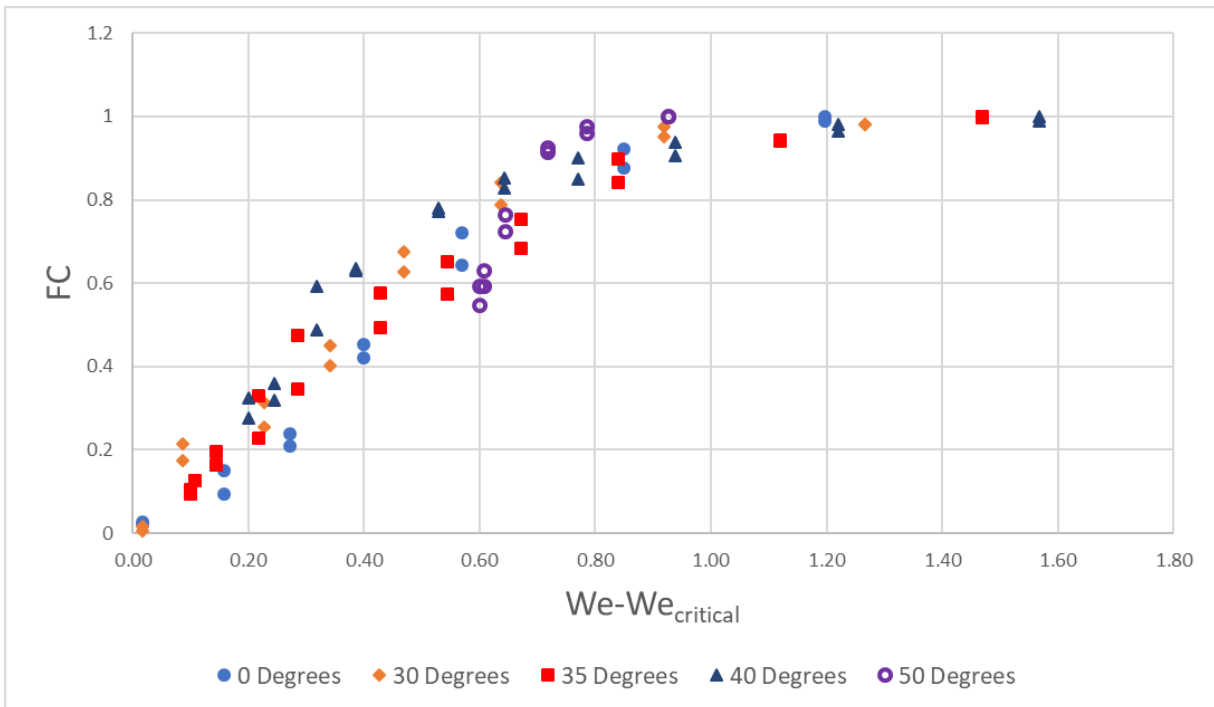


Figure 43: Fraction carryover plotted in terms of the We minus the We_{crit}

As seen in Figure 43, plotting the data this way illustrates that most of the data follows the same trend when normalized using We_{crit} .

The data from [18] could be described using equation 28 from Chapter 5, we now try using the same equation to describe the fraction carryover data. Recall that the general equation had the form:

$$FC = \frac{a[We - We_{crit}]^b}{\{1 + [a(We - We_{crit})^b]^n\}^{1/n}}$$

Where a , b and n must be optimized to best fit the data.

The data set for each angle has its own optimized curve with different coefficients. The coefficients and the root mean squared error (RMSE) are tabulated in Table 8 and they are illustrated in the following figures. The RMSE was calculated using the method provided by Chai and Draxler [54]

$$RMSE = \left[\sum_{i=1}^N \left(\frac{e_i^2}{N} \right) \right] \quad (65)$$

Where, e_i is the difference between the experimentally obtained value and the value obtained by the equation and N is the sample size.

Table 8: Optimized equation coefficients and resulting RMSE

θ_{CAC}	a	b	n	RMSE
0	13.5	3	1	0.12
30	30	3	0.83	0.20
35	151	3	0.5	0.24
40	76	3	0.68	0.11
50	2.7	3	7.8	0.05

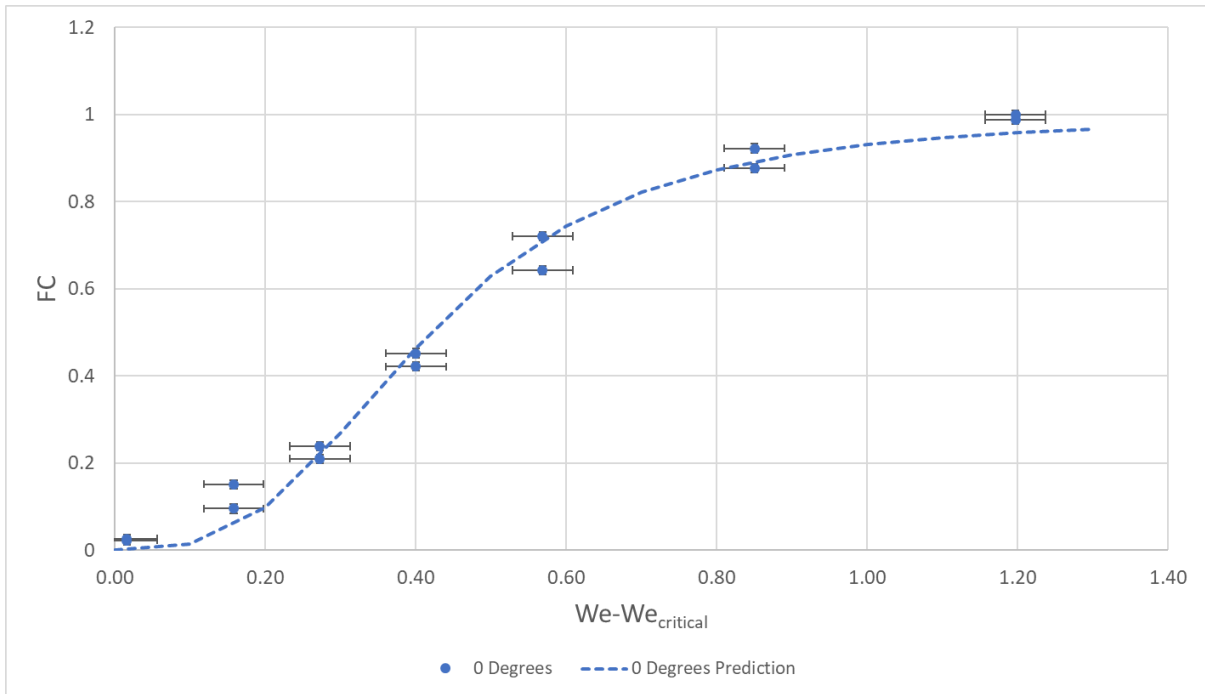


Figure 44: Predictive curve for 0° fraction carryover

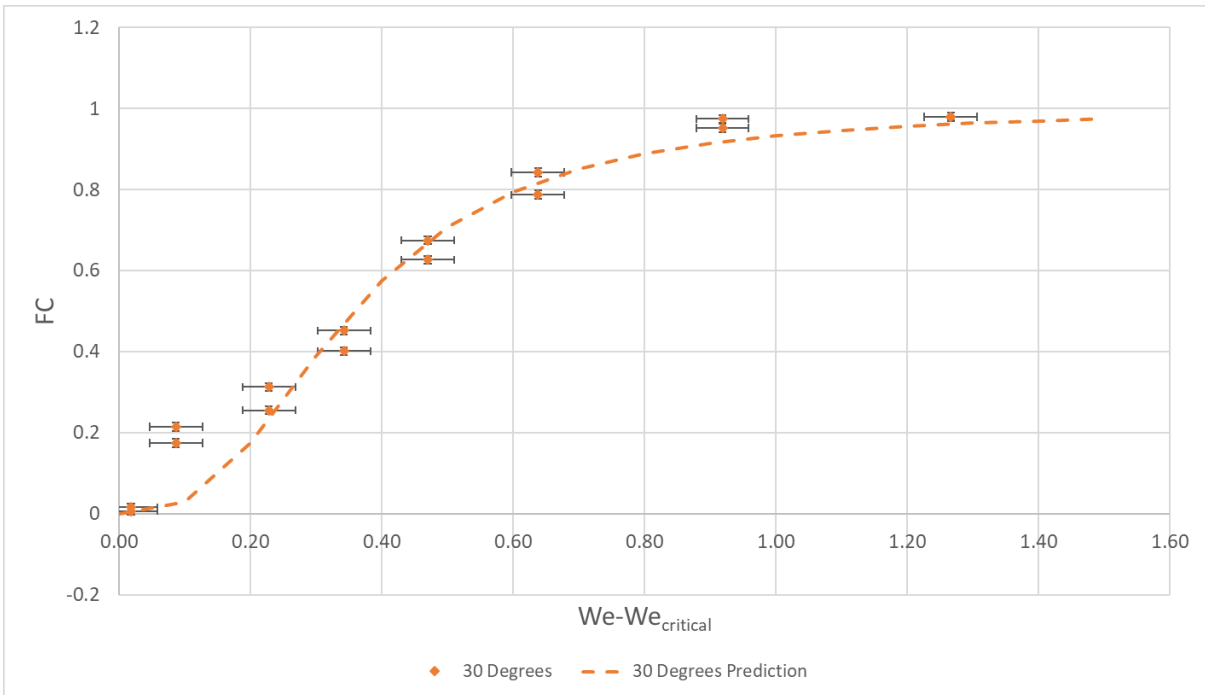


Figure 45: Predictive curve for 30° fraction carryover

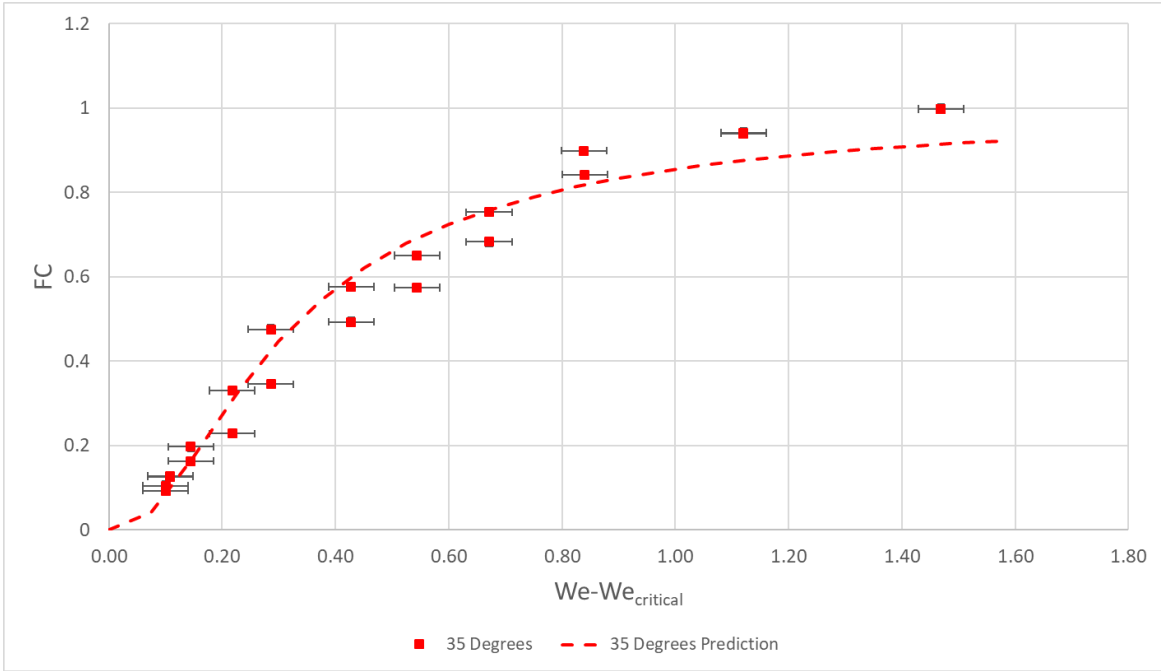


Figure 46: Predictive curve for 35° fraction carryover

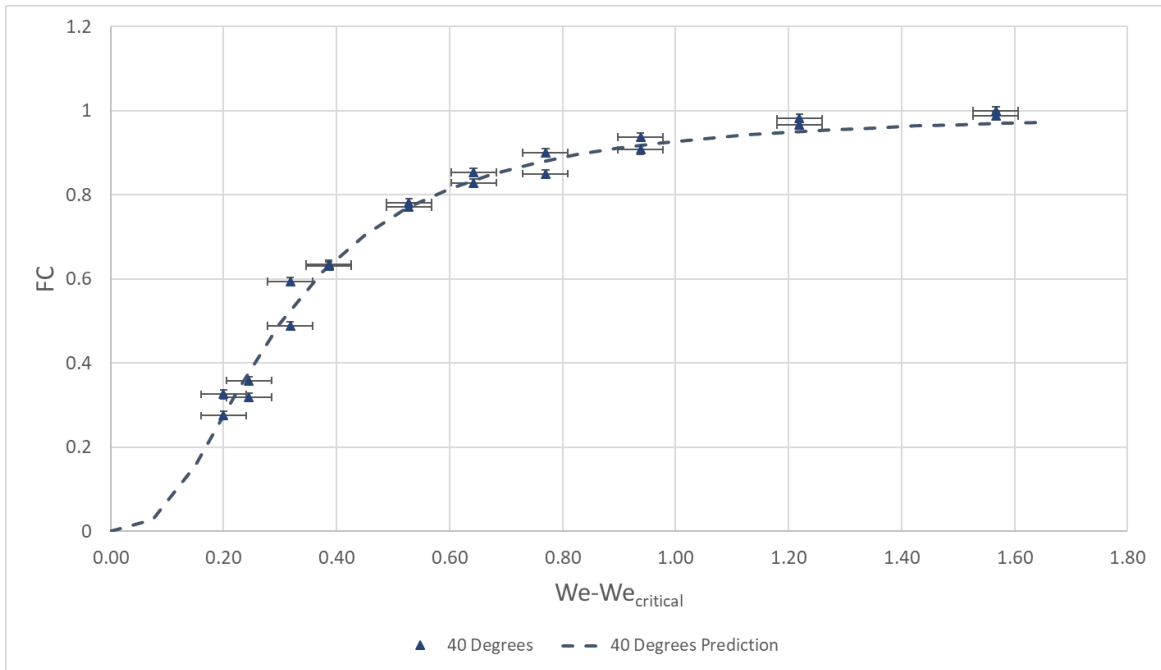


Figure 47: Predictive curve for 40° fraction carryover

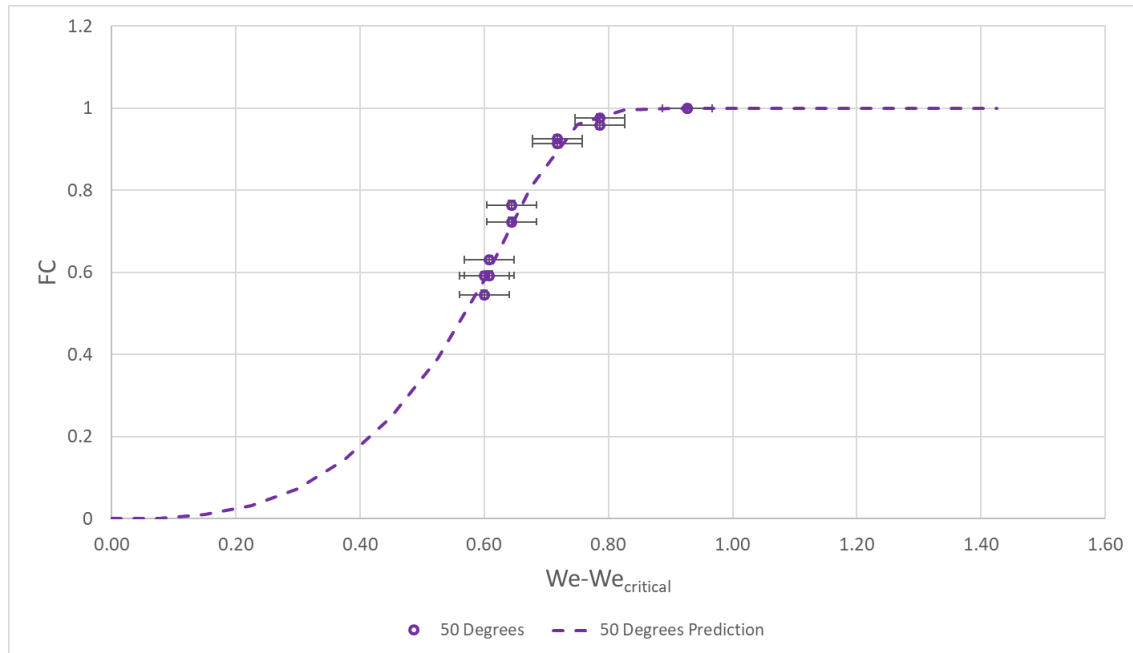


Figure 48: Predictive curve for 50° fraction carryover

As mentioned previously, the results do not follow the same distribution once an angle larger than 40° is reached. The quasi-linear increase of the carryover implies that it is likely near a critical point where all the water is entrained regardless of the We .

Next, a general equation can be fit to the entire data set. Although this equation will not describe each individual set as well as the one fit specifically to it, it fits the entirety of the data set most adequately. To determine the coefficients, the average was computed for a , b and n of each set, excluding the 50° results. Then the values were tweaked to optimize the fit and the result is illustrated in Figure 49.

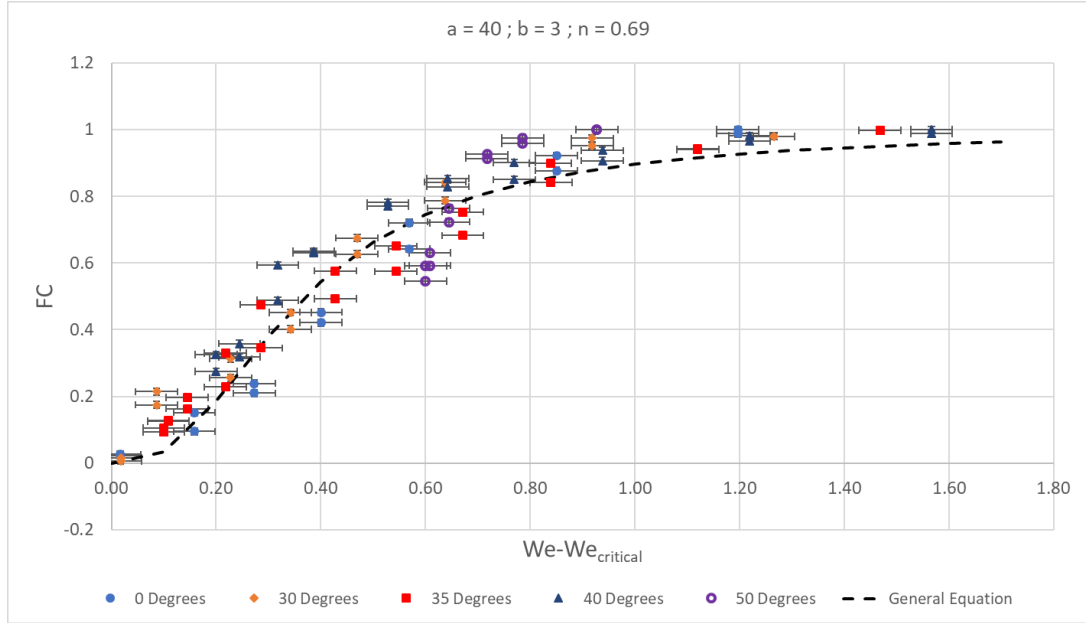


Figure 49: Optimized equation to best fit the entire data set

Therefore, a general equation that properly describes the fraction carryover for the CAC for $0^\circ \leq \theta \leq 40^\circ$ can be expressed as:

$$FC = \frac{40[We - We_{crit}]^3}{\{1 + [40(We - We_{crit})^3]^{0.69}\}^{1/0.69}} \quad (66)$$

The We_{crit} depends on θ_{CAC} and for the values that were tested, they are listed in Table 7. The We_{crit} in terms of the CAC angle is illustrated in Figure 50 using the five angles that were tested. However, there are not enough points to illustrate a strong trend. Additional testing needs to be performed to determine the We_{crit} at more angles between the ones tested to properly correlate the two. Then the We_{crit} could be included in equation 66 as a function of the CAC angle.

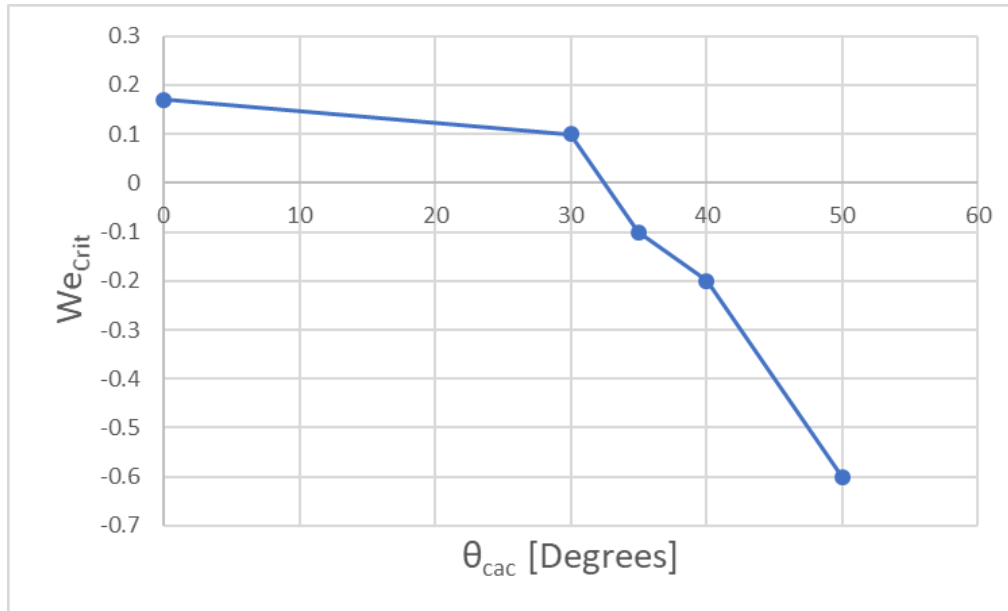


Figure 50: We_{crit} in terms of the Inclination Angle

7.5 Liquid Bridge Testing Results

The tested velocities, along with the observations made are listed in Table 9.

Table 9: Liquid bridge testing observations

Air Velocity [m/s]	Observations	Inlet Width [mm]
3.4	<ul style="list-style-type: none"> Long slow sliding before breaking into 2. Left a droplet in its trail that was blown out. 	400
5.03	<ul style="list-style-type: none"> Pushed further along plate before breaking up. Droplets they form are eventually blown out. 	400
6.67	<ul style="list-style-type: none"> Bridge is broken into multiple smaller droplets that coalesce forming a sort of liquid film. With the more concentrated airflow the bridge appears to take longer to breakup. 	200
9.30	<ul style="list-style-type: none"> Almost instant breakup. Small satellite droplet formed upon breakup which is immediately blown through. The remainder breaks up as a film and continues to move along the lower surface. 	200
Gradually Increased	<ul style="list-style-type: none"> At first the bridge doesn't move. Eventually starts moving very slowly. Once a critical velocity is reached it breaks apart and spreads as a film-like droplet on the lower plate. 	200

Figure 51 illustrates the way the liquid bridge is stretched before breakup up. In this test, the air velocity was set to 6.67 m/s and the liquid bridge broke up without forming a satellite droplet. Figure 52 shows a test at 9.30 m/s where the bridge broke up and formed a satellite droplet which was immediately entrained by the air. This breakup mode would likely contribute the most to the fraction carryover. Finally, Figure 53 shows a test where the air velocity was gradually increased. At the low velocity, the bridge was moved along the plates and remained intact. Had the velocity not changed, the bridge would have made its way to the end of the plates without breaking up.

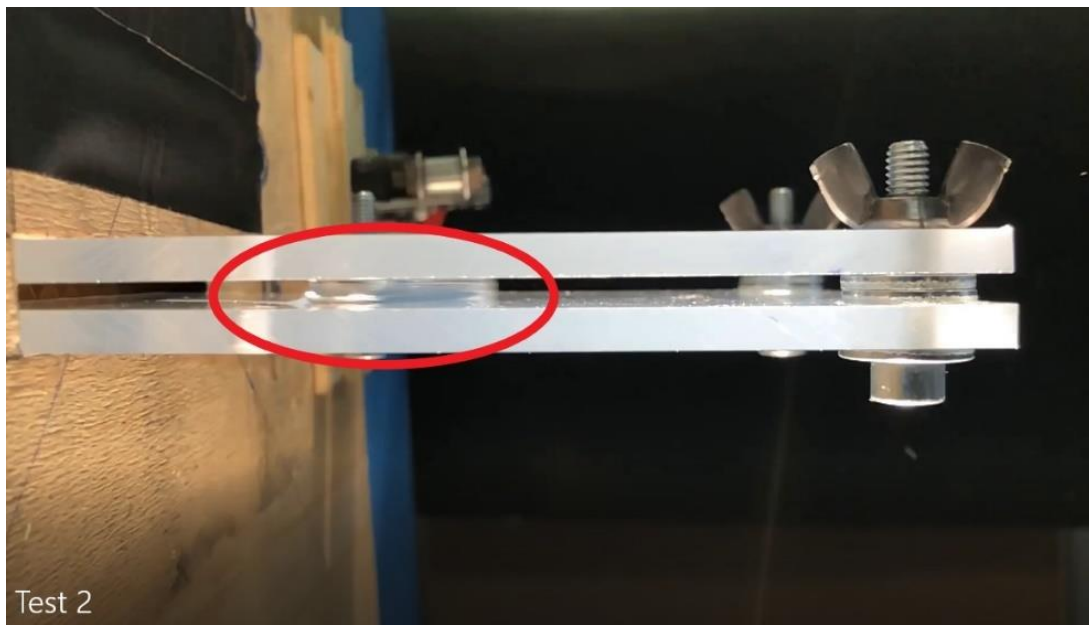


Figure 51: Liquid bridge stretched just before breakup

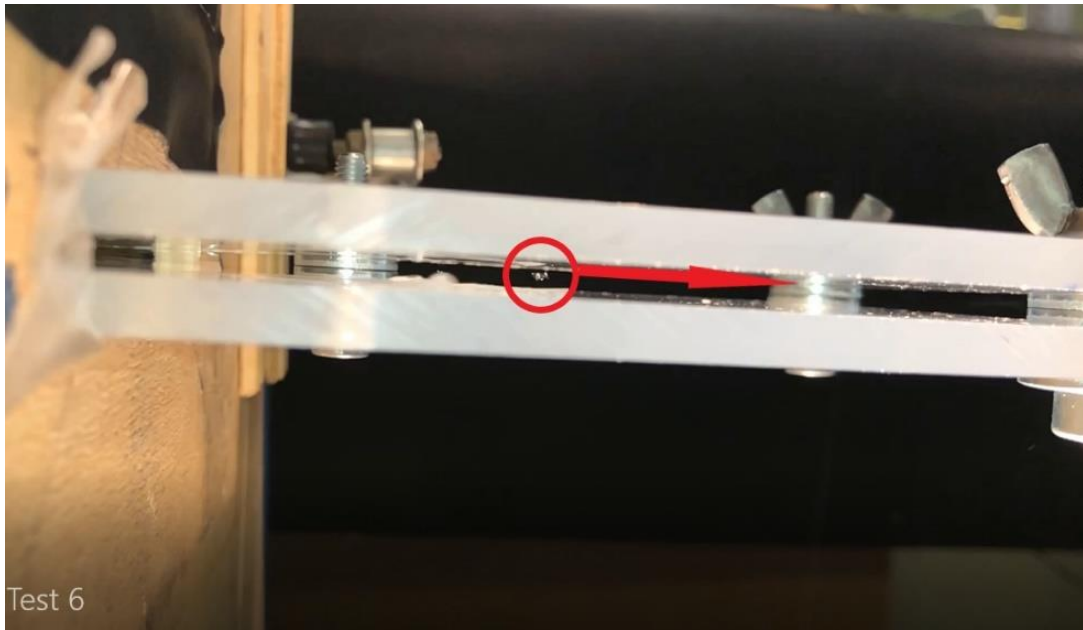


Figure 52: Satellite droplet formed immediately after breakup at 9.30 m/s

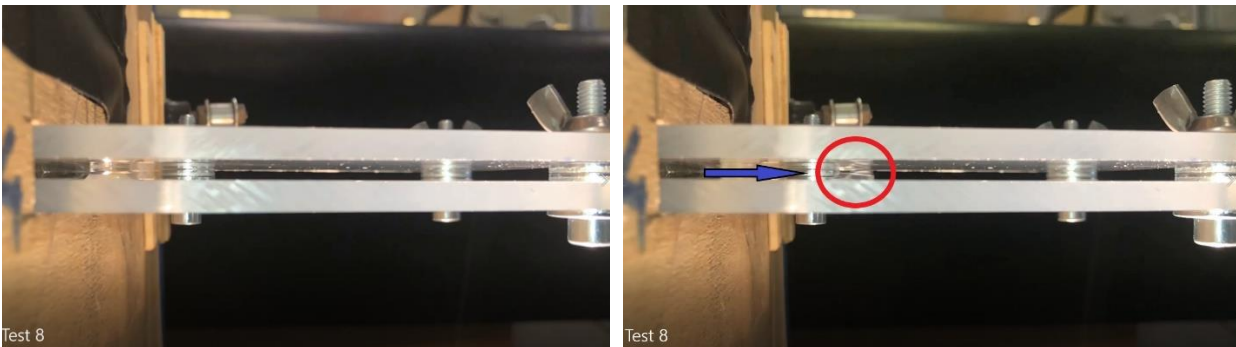


Figure 53: Bridge is pushed along intact at low velocities

Chapter 8 – Conclusions and Recommendations

8.1 CAC Condensate Entrainment Characteristics

Prior to these experiments, very little information could be found in open literature pertaining to the measurement of the fraction carryover of the condensate produced in a heat exchanger. There is no standardized method yet established for quantifying the entrainment in a generalized way for all heat exchangers. Comparing the results obtained with the ones obtained in the reference literature where similar experimentation was performed and plotting them in terms of the Weber number with the fin pitch as a significant length showed that this is an adequate way of expressing the fraction carryover.

Plotting the FC in terms of the We yielded a trend that could be expressed as a third order function. For $0^\circ \leq \theta_{CAC} < 35^\circ$, there exists a We_{crit} larger than 0 that must be reached before entrainment begins. For $\theta_{CAC} \geq 35^\circ$, the We_{crit} exists below 0, meaning that there is always some form of fraction carryover, FC_0 , even when $We = 0$. As the CAC angle is increased, the trend remains almost identical, however, it is shifted to the left along the x -axis. This holds true for $\theta_{CAC} \leq 40^\circ$ at which point, somewhere between 40° and 50° , the trend changes shape. This is likely due to being very close to the point where $FC_0 = 1$ and the phenomena governing the amount of condensate that is carried over may be dominated by another parameter. This means that for any angles larger than 40° , this correlation using the We is not valid and it should not be used to predict the FC .

For $0^\circ \leq \theta_{CAC} \leq 40^\circ$, the fraction carryover for this CAC can be well estimated using only the We and We_{crit} as inputs. The We_{crit} depends on the θ_{CAC} and for the tested

angles, this value is known. Otherwise, it may be estimated through interpolation using the trend formed by the data points. However, the accuracy of estimating the We_{crit} based on the trend has not been tested experimentally. Furthermore, the We_{crit} should be determined for more angles to validate the trend before this method is employed.

8.2 Liquid Bridge Testing Conclusions

It is clear that the experimental set-up used to perform these tests does not accurately replicate what is happening within the CAC channels. To do that, the test piece would need to be built in a way that simulates louvers and the spacing between the plates must be much smaller. Even then, plexiglass has a different wettability than that of aluminum, so the surface tension forces are not comparable. Due to the limitations of the available camera and time available, this was the closest approximation possible. However, several conclusions can still be drawn from on the testing performed. Based on the observations, when a liquid bridge is exposed to a shearing air flow there are four main modes through which it may react.

1. The surface tension forces between the liquid bridge and the plates are larger than the drag force and the bridge doesn't move. It therefore acts as a sort of "barrier" for the remaining droplets in the channel, contributing to the retained amount. This is likely to happen at very low We , where the velocity of the air is quite low through the channels.
2. The drag force is high enough to push the bridge along the channel without it breaking up, gathering other droplets in its path. It then slides off the end, contributing to the drained condensate. This is more likely to happen at low We

but where the air velocity is still high enough to form a drag force that overwhelms the surface tension retention forces.

3. The air velocity is high enough so that the drag force overwhelms the surface tension forces on the upper plate, so the bridge simply collapses and adds to the liquid film without creating a satellite droplet. This occurs at higher We .
4. The bridge breaks up due to the airflow and a small satellite droplet is formed which is immediately entrained, adding to the entrained amount. The drops that stay behind add to the retained amount. This is likely to happen at even larger We .

Based on this information, it is possible that there is some critical value air flow speed for any environment containing liquid bridges where a satellite droplet gets formed. At this point, the amount of condensate that is entrained might increase dramatically. This would need to be considered in the creating of a numerical model.

8.3 Recommendations for future Experimental Studies

8.3.1 Additional Entrainment Testing

Since the correlation accounts for the inclination angle by use of the We_{crit} , further testing should be performed using the same test bench to identify the We_{crit} for a larger set of angles for up to 40°. That way, a trend could be well identified, and an equation could be made to fit the data. This correlation could then be used to more accurately predict the We_{crit} for any angle up to 40° meaning that the inclination angle could be easily used as an input parameter.

In order to further validate and develop a correlation between the fraction carryover and the engine load, there are several other parameters that should also be investigated, such as different CAC fin spacings and geometries. The scope of this project focused only on one specific CAC and therefore these parameters were not changed throughout the testing. Although comparing the results obtained with those from literature showed that using the We with the fin spacing as the significant length seems to normalize the results adequately, it would be beneficial to investigate how different heat exchanger geometries affect the drainage vs entrainment characteristics. This could help influence future CAC design to help prioritize drainage over entrainment. Furthermore, all the tests in this study had the CAC plates running in the vertical direction. Similar testing should be performed with the CAC plates running horizontally. This would likely influence the behavior of the condensate. Other parameters that could be investigated are those that affect the wettability of the CAC fins, such as wear and age. Throughout its lifetime, a CAC will accumulate dirt, oil and other debris from the gasses passing through. This debris and any wear that this causes to the metal will change the wettability of the surfaces and, in-time, likely change the CAC's tendency to retain condensate.

The test procedure could also be improved by applying more advanced sampling techniques, such as isokinetic sampling. This would ensure that a more consistent amount of condensate is captured during the collection process. The use of isokinetic sampling is discussed in more detail in Appendix B.

8.3.2 Testing at Angles Above 40°

The correlation of the FC to the We only proved to be valid for angles up to 40°. At higher angles there are other parameters that start to govern the FC and the data starts

to follow a different trend. Therefore, testing at higher angles could be performed and a correlation could be attempted with other dimensionless groups that consider other parameters, such as the Bond number. If an equation that combines the two correlations can be formed, it would increase its bounds and allow for the prediction of the *FC* for a larger range of angles.

8.3.3 CAC Condensate Retention Testing

This project focused on the fraction of condensate that is entrained compared to the drained condensate. It was assumed for all tests that the CAC was at steady state and was fully saturated, meaning that the condensate retained within the fins was at a constant value, hence as soon as any amount of condensate left the CAC it was immediately replaced with new condensate. Heat exchanger condensate retention studies are available in literature but have never been performed on CACs. It was determined that the amount of condensate that a heat exchanger can retain depends mainly on its geometry. Future studies should investigate the effect of a transience in the operating parameters. If the CAC is allowed to accumulate a high amount of condensate at a low face velocity and suddenly the face velocity is increased dramatically, the total amount of condensate that the CAC will retain likely drops, meaning that a large amount of condensate will be ejected at once leading to a very high amount of carryover for a brief period of time. The amount that is ejected will likely depend on the magnitude of the difference in face velocity and on the CAC's geometry/fin spacing.

8.3.4 Measurement of Droplet Size Distribution

Other experiments that could be beneficial to the field is the measurement of the size distribution of the droplets being ejected from the CAC. This could be accomplished by having the stream hit a plate coated with a hydrophilic substance. Then, using a microscope, the drops of different sizes are counted. The results from these kinds of experiments would help determine how water droplets move downstream of the CAC and what percentage could be entrained far enough to enter the engine instead of hitting the intake manifold.

8.3.5 Liquid Bridge Testing

The purpose of the observational liquid bridge testing performed throughout this project was to identify the main modes that a liquid bridge can react when exposed to a perpendicular airflow. However, there are many ways that this could be expanded upon.

The test bench that was fabricated to perform this testing was simple and was not intended to simulate the internals of a CAC. Further testing should be performed using a test bench that accurately simulates the internal structure of a CAC to gain a better understanding of which of the identified breakup modes are most prevalent within the channels. Then, this could be correlated with the face velocity and inclination angle of the heat exchanger. This information would be useful if a robust numerical model describing the internal condensate were to eventually be developed.

REFERENCES

- [1] R. Cash, "A Quantitative Investigation Of The Water Condensation Inside Tubes Of Compact Charge Air," 2015.
- [2] W. Mingrui, N. Thanh Sa, R. F. Turkson, L. Jinping, and G. Guanlun, "Water injection for higher engine performance and lower emissions," *J. Energy Inst.*, vol. 90, no. 2, pp. 285–299, 2017.
- [3] S. Emtec, "EGR - Exhaust Gas Recirculation." [Online]. Available: <http://www.sttemtec.se/sv/egr/egr.php>.
- [4] T. C. Scott, "AUTOMOTIVE THERMO / FLUIDS Fundamentals of Moist Air Properties and Processes (6 / 25 / 12)."
- [5] A. I. ElSherbini and A. M. Jacobi, "A Model for Condensate Retention on Plain-Fin Heat Exchangers," *J. Heat Transfer*, vol. 128, no. 5, p. 427, 2006.
- [6] K. Wang, B. Bai, and W. Ma, "A model for droplet entrainment in churn flow," *Chem. Eng. Sci.*, vol. 104, pp. 1045–1055, 2013.
- [7] B. H. Kim and G. P. Peterson, "Analysis of the critical Weber number at the onset of liquid entrainment in capillary-driven heat pipes," *Int. J. Heat Mass Transf.*, vol. 38, no. 8, pp. 1427–1442, 1995.
- [8] K. F. Eid, M. Panth, and A. D. Sommers, "The physics of water droplets on surfaces: Exploring the effects of roughness and surface chemistry," *Eur. J. Phys.*, vol. 39, no. 2, p. 25804, 2018.

- [9] X. Wang and L. Wang, "Dynamic Contact Angle on a Surface with Gradient in Wettability," 2016.
- [10] T. C. Ku, J. H. Ramsey, and W. C. Clinton, "Calculation of Liquid Droplet Profiles from Closed-Form Solution of Young-Laplace Equation," *IBM J. Res. Dev.*, vol. 12, no. 6, pp. 441–447, 1968.
- [11] A. D. Sommers, J. Ying, and K. F. Eid, "Predicting the onset of condensate droplet departure from a vertical surface due to air flow-Applications to topographically-modified, micro-grooved surfaces," *Exp. Therm. Fluid Sci.*, vol. 40, pp. 38–49, 2012.
- [12] A. I. ElSherbini and A. M. Jacobi, "Liquid drops on vertical and inclined surfaces: I. An experimental study of drop geometry," *J. Colloid Interface Sci.*, vol. 273, no. 2, pp. 556–565, 2004.
- [13] S. A. Krzeczowski, "Measurement of liquid droplet disintegration mechanisms," *International Journal of Multiphase Flow*, vol. 6, no. 3, pp. 227–239, 1980.
- [14] M. A. Verges, M. C. Larson, and R. Bacou, "Force and shapes of liquid bridges between circular pads," *Exp. Mech.*, vol. 41, no. 4, pp. 351–357, 2001.
- [15] M. Ishii and M. A. Grolmes, "Inception Criteria for Droplet Entrainment In Two-Phase Concurrent Film Flow," vol. 21, no. 2, 1975.
- [16] M. Lawson, "Practical Applications of Delta Winglets in Compact Heat Exchangers with Practical Applications of Delta Winglets in Compact Heat Exchangers with Louvered Fins," Virginia Polytechnic Institute and State University, 2015.
- [17] A. V. Cherdantsev, "Overview of physical models of liquid entrainment in annular

- gas-liquid flow,” *AIP Conf. Proc.*, vol. 1939, no. March, 2018.
- [18] J. Min and R. L. Webb, “Condensate carryover phenomena in dehumidifying, finned-tube heat exchangers,” *Exp. Therm. Fluid Sci.*, vol. 22, no. 3–4, pp. 175–182, 2000.
- [19] S. B. Riffat, C. F. Afonso, A. C. Oliveirat, and D. A. Reay, “NATURAL AIR-CONDITIONING SYSTEMS,” vol. 17, no. 1, 1997.
- [20] ASHRAE, *2018 Ashrae Handbook*, 2018th ed. Tullie Circle, 2018.
- [21] T. C. Scott, “personal communication.” 2019.
- [22] J. M. Kaiser and A. M. Jacobi, “Condensate Retention Effects on the Air-Side Heat Transfer Performance of Automotive Evaporator Coils Amana Refrigeration , Inc . Carrier Corporation Copeland Corporation DaimlerChrysler Corporation Delphi Harrison Thermal Systems Frigidaire Company Gener,” 2000.
- [23] A. D. Sommers, R. Yu, N. C. Okamoto, and K. Upadhyayula, “Condensate drainage performance of a plain fin-and-tube heat exchanger constructed from anisotropic micro-grooved fins,” *Int. J. Refrig.*, vol. 35, no. 6, pp. 1766–1778, 2012.
- [24] L. T. Li *et al.*, “Investigation of defrosting water retention on the surface of evaporator impacting the performance of air source heat pump during periodic frosting-defrosting cycles,” *Appl. Energy*, vol. 135, pp. 98–107, 2014.
- [25] A. I. ElSherbini and A. M. Jacobi, “Retention forces and contact angles for critical liquid drops on non-horizontal surfaces,” *J. Colloid Interface Sci.*, vol. 299, no. 2, pp. 841–849, 2006.

- [26] S. Ravi Annapragada, J. Y. Murthy, and S. V. Garimella, "Droplet retention on an incline," *Int. J. Heat Mass Transf.*, vol. 55, no. 5–6, pp. 1457–1465, 2012.
- [27] A. Cioncolini and J. R. Thome, "Prediction of the entrained liquid fraction in vertical annular gas-liquid two-phase flow," *Int. J. Multiph. Flow*, vol. 36, no. 4, pp. 293–302, 2010.
- [28] B. Fulton and D. Styles, "Condensate Accumulation Model for an Engine Heat Exchanger," US 2014/0102428 A1, 2014.
- [29] E. Bettanini, "Simultaneous Heat and Mass Transfer on a Vertical Surface," *Int. Inst. Refrig. Bull.*, vol. 70, pp. 309–317, 1970.
- [30] F. c. McQuiston, "Correlation of Heat, Mass, and Momentum Transport Coefficients for Plate-Fin-Tube Heat Transfer Surfaces with Staggered Tubes," *ASHRAE Trans.*, vol. 84(1), pp. 294–308, 1978.
- [31] F. c. McQuiston, "Heat, Mass and Momentum Transfer Data for Five Plate-Fin-Tube Heat Transfer Surfaces," *ASHRAE Trans.*, vol. 84(1), pp. 266–293, 1978.
- [32] E. H. Uv and O. K. Sonju, "Heat Transfer Measurements of Circular Finned Tubes With and Without Partial Condensation," *Inst. Chem. Eng. Symp.*, vol. 1, no. 129, pp. 295–302, 1992.
- [33] C. M. Korte and A. M. Jacobi, "Condensate Retention and Shedding Effects on Air-Side Heat Exchanger Performance," vol. 61801, no. September, 1997.
- [34] Y. Zhong, A. Joardar, Z. Gu, Y. G. Park, and A. M. Jacobi, "Dynamic dip testing as a method to assess the condensate drainage behavior from the air-side surface of

- compact heat exchangers," *Exp. Therm. Fluid Sci.*, vol. 29, no. 8, pp. 957–970, 2005.
- [35] A. Joardar, Z. P. Gu, and A. M. Jacobi, "Assessing the Condensate-Drainage Behavior of Dehumidifying Heat Exchangers," *Int. Refrig. Air Cond. Conf.*, pp. 1–8, 2004.
- [36] G. D. Mandrusiak and V. P. Carey, "A method for detecting liquid shedding during annular flow in channels with offset strip," *Exp. Therm. Fluid Sci.*, vol. 4, pp. 239–245, 1991.
- [37] J. S. Brown, J. L. Terry, and R. J. Hutter, "An analytical prediction of water droplet travel when discharged from the face of an evaporator core," *SAE Pap.*, no. 940501, 1994.
- [38] K. T. Hong, "Fundamental characteristics of dehumidifying heat exchangers with and without wetting coatings," The Pennsylvania State University, 1996.
- [39] A. D. Sommers, "Methodology for calculating the volume of condensate droplets on topographically modified, microgrooved surfaces," *Langmuir*, vol. 27, no. 9, pp. 5523–5533, 2011.
- [40] L. Liu and A. M. Jacobi, "Issues affecting the reliability of dynamic dip testing as a method to assess the condensate drainage behavior from the air-side surface of dehumidifying heat exchangers," *Exp. Therm. Fluid Sci.*, vol. 32, no. 8, pp. 1512–1522, 2008.
- [41] M. Edalatpour, L. Liu, A. M. Jacobi, K. F. Eid, and A. D. Sommers, "Managing water

- on heat transfer surfaces: A critical review of techniques to modify surface wettability for applications with condensation or evaporation,” *Appl. Energy*, vol. 222, no. July, pp. 967–992, 2018.
- [42] C. Berna, A. Escrivá, J. L. Muñoz-Cobo, and L. E. Herranz, “Review of droplet entrainment in annular flow: Interfacial waves and onset of entrainment,” *Prog. Nucl. Energy*, vol. 74, pp. 14–43, 2014.
- [43] G. F. Hewitt and D. G. Owen, “EXPERIMENTAL DATA SET NO. 1: PRESSURE DROP AND ENTRAINMENT FRACTION IN FULLY DEVELOPED FLOW,” *Multiph. Sci. Technol.*, vol. 3, no. 1–4, pp. 145–154, 1987.
- [44] C. T. Crowe, *Multiphase Flow Handbook*, First. Boca Raton, 2005.
- [45] C. Extrand and Y. Kumagai, “Liquid Drops on an Inclined Plane: The Relation between Contact Angles, Drop Shape, and Retentive Force,” *J. Colloid Interface Sci.*, vol. 170, pp. 515–521, 1995.
- [46] B. J. Briscoe and K. P. Galvin, “The sliding of sessile and pendent droplets The critical condition,” *Colloids and Surfaces*, vol. 52, pp. 219–229, 1991.
- [47] E. B. Dussan, “ON THE SPREADING OF LIQUIDS ON SOLID SURFACES: STATIC AND DYNAMIC CONTACT LINES,” *Annu. Rev. Fluid Mech.*, vol. 11, pp. 371–400, 1979.
- [48] J. Fan, M. C. T. Wilson, and N. Kapur, “Displacement of liquid droplets on a surface by a shearing air flow,” *J. Colloid Interface Sci.*, vol. 356, no. 1, pp. 286–292, 2011.
- [49] A. S. Lexmond and C. W. M. Van Der Geld, “The effect of fluid flow on the

- detachment of drops in the wake of a flat plate,” vol. 29, pp. 363–370, 2005.
- [50] T. C. Scott, “TRANSIENT ANALYSIS OF 2 ROW DEEP CROSSFLOW CAC,” pp. 1–45, 2016.
- [51] S. W. Churchill and R. Usagi, “A General Expression for the Correlation of Rates of Transfer and Other Phenomena,” *AIChE J.*, vol. 18, no. November, pp. 1121–1127, 1972.
- [52] S. Al Issa and R. Macian-juan, “Droplets entrainment ratio in a PWR hot-leg pipe geometry,” *Nucl. Eng. Des.*, vol. 330, no. December 2017, pp. 1–13, 2018.
- [53] J. F. Padday, G. Petre, C. G. Rusu, J. Gamero, and G. Wozniak, “The shape, stability and breakage of pendant liquid bridges,” *J. Fluid Mech.*, vol. 352, pp. 177–204, 1997.
- [54] T. Chai and R. R. Draxler, “Root mean square error (RMSE) or mean absolute error (MAE)? -Arguments against avoiding RMSE in the literature,” *Geosci. Model Dev.*, vol. 7, no. 3, pp. 1247–1250, 2014.
- [55] S. J. Kline and F. A. McClintock, “Describing Uncertainties in Single-Sample Experiments,” *Mech. Eng.*, 1953.
- [56] H. W. Coleman and W. . Steele, “Engineering Application of Experimental Uncertainty Analysis,” *AIAA J.*, vol. 33, no. 10, pp. 1888–1896, 1995.

APPENDICES

Appendix A: Uncertainty Analysis

The following appendix presents the uncertainties in the experimentally acquired data. The errors in the measured parameters are discussed and used to estimate the uncertainties of the calculated values. The method for calculating the uncertainties in the calculated parameters is presented. However, since the experiments were not repeated a sufficient amount of times, it is not possible to perform a proper uncertainty analysis including the bias uncertainty. Therefore, an error analysis is performed instead.

A.1 Uncertainty in Measured Parameters

To calculate the Weber number, the face velocity at the heat exchanger was used. The air flow face velocity is measured using a Pacer model DTA 4000 vane anemometer with a resolution of 0.01 m/s. Moving the anemometer over the face of the HX and sampling the air flow indicates an uncertainty in the air velocity of ± 0.1 m/s.

The water was weighed using a Metler model PM6100 electronic balance with a resolution of 0.01g. The unit was recently calibrated so a reasonable estimate for the uncertainty would be ± 0.02 g. Due to evaporation, there is always a loss of the water captured in the towel before it is weighed of less than 0.03 g. Thus, a combined uncertainty due to the scale and evaporation of the water mass collected by the towel is ± 0.04 g. The timer used for the water collection has an uncertainty of ± 0.1 s and the type-K thermocouple used to measure the outlet temperature of the condensate is $\pm 1^\circ\text{C}$.

Table 10: Uncertainty in measured values

Parameter	Symbol	Uncertainty	Units
Face Velocity	V_{face}	± 0.1	m/s
Condensate Mass	m	± 0.04	g
Time	t	± 0.1	s
Outlet Temperature	T_{out}	± 1	$^{\circ}\text{C}$
Inclination Angle	θ_{CAC}	± 0.5	$^{\circ}$
Fin Pitch	Δ_f	± 0.01	mm
Relative Humidity	φ	± 1	%

A.2 Uncertainty in Calculated Parameters

The uncertainties in the calculated experimental parameters were determined using methods described by Kline and McClintock [55] and Coleman and Steele [56]. There is a propagation of error through the equations, which introduce an uncertainty in the calculated parameters. equation 67 was used to determine the uncertainties in the calculated values.

$$U_y = \left[\left(\sum_{m=1}^n \frac{\partial Y}{\partial X_m} U_m \right)^2 \right]^{1/2} \quad (67)$$

Where U_m = Uncertainty of variable $m=1,2,3\dots$

U_y = Propagating uncertainty in result

$\frac{\partial Y}{\partial X_m}$ = Partial derivative of result with respect to variable m .

Y is related to X_m by the following form,

$$Y = f(X_1, X_2, \dots, X_n) \quad (68)$$

A.2.1 Condensate Surface Tension

The surface tension of the condensate is calculated using equation 69. Since the only value with an associated uncertainty is the outlet temperature, it has the same relative uncertainty of around $\pm 5\%$.

$$\sigma_c = 0.1167 - 1.5 \times 10^{-4} T_{out} \quad (69)$$

A.2.2 Air Density

The air density was calculated using equation 70. Since P_{abs} and $R_{specific}$ were assumed to be constant values (101,325 Pa and 287.058 respectively), it is assumed that there is no associated uncertainty. Therefore, the only associated uncertainty is the outlet temperature which has a relative uncertainty of around $\pm 5\%$, giving the density the same relative uncertainty.

$$\rho_a = \frac{P_{abs}}{R_{specific} \times T_{out}} \quad (70)$$

The calculation of the air density is likely one of the largest sources of error since the assumption of constant atmospheric pressure is likely not entirely valid. There would exist a difference in pressure between the air within the CAC and the air that has exited. However, the Weber number is calculated based on the face velocity of the air exiting the CAC, it is considered acceptable to make this assumption. The same reasoning goes for the use of the outlet temperature as the working temperature.

A.2.3 Weber Number

The propagated precision uncertainty for the Weber number was calculated using equation 71, which yields an uncertainty ± 0.04 .

$$U_{We} = \left[\left(\frac{\Delta_f V_{face}^2}{\sigma_c} U_{\rho_a} \right)^2 + \left(\frac{\rho_a V_{face}^2}{\sigma_c} U_{\Delta_f} \right)^2 + \left(\frac{2\rho_a \Delta_f V_{face}}{\sigma_c} U_{V_{face}} \right)^2 + \left(-\frac{\rho_a \Delta_f V_{face}^2}{\sigma_c^2} U_{\sigma_c} \right)^2 \right]^{1/2} \quad (71)$$

A.2.4 Condensate Flow Rate

The propagated precision uncertainty of the condensate flow rate is found using the uncertainties of the captured condensate mass and the collection time and was found using equation 72. This yields a precision uncertainty of ± 0.01 g/s for both the drained and blown through condensate.

$$U_{\dot{m}} = \left[\left(\frac{1}{t} U_{m_{wet}} \right)^2 + \left(-\frac{1}{t} U_{m_{dry}} \right)^2 + \left(-\frac{m_{wet} - m_{dry}}{t^2} U_t \right)^2 \right]^{1/2} \quad (72)$$

Where, m_{dry} and m_{wet} are the mass of the absorbent collector before and after the collection period respectively.

A.2.5 Fraction Carryover

The propagated precision uncertainty for the fraction carryover was found using the uncertainties of the condensate flow rates. It is therefore found using equation 73. This yields a precision uncertainty of ± 0.01 for the fraction carryover.

$$U_{FC} = \left[\left(\frac{\dot{m}_{dr}}{(\dot{m}_{bt} + \dot{m}_{dr})^2} U_{\dot{m}_{bt}} \right)^2 + \left(-\frac{\dot{m}_{bt}}{(\dot{m}_{bt} + \dot{m}_{dr})^2} U_{\dot{m}_{bt}} \right)^2 \right]^{1/2} \quad (73)$$

Where, \dot{m}_{bt} and \dot{m}_{dr} are the flow rate of the blown through and drained condensate respectively.

A.3 Discussion About Bias Error

It is very important to note that the uncertainties calculated above are based solely on the precision of the instruments used to collect the data and it does not consider the bias error, meaning the error that might present itself if the same data point were collected multiple times. Unfortunately, due to a lack of time and resources, the data points were not repeated more than twice, therefore this type of complete uncertainty analysis could not be performed.

For instance, although the precision uncertainty of the fraction carryover is quite low due to the precision of the instrumentation used to calculate it, there is a high chance that the bias uncertainty (i.e. repeatability) present due to the nature of the collection method would increase the overall uncertainty. This is evident by the fact that even repeating the points twice at the same *We* yielded a difference in fraction carryover.

Appendix B: Isokinetic Sampling

When measuring the properties of a fluid stream containing particles using a tube placed in the stream, the velocity within the tube will be lower than the actual fluid stream velocity in which it is immersed. This means that the pressure at the inlet of the tube is slightly higher than that in the stream. Because of this pressure rise, some of the fluid molecules will go around the tube as opposed to entering it. This pressure rise is at a maximum when the tube is solid (i.e. all the fluid goes around the tube.)

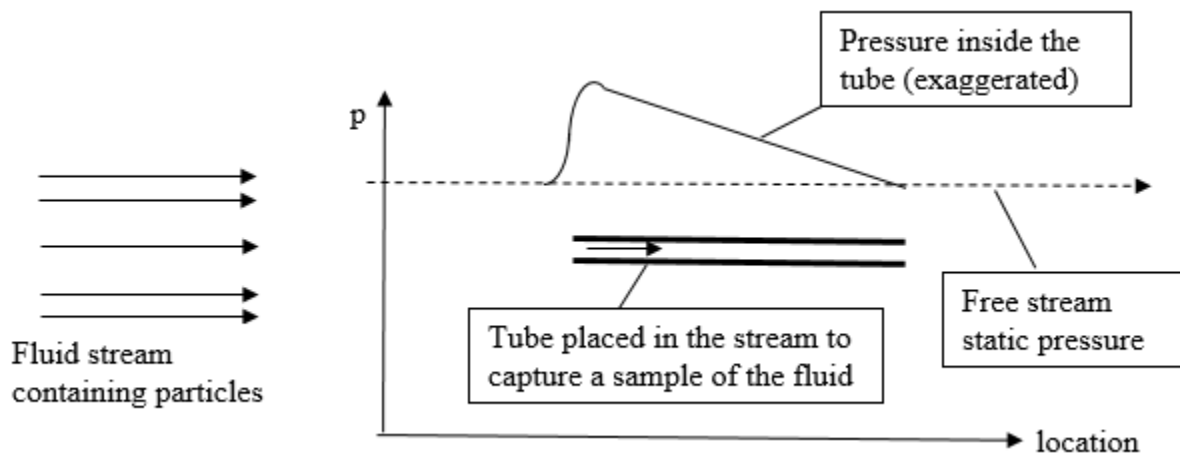


Figure 54: Illustration of pressure drop at tube inlet [21]

Since the particles in the fluid stream have more mass than the fluid molecules, the percentage of particles that bypass the tube will be higher than the percentage of fluid molecules that bypass it. Therefore, if the concentration of particles in the tube is sampled, it will yield a lower value than the concentration outside the tube (i.e. the real concentration).



Figure 55: Particles bypassing tube inlet [21]

To address this issue, the velocity in the tube must be adjusted so that it matches the free-stream velocity. This is usually accomplished by adding a pump at the end of the tube to overcome the pressure drop within the tube. This removes the pressure rise at the tube inlet and the concentration is not affected. The pump must be tuned to ensure that it is not increasing the velocity too much therefore increasing the concentration.

This same concept applies to the measurement of the fraction carryover. A similar phenomenon will occur when the absorbent towel is placed in front of the outlet air stream. It is not an issue if not all the air passes through the cloth since the goal is not to measure the amount of condensation per unit air. However, it is important that all the droplets leaving the CAC are captured by the cloth.

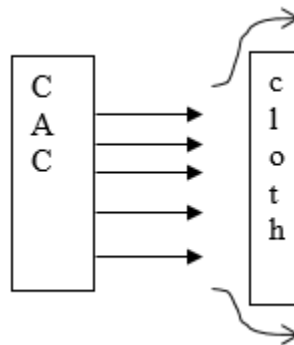


Figure 56: Droplets bypassing the towel due to the pressure rise [21]

Without any sort of velocity compensation, some drops will tend to go around the cloth unless it has an infinite size. It is likely not possible to see exactly how many are going around. What is known for certain is that:

1. A larger cloth area means more of the condensate blow-off is captured.
2. Clothes spaced closer to the CAC will probably capture more condensate.
3. The porosity of the cloth affects the pressure drop across the cloth and thus affects the number of drops captured.
4. At higher V_{face} , more of the blown-through condensate is in the form of large drops, which means they have more difficulty going around the cloth. Therefore, the uncertainty that this causes is likely higher at lower velocities than at higher velocities.

Considering a situation where a different cloth is used to measure the same test point twice, (or the same cloth with a different initial moisture content) and the cloth does not have the exact same area or is not held at exactly the same distance for both tests, an uncertainty is introduced and the two data points will not give exactly the same result. This is likely another cause for the spread in the two tests points being so high despite the low precision uncertainty.

One solution to this problem would be to apply the same sort of isokinetic sampling method as with the tube. A fan could be placed downstream of the cloth to try and increase the velocity to avoid the bypass of water droplets. However, it must be ensured that the fan does not influence the recorded V_{face} . A fixture should also be fabricated to hold the cloth at a set distance with the same face area for all tests.

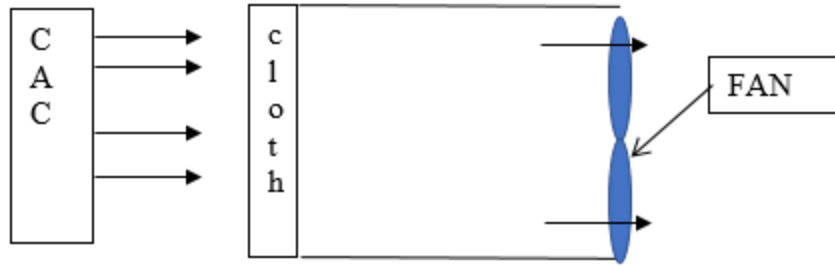


Figure 57: Condensate sampling with isokinetic sampling [21]

VITA AUCTORIS

NAME: Caleb Roch St-Aubin Ouellette

PLACE OF BIRTH: Sudbury, ON, Canada

YEAR OF BIRTH: 1994

EDUCATION: Collège Notre-Dame, Sudbury, ON, 2012

Laurentian University, B.Eng., Sudbury, ON, 2017

University of Windsor, M.A.Sc., Windsor, ON, 2019

Politecnico di Torino, Laurea Magistrale, Torino, Italy, 2019